Buffer-gas Loading and Magnetic Trapping of Atomic Europium

A thesis presented

by

Jinha Kim

to

The Department of Physics

in partial fulfillment of the requirements

for the degree of

Doctor of Philosophy

in the subject of

Physics

Harvard University

Cambridge, Massachusetts

June 1997

To My Parents

Buffer Gas Loading and Magnetic Trapping of Atomic Europium

by

Jinha Kim

Abstract

Atomic europium has been magnetically trapped using buffer-gas loading. Laser ablated Eu($^8S_{7/2}$) atoms are thermalized to 250 mK in a ^{3}He buffer gas. Anti-Helmholtz superconducting coils produce a quadrupole magnetic field to trap the $M_J = 7/2$ state of Eu. Detection is via absorption spectroscopy at 462.7 nm. Up to 1×10^{12} Eu atoms are loaded at a central density of 5×10^{12} cm^{-3}. Atoms can be held for longer than 100 s.

Thesis Advisor: John M. Doyle

Title: Associate Professor of Physics

Acknowledgments

I wish to thank my thesis adviser, Professor John M. Doyle, for his guidance and friendship during my years at Harvard. He taught me everything I know about conducting a scientific research. With patience, he has transformed me from a clueless graduate student into an experimental physicist.

I am greatly indebted to the following people who participated in the set-up and data-taking: Dr. Bretislav Friedrich, Dan Katz, Dave Patterson, Jonathan Weinstein, and Robert deCavalho. Dr. Freidrich was an unofficial second advisor to me and gave me many valuable suggestions throughout the project. Dave, Jonathan and Robert are gratefully acknowledged for their contribution to the experiment and for making the long hours at night bearable with their enthusiasm and sense of humor. I also would like to thank my other labmates in the basement of Lyman, Paul, Carlo, James, Dan, Clint, Brian and Karine for their support. Their presence made the lab a fun and interesting place to work.

I am very grateful to many people outside the lab who made my life during graduate school not only bearable but often enjoyable. I thank Big Dave, and Karen for their advices and for being great traveling companions. Steve, Joe and Deb have been caring and cheerful pals. I am indebted to my classmates from Caltech, Ralph, Mike (Chou) and Mike (Kwan), for years of encouragement, kind words and support. One of the greatest joys during my stay at Harvard has been playing ultimate frisbee. I wish to thank each member of Blue Burning Planet (BBP) for the memories on and off the field and Karl and Zaz for introducing me to this awesome sport.

Eun-Gyung and Sung-Hae have been generous and supportive friends for more than 15 years. I appreciate their enduring friendship and confidence in me.

Mr. Hilleary, my high school math teacher, and Professor. Frautschi from Caltech deserve special thanks for their guidance and encouragement during the earlier phases of my education.

My sincere thanks to Dave Patterson for everything he has done for me for the last

two years. This thesis would not have been possible without the scientific help and moral support he has given me.

Last but foremost, I would like to thank my parents and sister. Words cannot fully express my gratitude and affection toward them for their generous and unflinching support throughout my education and for the joy and happiness they gave me throughout my life. I am deeply grateful to my parents for the sacrifices they made in order to provide for me the opportunities they could only dream of. Their encouragement and belief in me helped me endure the darkest hours of doubt and frustration and complete this thesis. To them. I dedicated my thesis.

Contents

List of Figures

List of Tables

Chapter 1

Introduction

The structure of the atom has been studied for more than a century. Early studies led to and then verified the theory of quantum mechanics. Atoms and small molecules have been useful in testing (and generating new) theory because they can be studied as essentially closed systems. Many other systems exhibit analogous behavior, but are too complex or are too strongly coupled to the environment to be used for precision tests.

In order to gain further precision in atomic studies, two criteria must be met. First, the atom must be decoupled from its environment. This means the atom must be in a low density gas phase, rather than a strongly interacting solid or liquid. Second, the measurement must take place over a long time. This second criteria has driven researchers to search for sources of cold atoms. Thermal cells and beams, the workhorses of atomic physics for many decades, are limited because almost any cold atom ($T <$ 10 K) will stick to any solid wall. Due to the available production techniques, beam temperatures are also limited to $\sim$1 K. .

Together, these criteria have led physicists to develop *traps*, means of confining cold atoms without physical walls. It should be emphasized that any such system is out of equilibrium - if allowed to "thermalize", the atoms would form a solid. It is the low density of trapped samples that allow them to persist for a long time as a low

temperature gas.

In recent years, trapping of atoms has become available through magnetic traps, optical molasses and laser cooling. Evaporative cooling, a technique for cooling atoms once they are in a conservative trap (i.e. the trapping force is conservative), has allowed researchers to cool trapped atoms by many orders of magnitude, and led to the first attainment of Bose Einstein condensation (BEC) in a weakly interacting atomic system.

Although any paramagnetic atom or molecule (including more than half of the periodic table) can be trapped in a static magnetic trap, only a handful of these species have been trapped. So far the trapping of the ground state of neutral particles has been limited to Group 1A atoms, specifically hydrogen, sodium, lithium, and rubidium. This paucity of trapped species has been due to the lack of a general trap loading mechanism.

In order to load atoms into the trap, it is necessary to cool atoms below the trap depth while they are inside the trap. So far, cooling of a few species has been accomplished by cleverly manipulating properties that are unique to those species. In case of hydrogen, it was the low binding energy H has to a liquid He surface. Cooling took place through collision between the liquid He surface and hydrogen atoms. In case of alkali-metal atoms, it was the presence of strong optical transitions and simple internal level structure that allowed optical precooling. In order to greatly expand the number of atoms and molecules that can be trapped, a more general cooling or loading method is necessary.

In this thesis, buffer-gas loading of atoms into a magnetic trap is described and demonstrated using atomic europium. The buffer-gas loading technique has been used for loading ion traps at room temperature. However, it has never been used for loading neutral atom traps until now. The buffer-gas loading used in the thesis relies only on thermalizing elastic collisions between a cryogenic helium gas and the species to be trapped. This precooling method is quite general. Any atoms or molecules that are paramagnetic can be loaded into a magnetic trap as long as the trap depth is higher

than 250 mK (below which no buffer gas exists that has a significant vapor pressure).

Chapter 2 explains the motivation for the cooling and trapping of neutral atoms and gives an overview of other techniques and recent progresses in the field. Chapter 3 presents theoretical background including the spectroscopic properties of europium, information on laser ablation and the theory of absorption spectroscopy of trapped europium. Chapter 4 describes a series of room temperature (table top) experiments that were performed before the trapping experiment. The apparatus and the trapping procedures are described in detail in Chapter 5. Chapter 6 describes the data analysis and presents the results of trapped europium. Finally, Chapter 7 summarizes the work and suggests future directions.

Chapter 2

Background: Trapping and Cooling of Atoms

A neutral atom (Na) was first trapped in 1985 by Migdall et al. [1]. Since then, there has been a rapid progress in the field of trapping and cooling of atoms. Magnetic traps, optical traps, laser cooling, and evaporative cooling are among the techniques used. There have already been many interesting discoveries. The field continues to produce important results and is opening up exciting possibilities in many areas of physics. In this chapter, we present an overview of recent developments in trapping and cooling of neutral atoms. First, the motivation for trapping neutrals will be discussed. Next, the most widely used trapping and cooling techniques will be briefly reviewed. For a comprehensive overview of the experimental development in trapping and cooling of atoms, see the review article by Ketterle and Druten[2].

This chapter is intended for a reader unfamiliar with the field of atomic trapping and cooling. Those readers familiar with the field may wish to skip to Chapter 3 where the description of the new experiments is begun.

2.1 Motivation: Why Trap and Cool Neutral Atoms?

The recent attainment of Bose Einstein condensation (BEC) in a weakly interacting alkali gases has been one of the most exciting developments in atomic physics in the past decade. Realization of BEC offers more than just a confirmation of a prediction made by Bose and Einstein in 1926. Bose-Einstein condensates are a new form of matter, unavailable until now. Perhaps as significant is the creation of "atom laser" which has been now successfully demonstrated at MIT[3]. The "atom laser" is a macroscopic aggregation of coherent atoms just as a laser beam is a system of coherent photons. An atom laser may find use as a new investigative tool for probing surfaces with a very high resolution (e.g. atom interferometry).

From the beginning a primary motivation for pursuing trapping has been to improve the resolution of spectroscopic experiments. Atomic spectroscopy has allowed for precision studies of atomic structures and the careful studies of interatomic interactions. Many of these measurements could be dramatically improved if the atomic samples were colder and slower (confined).

The study of collisions at low temperatures has been particularly interesting. At temperature below 1 K, the dynamics of atomic collisions enters a new regime. Their behavior is qualitatively different from that of thermal energies. For cold collisions, the cross sections for elastic, inelastic, and certain physical and chemical processes can become very sensitive to the interparticle potentials, internal alignment and the presence of light[4, 5, 6]. Advances in cooling and trapping techniques have permitted the study of a new class of inelastic processes for different atoms and enabled the detailed study of higher-order collisional processes[7, 8].

In addition to improvements that can be made with trapping and further cooling of atoms, extending cooling and trapping techniques to molecules will likely have a great impact in many areas of physics and chemistry, and thus is of great interest. High resolution spectroscopy and the study of cold collision physics could be performed

with molecules, thus improving our understanding of intermolecular potentials, energy exchange and cluster formation among many other phenomena.

One of the most exciting prospects offered by working with cold trapped molecules is to make improved tests of time reversal invariance by searching for electric dipole moments (EDM) of elementary particles using radicals such as YbF and TlF[9, 10]. EDM measurements can be made in atoms, but the effect is greatly amplified in highly polar molecules due to the large internal electric field between the constituent atoms. EDM measurements are typically done using a variant of the separated oscillatory fields technique first developed by Ramsey[11]. The sensitivity of these types of experiments is proportional to the interaction time. Current experiments are done primarily in molecular beams, where the interaction time is limited to several ms. In a trap, this time could become 1 s or greater. Further analysis is necessary before the potential improvement of moving to a trap can be quantified, but it may be possible that the sensitivity of an EDM measurement could, in the far future, be increased enough to test some of the limits of the Standard Model[12].

2.2 Trapping Techniques

Wall-free confinement of neutral atoms is accomplished by using interaction between atoms and fields to create a potential well. In most traps, magnetic forces, electric dipole forces or a combination of the two are used to create a trap.

2.2.1 Static Magnetic Traps

One of the most successful traps for neutral atoms has been the static magnetic trap.

Because Maxwell's equations do not allow a maximum of a static field in free space, only atoms in the low-field-seeking states at a minimum of the magnetic field can be trapped. The field geometry of static magnetic traps falls into two categories. One is spherical quadrupole field which is created by coils in an anti-Helmholtz configuration.

It produces a linear, "V-shaped" potential ($E = \mu \frac{dB}{dr} r$, where B is the magnetic field) which provides a tight confinement. The magnetic field is equal to zero at the center of such a trap. The presence of the zero field is problematic (because it can induce Majorana spin-flips of the trapped atoms) and cannot be removed by simple addition of a bias field (this only translates the zero point). BEC of sodium and rubidium atoms was first achieved by using novel "tricks" to circumvent this problem. The MIT group added a blue detuned focused laser beam at the center. Sodium atoms were repelled from the center by the optical dipole force[13]. The Boulder group, on the other hand, added a rotating magnetic field at a frequency higher than the orbiting frequency of the atoms but much less than the Larmor frequency[14]. The resulting time-averaged potential was a parabolic potential with a non-zero minimum.

The second type of trap is a Ioffe-type configuration: it is typically created by four current bars along the axial direction and two pinching coils capping the ends of the current bars. This configuration allows a parabolic (axial) and linear (radial) field minimum around a finite bias field. This removes the loss of the trap atoms due to Majorana spin flips. The first trapping of atomic hydrogen employed this trap configuration[15]. Current work with sodium, lithium and rubidium atoms uses the Ioffe-type trap[16, 17].

One advantage of magnetic traps is the deep trap depth. Using superconducting magnets, a trap depth on the order of at least 1 K (for most paramagnetic atoms) can be easily achieved. However, because atoms are trapped by the higher energy low-field seeking states, collisions can cause transitions to anti-trapped high-field seeking states (which are rejected from the trap). In a magnetic trap, this is mostly caused by spin exchange and dipolar relaxation. Spin exchange involves an exchange of angular momentum between the electron spin and the nuclear spin. It has a rather large rate coefficient, typically 10^{-12} cm^3/s, and usually causes atoms to leave the trap within the first few seconds after loading. Only atoms in a hyperfine state which does not undergo spin relaxation are usually left behind. Even those "pure" states can still spin-flip to

a lower hyperfine state by coupling the spin angular momentum to the orbital angular momentum. This process, called dipolar relaxation, typically has a rate coefficient 1000 times smaller than spin relaxation. Both spin exchange and dipolar relaxation occur at a rate proportional to n, the local density.

At high densities three-body recombination (or dimerization) can also lead to trap loss. At high densities, the rate of dimerization becomes important. This process is proportional to the three-body collision rate. This is because in order for two atoms to form a molecule (which has a lower energy than the sum of the energies of the two atoms), a third body is necessary to carry away the extra energy (in order to conserve both energy and momentum). The three-body recombination is given by Ln^2, where L is the rate coefficient. It becomes a dominant process for $n > 10^{13}$ cm^{-3} for sodium atom (and is similar for other alkali atoms)[2].

All the above processes occur preferentially at the center of a trap where the density of atoms is the highest. The atoms have the lowest total energy. The loss of low energy atoms results in heating of the sample and thus limits the lowest temperature that can be attained by evaporative cooling. The ultimate temperature is determined by the ratio of "good" (elastic) to "bad" (inelastic) collisions. Evaporative cooling is most efficient with atoms that have a high ratio of "good" to "bad" collisions. For hydrogen, the lowest temperature that can be reached by evaporative cooling is 1 μK.[2] For alkali atoms such as sodium or rubidium, it is much lower ($\sim$ *pico* Kelvins) due to the large elastic cross section (1000 times larger than for hydrogen).

2.2.2 Dipole Traps

An atom inside an off-resonant laser beam experiences either an attractive or repulsive potential depending on whether the laser is red- or blue- detuned. Because the potential is proportional to the laser intensity, the atoms aggregate toward the region of maximum laser intensity for red-detuned light and the minimum intensity for blue-detuned light.

Atoms have been trapped in a single tightly focused red-detuned laser beam[18, 19]. Later this design was improved by using two crossed red-detuned beams, which provided a more isotropic trap[20].

In a red-detuned trap, atoms are attracted to the high intensity region. Trapped atoms are subject to heating from scattering by trapping photons. This problem can be somewhat alleviated by using intense, far-detuned light[21, 22]. In a blue-detuned trap, heating is less of an issue because atoms are trapped in the dark region. In such a trap atoms are surrounded by repulsive walls of blue-detuned light. This has been demonstrated for sodium atoms[13].

2.2.3 Other Traps

The Magneto-Optic Trap (MOT) is a non-conservative trap. Trapping is achieved by a combination of viscous and restoring forces which dissipates the kinetic energy of atoms and confines them to a region of space. In this respect, the MOT can be thought of as a cooling and trapping method.(See section 2.3.1.)

Other possible traps include: (1) ac electric field trap which utilizes a harmonic potential produced by the second-order Stark effect around a saddle point of the electric field intensity[23]. (2) microwave trap which traps the lower hyperfine state of hydrogen[24]. (3) ac magnetic trap[25, 26]. (4) electric fields with molecules that have a permanent electric dipole moments and others. Many more varieties are possible by combining them with dipole traps and magnetic traps.

2.3 Loading Techniques

For neutral atom traps, the trap depth is typically about 1 K (for cryogenic traps) to about 100 mK (for room temperature traps). In order to load atoms into such traps, an efficient precooling mechanism is required. Before this work, successful loading of neutral atoms has relied on either interaction of atoms with light (laser cooling) or direct

thermalization with surfaces whose temperature is cryogenically controlled.

2.3.1 Laser Pre-cooling

All of the alkali atoms (with the exception of Fr) have been magnetically trapped (Li, Na, Rb, Cs)[13, 17, 14]. Laser precooling was used to load these atoms into magnetic traps. One important advantage of the laser cooling technique is that atoms can be cooled below 1 mK (typically to 100 μK), therefore allowing the use of a shallow magnetic trap. Because the atoms can be cooled to sub mK temperatures, a magnetic trap can be constructed without using superconducting magnets and the requisite cryogenics to support it. Laser pre-cooling can also be used for loading optical traps whose trap depths are, in general, $\leq$ 1 mK[20].

The general principle behind laser cooling is to manipulate parameters that influence interaction between atoms and photons such that it produces a damping force against the moving atoms. This causes the necessary dissipation of the kinetic energy of the atoms. For example, if an atom is placed in a region of counterpropagating lasers that are red detuned with respect to the transition wavelength, it preferentially absorbs a photon moving in the opposite direction but spontaneously reemits into any direction with equal probability. The net effect is that the atoms get momentum kicks in the opposite direction to their velocity resulting in dissipation of their kinetic energy (i.e. Doppler cooling).

Optical molasses utilizes the Doppler shift to preferentially absorb counterpropagating photons. Although this is not a trap, the strong damping provided by Doppler cooling can also produce viscous confinement. Sodium atoms caught in optical molasses have such a short mean free path that it takes longer than 1 s to diffuse 1 cm. This confinement is similar to that of a particle in Brownian motion in a viscous fluid.

A magneto-optic-trap (MOT), exploits the differences in Zeeman-split levels in a weak inhomogeneous magnetic field to cajole the atoms to preferentially absorb pho-

tons moving in the opposite direction. The optical molasses and MOT were first demonstrated at Bell Lab. in 1985[27] and 1987[28] respectively.

The MOT and optical molasses can be loaded from a vapor cell or a Zeeman-slowed atomic beam[28]. The atoms can then be transferred into a static magnetic trap. Atoms can also be directly loaded into a magnetic trap by employing the Doppler cooling method[29].

For MOT or Doppler cooling, the temperature to which atoms can be cooled is the "Doppler limit", defined by $k_B T = \hbar\Gamma/2$ where Γ^{-1} is the radiative lifetime of the excited state. It was observed that in optical molasses, atoms can be cooled as much as two orders of magnitude below this limit by the polarization gradient cooling[30]. Its limit is given by $k_B T = p^2/2M$, where $p = h/\lambda$ is the recoil momentum of a single scattered photon. In practice, atoms are cooled to no lower than approximately 10 recoil energies by this technique.

Several new laser cooling techniques have been developed to cool atoms even further below the recoil limit. These include Raman cooling[31], velocity-selective coherent population trapping (VSCPT)[32] and gravitational Sisyphus cooling[33]. These cooling techniques have not yet been demonstrated in loading the atoms into a magnetic trap. However, since MOT and Doppler cooling are already sufficient for loading magnetic traps, these new techniques might be used for loading more shallow traps such as optical dipole, a far off-resonance (FORT), or microwave traps.

2.3.2 Pre-cooling via Thermalization with a Surface

Because a sample of gas in physical contact with a surface will thermalize to the temperature of the surface, it seems possible to cool atoms by placing them inside a cold cell. However, this is not feasible at very low temperatures because most atoms impinging upon a wall simply stick to the wall and stay there.

The lowest binding energy of any atom to a wall is 0.4 K, for atomic hydrogen to ^{3}He-

^{4}He liquid-coated walls. For H and helium-coated walls, there is a temperature region in which hydrogen may be contained at reasonable density (100-800 mK). H adsorbed on liquid helium forms a 2 dimensional gas on the surface and does not dissolve in the liquid. For a gas in equilibrium with the surface the surface density, σ, is given by

$$\sigma = n\lambda_d(T)e^{\frac{E_b}{kT}} \tag{2.1}$$

where E_b is the binding energy, n is the bulk density just above the surface and λ_d is the thermal DeBroglie wavelength. As the gas and the wall are cooled down, the surface density increases. Ultimately three-body recombination at the surface rapidly destroys the sample. This limits work with hydrogen in contact with physical walls to temperatures above 80 mK[34]. Also, the residence time on the surface, τ_r, is given by

$$\tau_r = \frac{4\lambda_d}{vs}e^{\frac{E_b}{kT}} \tag{2.2}$$

where v is the average velocity of atoms in the gas and s is the sticking probability. For temperatures below 60 mK, τ_r becomes greater than 1 s and atoms can be considered stuck on the walls.

The first demonstration of evaporative cooling was performed with hydrogen atoms loaded into an Ioffe-type magnetic trap using this technique[15]. For hydrogen, laser cooling is hard to implement because of the difficulty of producing the appropriate high power, cw laser of such short wavelength (121.6 nm) and therefore has never been implemented as a precooling technique. (Although L-α laser cooling of trapped H has been performed[35].)

2.4 Evaporative Cooling

After loading into the trap, the atoms can be further cooled using evaporative cooling. Even though other methods for cooling exist (e.g. sub-recoil Doppler cooling methods such as Raman cooling and VSCPT), evaporative cooling has proven to be very efficient and simple to implement.

Evaporative cooling of trapped neutral atoms was first proposed by Hess in 1985[36] and was observed for the first time at MIT with atomic hydrogen in 1987[37]. Forced evaporation was shown to cool the trapped sample efficiently while simultaneously increasing the density of the atoms[38]. Since then, forced evaporative cooling has become an important tool for producing dense, ultra cold atoms. It was instrumental in achieving BEC.

The advantages of evaporative cooling include general applicability to any atomic species and trap type, the absence of adverse effects due to radiation, the simultaneous decrease in temperature with increase in density, and the fact that it works over a wide range of temperatures and densities. Although the limiting temperature depends on the atomic species and trap methods, for alkali atoms the fundamental temperature limit is expected to be in the pico-Kelvin range[2].

The main principle behind evaporative cooling is simple: the atoms with high energy are preferentially removed from the trap. The remaining atoms then rethermalize at a lower temperature. Successful evaporative cooling requires that the internal thermalization time be short compared to the lifetime of the sample. The thermalization time is set by the atom-atom elastic collision rate and the lifetime is set by loss and heating caused by inelastic collisions ("bad collisions"). Examples of bad collisions are dipolar relaxation, spin exchange, Majorana spin-flips, three-body recombination, Rayleigh scattering, and photoassociative two-body inelastic collisions. (The last two occur in a red-detuned optical dipole trap.)

Forced evaporative cooling has been demonstrated in an optical dipole trap for sodium[20] and in magnetic traps for hydrogen[38], sodium[39], rubidium[14], and lithium[29]. The techniques that have been used for removing high energy atoms in the aforementioned experiments include: lowering the trap edge causing the high energy atoms to stick to the wall[38], and radiatively pumping high energy atoms into untrapped states (that exit the trap and stick to a wall). Radiative evaporation can be

Atom	N	$n_0(\mathrm{cm}^{-3})$	T(K)
H	7×10^{12}	2×10^{13}	1×10^{-3}
Li	2×10^{8}	7×10^{10}	2×10^{-4}
Na	1×10^{9}	1×10^{11}	2×10^{-4}
Rb	4×10^{6}	4×10^{10}	9×10^{-5}

Table 2.1: The former status of magnetic trapping[2]. The number of atoms N, peak density n_0 and temperature T given above are the initial values (right after the loading and before atoms were evaporative cooled).

achieved in different ways. The most common method for magnetically trapped atoms is rf-induced evaporation which exploits one-to-one correspondence between Zeeman shift and potential energy. By tuning the rf-frequency to the hyperfine transition for atoms at high magnetic field, high energy atoms are selectively removed[40]. This can also be done using optical wavelengths if a suitable transition exists. If the linewidth of the transition is broad, one can spatially select out the high energy atoms by focusing the laser on the edge of the atom cloud[35].

To review all the theoretical and experimental studies of evaporative cooling is beyond the scope of this thesis. For more detail, see a review article on evaporative cooling of trapped atoms by Ketterle and Druten[2] and references therein.

2.5 Current Status of Magnetic Trapping

The atoms that have been trapped in their ground state are H, Na, Li, Rb, and Cs[41, 13, 17, 42, 43]. The total number, density and temperature are shown for H, Na, Li and Rb in Table 2.1. BEC has been observed in Rb, Na and Li[14, 44, 45]. In this thesis, we report trapping of europium atoms[46]. A more recent experiment in our lab demonstrated trapping of chromium atoms. That work will not be discussed in this

thesis but is the subject of a future publication[47].

Chapter 3

Theoretical Background

The purpose of this chapter is to provide theoretical background of the trapping and detection techniques employed in the experiment. First, the fundamental mechanisms for the laser ablation process will be described. Second, a physical model of the thermalization process via elastic collisions with the buffer gas will be described. Lastly, the principles behind the spectroscopic detection of Europium will be discussed.

3.1 Laser Ablation

Laser ablation is used in our experiments as a source of atoms. Atoms are liberated from a lump of solid material placed a few centimeters from the trap center. Theoretical and experimental background on the ablation process is presented in this section.

3.1.1 Background

Laser ablation of solid materials has been well established as an important tool in many scientific disciplines including physics, materials science, chemistry and biology. A quick glance at some of its application shows how versatile and widely applied this technique has become: surface processing of materials such as composite substrates[48], organic polymers[49], and inorganic crystals[50], micropackaging, surgery[51], laser desorption

for mass spectrometry[52], generation of x-rays[53] and the growth of novel materials.

Despite prolific practical and scientific applications, sorting out the fundamental mechanisms of laser ablation and identifying the physical processes in a laser-ablation event has proven quite difficult. For example, the coupling mechanism between the laser light and the sample can be very complex since the optical and thermal properties may change upon laser exposure due to formation of excited states, heating, phase transition, and/or photochemical reactions. There are also complications due to plasma formation, nonlinear absorption, or redeposition of ablated materials which have to be taken into account. Therefore, the dominant physics during an ablation event depends strongly on the ablation conditions like fluence, wavelength, pulse duration, and pressure and chemical composition of the ambient gas.

3.1.2 Model for Ablation

Despite this complexity, a simplified description of the laser ablation will be given for the case relevant to our experimental conditions. Although this falls short of explaining the complex and rich phenomena to our satisfaction, it will illuminate some of the basic physical processes that occur during laser ablation.

When the ablation beam impinges on the material, the light is partly absorbed either due to a single photon or multiphoton transition. The absorption causes the temperature to rise. Some of this energy is transferred to the motion of the atoms and ions that make up the lattice. The resulting heating occurs leads to melting, evaporation and plasma formation, depending on the beam intensity.

For intensities greater than 10 kW/cm^2, heat losses at the surface due to black-body radiation($\sim$1 kW) and convection ($\sim$100 W) can be ignored because they are much smaller than the input power. (For our experimental condition, the intensity is typically on the order of $\sim$1 GW/cm^2.) The energy absorbed from the laser heats up the material via conduction. The heat penetration depth due to heat conduction is on

the order of $\sqrt{\kappa t_p}$. where κ is the thermal diffusivity and t_p is the duration of the light pulse. If the laser spot size r and the material thickness d are greater than the diffusion length $\sqrt{\kappa t_p}$. the temperature change, $T - T_0$ may be estimated by

$$\sqrt{\kappa t_p}\rho C_v(T - T_0) \approx (1 - R)I_0 t_p \tag{3.1}$$

where ρ is the density, C_v the specific heat per unit volume. R the reflectivity and I_0 the laser intensity. Since $r \sim 0.01$ cm, $d \sim 1$ cm, and $\sqrt{\kappa t_p} \sim 200$ nm for our experimental condition. the above approximation is valid. If the temperature exceeds the melting and boiling temperature. then the heat of fusion(H_{fus}) and vaporization (H_{vap}) should be added to the left side of eqn. 3.1. Hence,

$$\begin{aligned}\sqrt{\kappa t_p}\rho[C_v(T_{melting} - T_0) + C'_v(T_{boiling} - T_{melting}) + C''_v(T - T_{boiling}) \\ + H_{vap} + H_{fus}] \approx (1 - R)I_0 t_p\end{aligned} \tag{3.2}$$

At intensities between 10^6 W/cm^2 and 10^{10} W/cm^2. the vapor in front of the surface becomes dense and ionized. This in turn increases absorption of the laser beam by the plasma. Multiphoton absorption, photoionization, photochemical reaction, and dust production (i.e. bulk removal of the target) become significant and therefore, the energy involved in these processes need to be taken into account in eqn. 3.2.

3.1.3 Previous Experiments

The time-of-flight experiments at these intensities have shown peculiarities, such as occurences of hyperthermal neutral atoms in addition to thermal atoms. Figure 3.1 shows a two peak structure in kinetic energy distribution of the ablated atoms[54]. The low energy peak is thought to correspond to a regular thermal beam of neutral atoms and the high energy peak correspond to hyperthermal atoms. The high energy peak is typically four to eleven times the temperature of the lower energy peak. A characteristic temperature obtained by fitting a typical time-of-flight data using a half range Maxwell Boltzman is on the order of several tens of thousand Kelvin[55]. The mechanism by

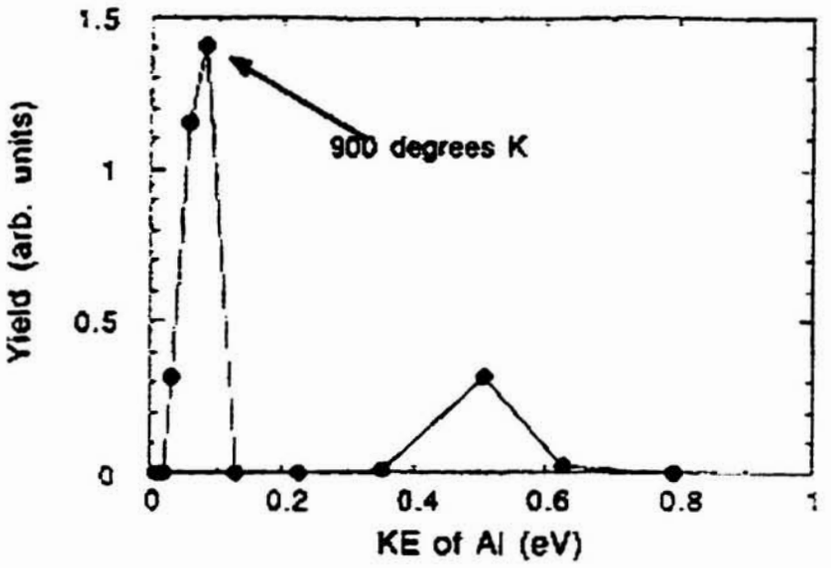

Figure 3.1: Kinetic energy distribution of ablated Al atoms. The figure is taken from ref. [54].

which the atoms gain such high kinetic energies is not understood. In the limiting case of pure thermal vaporization at the surface, it would be expected that atoms would come off near the critical temperature which is typically $\sim 10^3$ K, which corresponds to 0.1 eV. One possible explanation for the production of the hyperthermal atoms is electronically excited desorption of atoms from the surface by direct absorption of photons[54].

For fluence greater than 10^{10} W/cm^2, the material is rapidly transformed into a high temperature (above 10000 K), high density plasma regardless of its chemical composition.

3.2 Buffer Gas Loading

In this section, thermalization with ^{3}He buffer gas as a precooling method is described and a model calculation of the thermalization process is presented.

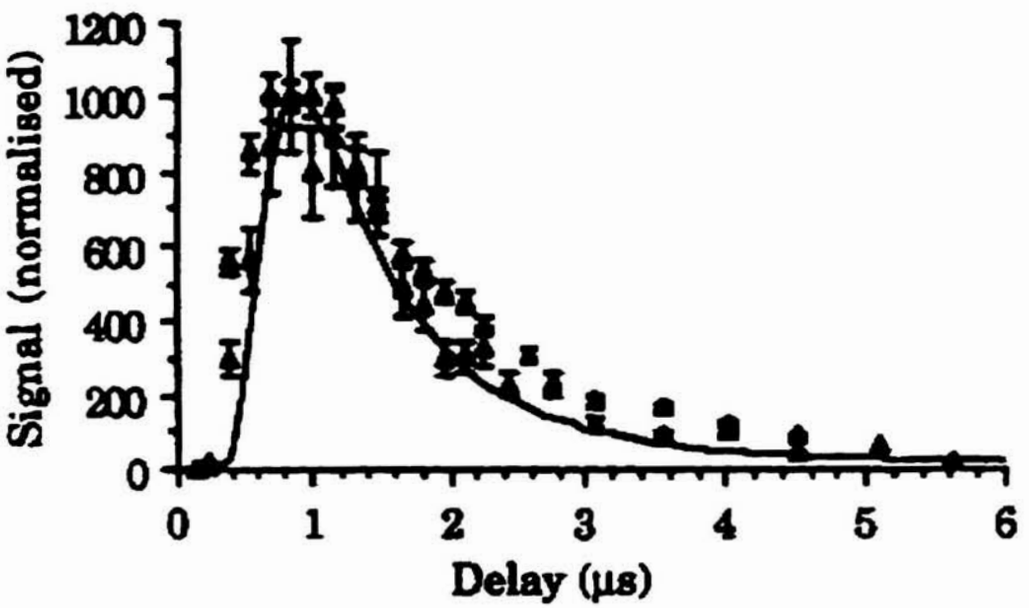

Figure 3.2: Temporal development of the mass spectrometer signal from an aluminium sample fitted with a half range Maxwell Boltzmann distribution with a characteristic temperature of 12000 K. Ablation laser wavelength 532 nm and 275 mJ pulse energy was used. The figure is taken from ref. [56].

3.2.1 Thermalization with Buffer Gas

In order to load atoms into a conservative trapping field, it is necessary to remove translational energy from the atoms while they are in the trap region. One way is via collisions with a cold buffer gas. Because buffer-gas loading relies on elastic collisions, it is essentially independent of the internal structure of the trapped species and therefore should be useful for loading a wide variety of atomic and molecular species into traps. More than half of the atoms (roughly 70%) in the periodic table are paramagnetic (see Table 3.1). Also, a number of interesting non-reactive molecules and many reactive radicals are paramagnetic. As discussed, only alkali atoms and atomic hydrogen have been magnetically trapped due to the lack of an easily employable general precooling technique. Optical cooling techniques applicable in cooling alkali atoms (those have a simple level structure) are difficult to implement for most atoms and molecules. This is due mostly to their complicated level structures. Also, in many cases, the excitation wavelengths are not accessible with current laser technology. Hydrogen was trapped using thermalization with the helium coated surface by exploiting the exceptional low binding energy between them. All other atom-surface pairs have much higher binding energy and therefore this loading scheme cannot be generalized to other species.

The use of a buffer gas for loading traps was first employed for loading ion traps at room temperature[59]. This was possible with ions because the strength of the electrostatic interaction allows very deep traps to be created.

For static magnetic traps, the trap depth is limited to typically 1-10 K even when using superconducting magnets. The total number of molecules loaded into the trap is determined by a balance between the flux of atoms from the atoms source (in our case, laser ablated atoms) and the loss of atoms due to readsorption on the cell walls. The loss of molecules over the trap edge is given by the rate at which atoms at the edge of the trap collide with the physical walls (assuming that any molecule impinging on the wall is lost). The total loss rate is given by $n_e v A/4$, where n_e is the density at the

State $^{2S+1}L_J$	$g_J J$	Element
$^2S_{1/2}$	1.001	H, Li, Na, K, Cu, Rb, Ag, Cs, Au, Fr
$^4S_{3/2}$	3.003	N, P, As, Sb, Bi
$^6S_{5/2}$	5.006	Mn, Re, Tc
$^7S_3$	6.007	Mo, Cr
$^8S_{7/2}$	7.007	Eu
$^2P_{1/2}$	0.333	B, Al, Ga, In, Tl
$^2P_{3/2}$	2.001	F, Cl, Br, I, At
$^3P_2$	3.002	O, S, Se, Te, Po
$^6D_{1/2}$	1.669	Nb
$^2D_{3/2}$	1.199	Sc, Y, La, Lu, Ac
$^3D_3$	4.002	Pt
$^9D_2$	5.303	Gd
$^5D_4$	6.005	Fe, Os
$^4F_{3/2}$	0.598	V, Ta
$^3F_2$	1.332	Ti, Zr, Hf
$^2F_{7/2}$	3.994	Tm
$^3F_4$	5.002	Ni
$^4F_{9/2}$	6.003	Co, Rh, Ir
$^5F_5$	7.005	Ru
$^1G_4$	3.782	Ce
$^6H_{5/2}$	3.782	Pm
$^3H_6$	6.983	Er
$^6H_{15/2}$	9.938	Tb
$^5I_4$	2.413	Nd
$^4I_{9/2}$	3.290	Pr
$^4I_{15/2}$	8.964	Ho
$^5I_8$	9.933	Dy

Table 3.1: Maximum magnetic dipole moments of selected ground-state atoms arranged by term[57, 58]. Here S, L and J are spin, orbital and total electronic angular momentum quantum numbers respectively and g_J is the Landé factor.

wall. v is the average velocity of molecules, and A is the area of the surface defined by the trap edge. The density at the edge of the trap is given by $n_e = n_0 e^{-\eta}$, where $\eta \equiv < \mu > H_{max}/kT$ (i.e. the ratio of the trap depth to the temperature), n_0 is the density at the center, $< \mu >$ is the space-fixed magnetic moment of the atom, H_{max} is the magnetic field strength at the trap edge, T is the translational temperature of the gas. For continuous rf-discharge source, the flux can on the order of 10^{12} s^{-1}[62]. For $\eta = 10$. the expected number density just after initial loading is calculated to be $n_0 = 6 \times 10^{13}$ cm^{-3}. For an ablation source. atoms are released all at once when the ablation beam hits the precursor metal and some fraction of them are loaded into the trap. The trap lifetime, τ. is given by

$$\tau = \frac{4N}{n_e v A} \tag{3.3}$$

where N is the total number of atoms in the trap. $N = n_0 V$ where V is the "effective volume" of the trap. V is determined by the temperature of atoms and the geometry of trapping fields. For our trap, $V = V_0 \eta^{-3}$ with $V_0 = 245$ cm^3 and τ is roughly 1 s for $\eta = 10$ (see Chapter 6.2.4). This gives enough time for the buffer gas to be pulled out of the trap.

The above analysis suggests that in order for buffer gas loading to work, the buffer gas has to have sufficient vapor pressure at temperatures well below 0.1-1 K. Only ^{3}He and ^{4}He gases have a significant vapor pressure in this temperature range. Figure 3.3 shows vapor pressure vs. temperature for ^{3}He and ^{4}He below 1 K. From their vapor pressure curves. it should be possible to load traps with a depth greater than ~2 K using ^{3}He and a depth greater than ~7 K using ^{4}He.

The idea of using cryogenic ^{3}He buffer gas to loading traps was first suggested by Doyle in his thesis[34] and was later described in more detail[62]. The idea outlined was that paramagnetic atoms and molecules would be precooled by elastic collision with ^{3}He buffer gas kept at 240 mK with a number density of $5 \times 10^{15} cm^{-3}$. This takes place in a trapping region created by a static magnetic field. The particles that are precooled to

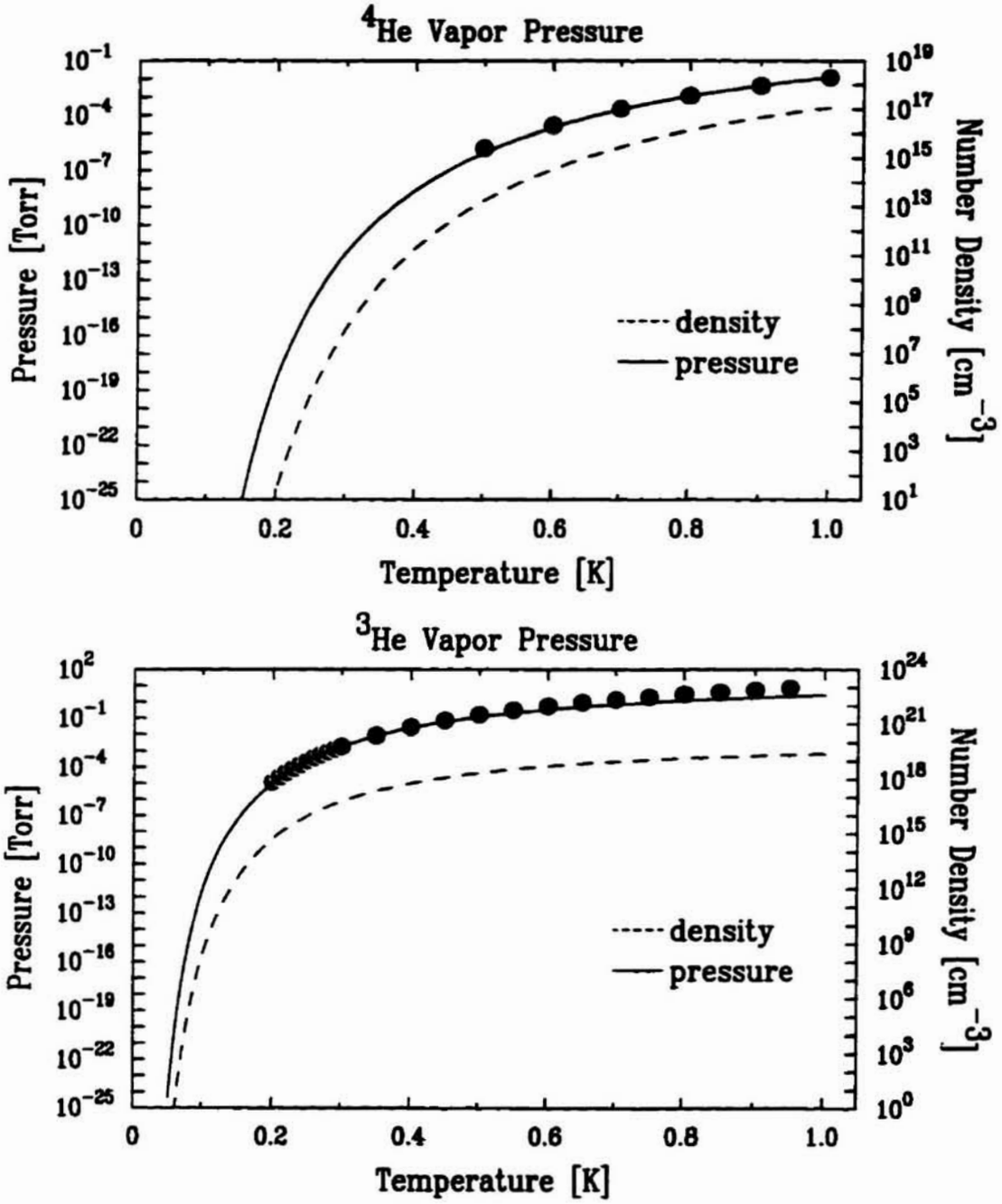

Figure 3.3: Vapor pressure curves of ^{3}He and ^{4}He. The data were taken from ref. [60, 61] and fit with P=a*exp(b/T) where P is pressure and T is temperature.

this temperature are magnetically confined. After loading, the buffer gas is removed by lowering the cell temperature to 80 mK which reduces the vapor pressure below 10^{-15} Torr.

This thesis describes the first realization of this technique using atomic europium and using ^{3}He and ^{4}He as the buffer gas.

3.2.2 The Thermalization Model

Let T_i be the initial temperature of the atoms as it comes off the surface, either as a result of an RF discharge or due to laser ablation and let T_N be the temperature of the atoms after N collisions with the buffer gas at temperature T_b.

In order to find the number of collisions required for thermalization, we first consider the effect of a single collision. For this calculation, we assume the buffer gas and the atom to be trapped are two point particles of mass, m and M. Their velocities before the collision are $\vec{v}_i$ and $\vec{V}_i$ and after the collision are $\vec{v}_f$ and $\vec{V}_f$. In order to simplify the calculation, we change into the center of mass frame with $\vec{V}_{cm} = \frac{M\vec{V}_i + m\vec{v}_i}{M+m}$ and let $\tilde{\mathbf{v}}_i, \tilde{\mathbf{V}}_i, \tilde{\mathbf{v}}_f$, and $\tilde{\mathbf{V}}_f$ be the velocities in the center of mass frame. The conservation of momentum and energy in this frame give

$$P^{tot} = 0 = M\tilde{\mathbf{V}}_i + m\tilde{\mathbf{v}}_i = M\tilde{\mathbf{V}}_f + m\tilde{\mathbf{v}}_f \tag{3.4}$$

$$E^{tot} = \frac{M}{2}\tilde{V}_i^2 + \frac{m}{2}\tilde{v}_i^2 = \frac{M}{2}\tilde{V}_f^2 + \frac{m}{2}\tilde{v}_f^2 \tag{3.5}$$

Averaging over statistical distribution of the atoms and using the conservation laws,

$$\begin{aligned} < \tilde{V}_f^2 > &=< \tilde{V}_i^2 > = < V_i^2 + V_{cm}^2 - 2\vec{V}_i \cdot \vec{V}_{cm} > \\ &=< V_i^2 > + < V_{cm}^2 > - \frac{2M}{M+m} < V_i^2 > - \frac{2m}{M+m} < \vec{V}_i \cdot \vec{v}_i > \\ &= (1 - \frac{2M}{M+m}) < V_i^2 > + < V_{cm}^2 > \end{aligned} \tag{3.6}$$

$$
\begin{aligned}
< V_f^2 > =< (\vec{\mathbf{V}}_f + \vec{V}_{cm})^2 >=< \vec{V}_f^2 > + < V_{cm}^2 > +2 < \vec{\mathbf{V}}_f \cdot \vec{V}_{cm} > \\
= (1 - \frac{2M}{M+m}) < V_i^2 > + \frac{2}{(M+m)^2}(M^2 < V_i^2 > + m^2 < v_i^2 >) \\
= \frac{M^2+m^2}{(M+m)^2} < V_i^2 > + \frac{2m^2}{(M+m)^2} < v_i^2 > \qquad (3.7)
\end{aligned}
$$

$< \vec{V}_i \cdot \vec{v}_i >$ and $< \vec{\mathbf{V}}_f \cdot \vec{V}_{cm} >$ are equal to zero from symmetry.

$$
\begin{aligned}
< V_f^2 - V_i^2 > &= -\frac{2Mm}{(M+m)^2} < V_i^2 > + \frac{2m^2}{(M+m)^2} < v_i^2 > \qquad (3.8) \\
&= \frac{2m}{(M+m)^2}(M < V_i^2 > - m < v_i^2 >) \qquad (3.9)
\end{aligned}
$$

The change in temperature of an atom before and after colliding with a buffer gas is the

$$T_f - T_i = -\frac{2Mm}{(M+m)^2}(T_i - T_b) \qquad (3.10)$$

This can be generalized into a differential equation.

$$\frac{dT_N}{dN} = -\frac{2Mm}{(M+m)^2}(T_N - T_b) \qquad (3.11)$$

where T_N is the temperature of the trap atom after N collisions with the buffer gas. The solution to eqn. 3.11 is given by

$$T(N) = (T_i - T_b)exp\left(-\frac{2Mm}{(M+m)^2}N\right) + T_b \qquad (3.12)$$

The characteristic number of collisions (i.e. 1/e) for thermalization is given by $\frac{(M+m)^2}{2Mm}$ which is 26 for Eu atoms in ^{3}He buffer gas.

The number of collisions required for hot Eu atoms to reach within ±10% of the buffer gas temperature is 250 for T_{Eu}= 1000 K and $T_{^3He} = 0.25$ K.

In order to ensure that the atoms thermalize before colliding with the wall of the container surrounding the trap, it is necessary that the density of the buffer gas be such that the displacement of the atoms after 250 collisions is smaller than the size of the trap region (e.g. $250 \times \lambda_m \leq d = 2$ cm where λ_m is the mean free path of the Eu in the helium and d is the diameter of the cell). Because Eu atoms are much heavier and energetic

than ^{3}He atoms, they travel ballistically for most of their path before thermalizing to the temperature of the buffer gas. Therefore, the path length traveled during N collisions is $N \times \lambda_m$ (instead of $\sqrt{N} \times \lambda_m$.) If we assume an elastic cross section of about 10^{-14} cm^2 between Eu and ^{3}He[11], then the minimum density required is $\sim 10^{16}$ cm^{-3}. For ^{3}He, the density at 250 mK is 7×10^{15} and thus satisfies this criterion. (See Figure 3.3.)

3.3 Spectroscopic Detection of Eu

In this section, the theoretical background for spectroscopic detection of Eu is presented. This includes calculations of the eigenenergies of Eu vs. magnetic field strength, the absorption cross section and from these, the number density.

3.3.1 Hyperfine eigenstates of Eu

The Hamiltonian $\mathcal{H}$ of an atom with total electronic angular momentum $\vec{J}$ and nuclear spin $\vec{I}$ subject to an external magnetic field $\vec{H}$ takes the form:

$$\mathcal{H} = g_J \mu_b \vec{J} \cdot \vec{H} + g_I \mu_b \vec{I} \cdot \vec{H} + a\vec{I} \cdot \vec{J} + b\frac{\frac{3}{2}\vec{I} \cdot \vec{J}(2\vec{I} \cdot \vec{J} + 1) - \vec{I}^2 \cdot \vec{J}^2}{2I(2I-1)J(2J-1)} \tag{3.13}$$

where J and I are the electronic and nuclear angular momentum quantum numbers, g_I and g_J the corresponding g-factors, a and b the hyperfine magnetic dipole and electric quadrupole coupling constants, and μ_B the Bohr magneton. The actual values of the aforementioned constants for $a^8S^u_{7/2}$, $z^{10}P^g_{7/2}$ and $y^8P^g_{7/2}$ are given in Table 3.2. The matrix elements of $\mathcal{H}$ can be obtained analytically either in the coupled basis, $|F, M>$, corresponding to the weak-field limit, or in the uncoupled basis $|M_J, M_I>$, corresponding to the strong-field limit. Hence, either yields the eigenenergies and line strengths in closed form.

State	g_J	^{151}a	^{153}a	^{151}b	^{153}b	Isotopic shift	λ
$a^8S^u_{7/2}$	1.99	-20.05	-8.85	-0.7	-1.78	-	0
$z^{10}P^g_{7/2}$	2.225	968.6	431.3	157.3	398	0	710.6
$y^8P^g_{7/2}$	1.929	-219.1	-97	-295	-753	-2977	462.7

Table 3.2: Hyperfine constants (in MHz) of selected states of Eu, their g-factors, isotopic shifts (in MHz), and wavelengths (in nm) of transitions from the ground state. The natural abundances of the 151 and 153 isotopes are 47.8% and 52.2% and both isotopes have nuclear spin of 5/2. The values were taken from ref. [63].

Low-field limit

In the low-field limit, the angular momenta $\vec{J}$ and $\vec{I}$ couple to a resultant angular momentum $\vec{F} = \vec{J}+\vec{I}$ characterized by a quantum number $F = J+I, J+I-1, \ldots, |J-I|$: each value of F has $2F+1$ projections $M = -F, -F-1, \ldots, +F$ on the space-fixed axis defined by the directions $\vec{H}$. Note that there are $\sum_F(2F+1) = (2J+1)(2I+1)$ coupled states $|F, M>$. The eigenenergy is given by

$$E(F,M) = \frac{1}{2}aK + b\frac{\frac{3}{4}K(K+1) - I(I+1)J(J+1)}{2I(2I-1)J(2J-1)} + Mg_F\mu_B H \tag{3.14}$$

where

$$K \equiv F(F+1) - J(J+1) - I(I+1) \tag{3.15}$$

and

$$g_F = g_J\frac{F(F+1) + J(J+1) - I(I+1)}{2F(F+1)} \tag{3.16}$$

with

$$g_J = \frac{J(J+1) + L(L+1) - S(S+1)}{2J(J+1)} + g_S\frac{J(J+1) + S(S+1) - L(L+1)}{2J(J+1)} \tag{3.17}$$

S and L the total electronic spin and orbital angular omentum quantum numbers, and g_S the gyromagnetic ratio of the electron; $H \equiv |\vec{H}|$.

High-field limit

In the strong-field limit, the angular momenta $\vec{J}$ and $\vec{I}$ are no longer integrals of motion but their projections M_J and M_I on the space-fixed axis are. Since M_J and M_I take respectively $(2J+1)$ and $(2I+1)$ values, there are (2J+1)(2I+1) uncoupled states $|M_J, M_I>$. In the uncoupled basis, the eigenvalues of Hamiltonian 3.13 are given by

$$E(M_J, M_I) = M_J g_J \mu_B H + M_I g_I \mu_B H + a M_J M_I + \frac{9b}{4I(2I-1)J(2J-1)}[M_J^2 - \frac{1}{3}J(J+1)][M_I^2 - \frac{1}{3}I(I+1)] \quad (3.18)$$

(neglecting the magnetic octupole and higher-order interactions)

Energy vs. Magnetic field : Exact Calculation

In the intermediate-field regime, the energy level can be solved exactly by diagonalizing the Hamiltonian. The matrix elements of this Hamiltonian can be most easily calculated in the uncoupled basis, $|M_J, M_I>$.

The explicit evaluation of the non-zero matrix elements are as follows.

$$< M_J, M_I | g_J \mu_B J_z H | M_J, M_I >= g_J \mu_B M_J H \quad (3.19)$$

$$< M_J, M_I | g_I \mu_B I_z H | M_J, M_I >= g_I \mu_B M_I H \quad (3.20)$$

$$< M_J, M_I | a\vec{I} \cdot \vec{J} | M_J, M_I >= a M_I M_J \quad (3.21)$$

$$< M_J, M_I | a\vec{I} \cdot \vec{J} | M_{J-1}, M_{I+1} > = \frac{1}{2} a \sqrt{J(J+1) - M_J(M_J-1)} \sqrt{I(I+1) - M_I(M_I+1)} \quad (3.22)$$

$$< M_J, M_I|a\vec{I}\cdot\vec{J}|M_{J+1}, M_{I-1} > = \frac{1}{2}a\sqrt{J(J+1)-M_J(M_J+1)}\sqrt{I(I+1)-M_I(M_I-1)} \quad (3.23)$$

If we let $\beta \equiv \frac{b}{2I(2I-1)J(2J-1)}$ and $f \equiv \frac{3}{2}\vec{I}\cdot\vec{J}(2\vec{I}\cdot\vec{J}+1)-\vec{I}^2\cdot\vec{J}^2$ then the last term in the Hamiltonian (eqn. 3.13) can be written as βf. The matrix elements corresponding to this interaction are

$$< M_J. M_I|\beta f|M_J. M_I >= \frac{1}{2}\beta[3M_I^2 - I(I+1)][3M_J^2 - J(J+1)] \quad (3.24)$$

$$< M_J. M_I|\beta f|M_{J-1}. M_{I+1} >= \frac{3}{4}\beta(2M_J-1)(2M_I+1) \sqrt{(J+M_J)(J-M_J+1)(I-M_I)(I+M_I+1)} \quad (3.25)$$

$$< M_J. M_I|\beta f|M_{J-1}. M_{I-1} >= \frac{3}{4}\beta(2M_J+1)(2M_I-1) \sqrt{(J-M_J)(J+M_J+1)(I+M_I)(I-M_I+1)} \quad (3.26)$$

$$< M_J. M_I|\beta f|M_{J-2}. M_{I+2} >= \frac{3}{4}\beta[(J+M_J)(J+M_J-1)(J-M_J+1)(J-M_J+2) (I-M_I)(I-M_I-1)(I+M_I+1)(I+M_I+2)]^{\frac{1}{2}} \quad (3.27)$$

$$< M_J. M_I|\beta f|M_{J+2}. M_{I-2} >= \frac{3}{4}\beta[(J-M_J)(J-M_J-1)(J+M_J+1)(J+M_J+2) (I+M_I)(I+M_I-1)(I-M_I+1)(I-M_I+2)]^{\frac{1}{2}} \quad (3.28)$$

Figure 3.4 shows the result of this calculation for ground and excited state for ^{151,153}Eu. In the low-field limit, the total angular momentum, $\vec{F}$, and M_F are good quantum numbers. As the magnetic field strength is increased, the energy levels become grouped according to M_I and M_J values (which are good quantum numbers in the high-field limit). The correlation between the energy levels at these two limits is illustrated in Figure 3.5.

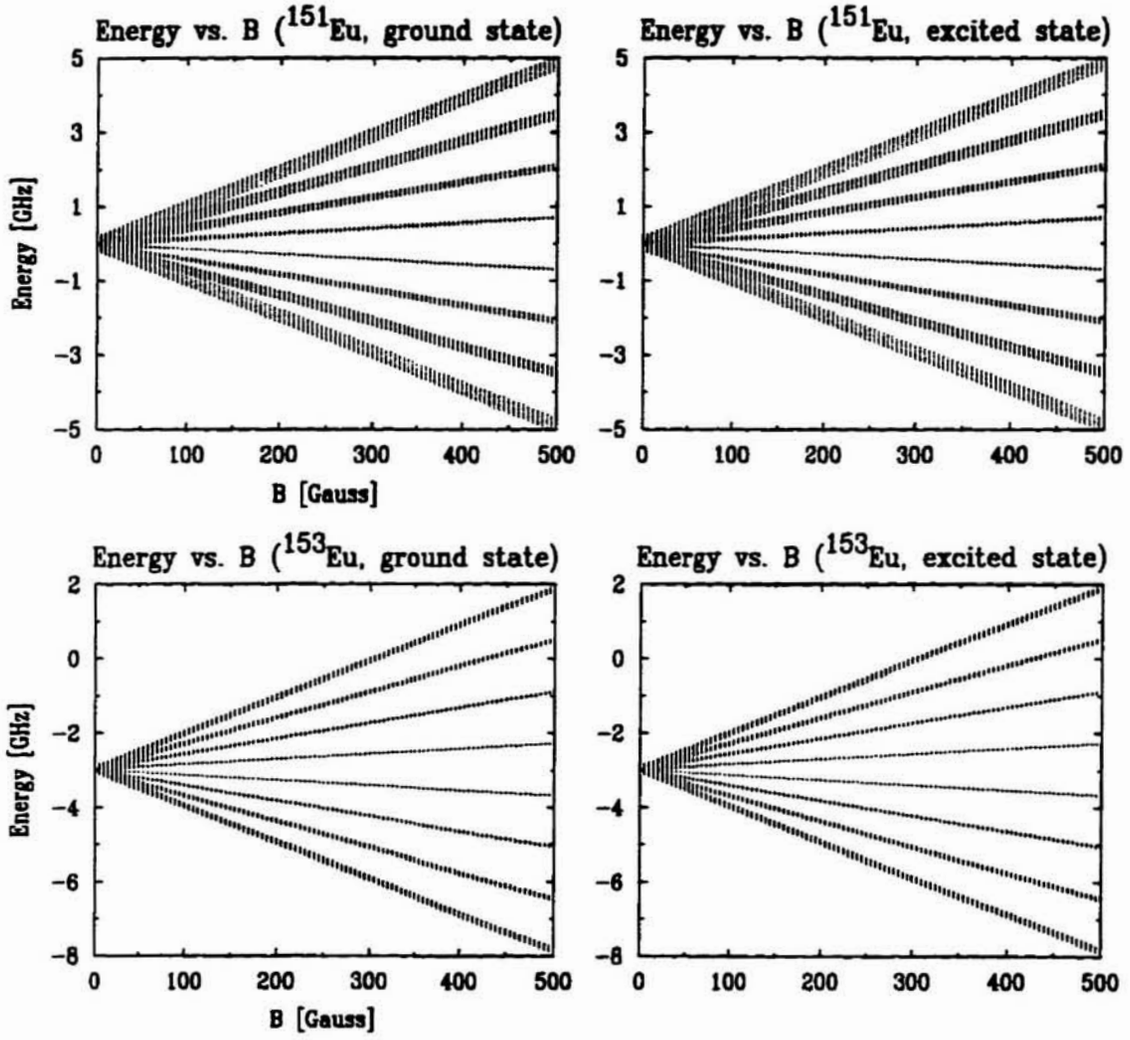

Figure 3.4: Eigenenergies of Eu atoms in the ground state and in $y^8P^g_{7/2}$ excited state at different magnetic field strengths. At high field, levels split to 8 bands (corresponding to different M_Js) with each band consisting of 5 different levels (corresponding to 5 M_Is). The magnified level structure is shown in Figure 3.5.

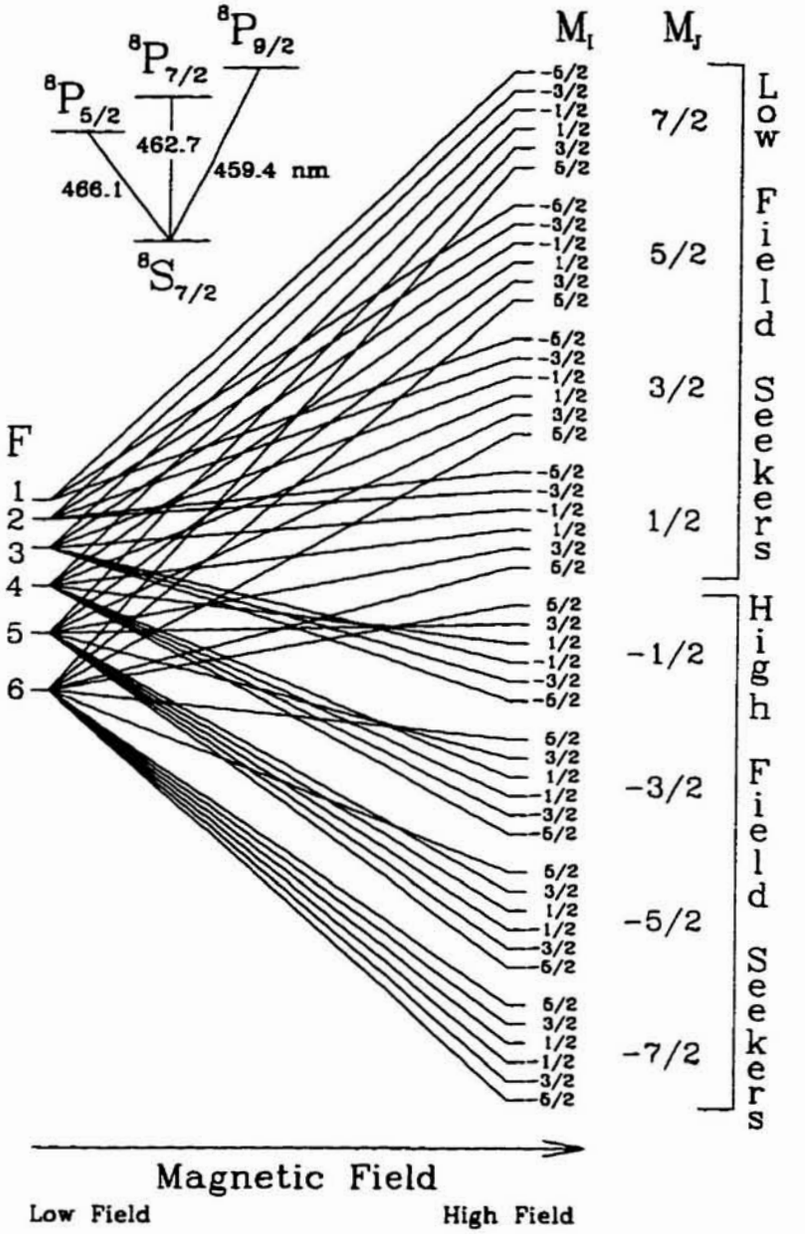

Figure 3.5: The correlation diagram of eigenstates of Eu atoms (for $^8S_{7/2}$and$^8P_{7/2}$ states).

3.3.2 Line Strength Factor

The line strength factor $S_q(M'_J, M'_I; M_J, M_I)$ of a transition between states $|M'_J, M'_I > \leftarrow |M_J, M_I >$ due to an electric dipole moment d_q (of unit magnitude, with $q = 0$ for parallel and $q = \pm 1$ for perpendicular transition) is given by

$$S_q = |< M'_J, M'_I | d_q | M_J, M_I >|^2 \tag{3.29}$$

$$< M'_J, M'_I | d_q | M_J, M_I > \propto \delta(M'_I, M_I) < J, 1, M_J, q; J', M'_J >< J' || d || J > \tag{3.30}$$

where $< J. 1. M_J, q; J'. M'_J >$ is a Clebsch-Gordan coefficient[64].

3.3.3 Absorption

When an atomic system is subject to a monochromatic radiation, it has a probability, $P_{if}(t)$, of absorbing a photon and make a transition from the lower energy level E_i into the higher level E_f. This process is called (induced) absorption. The transition probability per second, $\frac{d}{dt}P_{if}$ is given by

$$\frac{d}{dt}P_{if} = \rho(\nu_{fi}) B_{if} \tag{3.31}$$

where $\rho(\nu_{fi})$ the spectral energy density of the radiation field and $\nu_{fi} = (E_f - Ei)/h$. The constant factor B_{if} is the Einstein coefficient of induced absorption and is given by

$$\begin{aligned} B_{if} &= \frac{1}{6\epsilon_0 \hbar^2} |\vec{d}_{if}|^2 \\ &= \frac{1}{2\epsilon_0 \hbar^2} \left(\frac{1}{3} |< d_x >|^2 + \frac{1}{3} |< d_y >|^2 + \frac{1}{3} |< d_z >|^2 \right) \\ &= \frac{e^2}{2\epsilon_0 \hbar^2} \left(\frac{1}{3} |< x >|^2 + \frac{1}{3} |< y >|^2 + \frac{1}{3} |< z >|^2 \right) \end{aligned} \tag{3.32}$$

for isotropic case. The factor $\frac{1}{3}$ in front of x^2, y^2, z^2 indicates that the atoms are randomly oriented with respect to the electric field of the radiation. If, however, the atoms are not randomly oriented with respect to the field, then B_{if} should be modified to

$$B_{if} = \frac{e^2}{2\epsilon_0 \hbar^2} \left(f_x |< x >|^2 + f_y |< y >|^2 + f_z |< z >|^2 \right) \tag{3.33}$$

f_x, f_y, and f_z are given by $< sin^2\theta cos^2\phi >, < sin^2\theta sin^2\phi >$, and $< cos^2\theta >$ respectively by taking z-direction to be along the orientation of atoms and averaging over the atoms subject to the radiation.

In evaluating the matrix element of the dipole operator between angular momentum states, it is more convenient to express x, y, and z as a superposition of tensor operators whose rank is 1. $Y^1_{-1}, Y^1_0, Y^1_{+1}$. This is because we can then use the Wigner-Eckart theorem to evaluate the ratio between the different components of the same tensor operator. (The difference among the different components of the same tensor operator is due to geometry, not dynamics, and it is given by Clebsch-Gordon coefficients.)

They are given by

$$x \propto \frac{1}{\sqrt{2}}(Y^1_{-1} - Y^1_{+1}) \tag{3.34}$$

$$y \propto \frac{i}{\sqrt{2}}(Y^1_{-1} + Y^1_{+1}) \tag{3.35}$$

$$z \propto Y^1_0 \tag{3.36}$$

For $|i> = |M_J, M_I>$ and $|f> = |M'_J, M'_I>$, B_{if} then can be expressed in terms of tensor operators as follows:

$$\begin{aligned} B_{if} &= \frac{1}{2\epsilon_0\hbar^2}\left(F_{-1}|< d_{-1} >|^2 + F_0|< d_0 >|^2 + F_{+1}|< d_{+1} >|^2\right) \\ &\propto \frac{e^2}{2\epsilon_0\hbar^2}\left(F_{-1}|< Y^1_{-1} >|^2 + F_0|< Y^1_0 >|^2 + F_{+1}|< Y^1_{+1} >|^2\right) \\ &\propto \sum_{q=-1}^{q=+1} F_q S_q(M'_J, M'_I; M_J, M_I) \end{aligned} \tag{3.37}$$

where

$$F_{-1} = \frac{1}{2}(f_x + f_y) \tag{3.38}$$

$$F_0 = f_z \tag{3.39}$$

$$F_1 = \frac{1}{2}(f_x + f_y) \tag{3.40}$$

and S_q is given by eqn. 3.30. Note that for an isotropic case (either an isotropic radiation and/or random orientation of atoms), F_{-1}, F_0, and F_{-1} are $\frac{1}{3}$ each. If the

atomic system has degeneracies g_i for the initial state and g_f for the final state. then

$$B_{if} = \frac{1}{2\epsilon_0\hbar^2}\frac{1}{g_i}\sum_{g_i}\sum_{g_k} F_{-1}|< d_{-1} >|^2 + F_0|< d_0 >|^2 + F_{+1}|< d_{+1} >|^2 \tag{3.41}$$

For $|i>=|M'_J, M'_I>$ and $|f>=|M_J, M_I>$, (i.e in presence of a high magnetic field)

$$B_{if} = \frac{1}{2\epsilon_0\hbar^2}\sum_{q=-1}^{q=+1} F_q S_q(M'_J, M'_I; M_J, M_I) \tag{3.42}$$

Absorption Cross Section

The rate of change in the population numbers for a system with two energy levels, E_1 and E_2, populated by N_1 and N_2 is

$$\begin{aligned}\frac{dN_1}{dt} &= -\frac{dN_2}{dt} \\ &= -B_{12}\rho(\nu)N_1 + B_{21}\rho(\nu)N_2 + A_{21}N_2\end{aligned} \tag{3.43}$$

In a steady-state situation where N_1 change little over time. the ratio of N_2 to N_1 is

$$\frac{N_2}{N_1} = \frac{B_{12}\rho(\nu)}{B_{21}\rho(\nu) + A_{21}} \tag{3.44}$$

If $A_{21} \gg B_{12}\rho(\nu)$. $N_{total} \approx N_1$ and most of the photons absorbed are lost from the incident flux due to spontaneous emission. This enables us to directly infer the number of atoms in the laser beam from the power absorbed. The rate of photon absorption per atom is $B_{12}\rho(\nu)$. If we let σ_{abs} be the rate of the photon absorption per incident photon flux.

$$\sigma_{abs}(\nu) = \frac{h\nu}{c}B_{12}\mathcal{S}(\nu) \tag{3.45}$$

The $\mathcal{S}(\nu)$ term which gives the frequency dependence of the cross section depends on the spectral density of the impinging radiation field and the spectral features of the $|i> \rightarrow |f>$ transition such as natural linewidth, Doppler broadening, magnetic broadening, isotope effect, and hyperfine interaction. Its normalization is given by

$$\int_0^\infty \mathcal{S}(\nu)d\nu = 1 \tag{3.46}$$

In the low optical density regime, $S(\nu)$ is simply the absorptance at ν divided by the integrated area of the spectrum. (i.e. $S(\nu) \approx \mathcal{A}(\nu)/\int_\nu \mathcal{A}(\nu)d\nu$ where $\mathcal{A}(\nu)$ is absorptance at ν)

3.3.4 Absorption Spectroscopy: Density of Atoms in the Trap

When a laser beam passes through an absorbing medium, its power decreases due to absorption. The absorptance $\mathcal{A}$ is defined as

$$\mathcal{A} \equiv 1 - \frac{P_{out}}{P_{in}} \tag{3.47}$$

where P_{in} and P_{out} are the input and transmitted power respectively. For absorption cross section $\sigma(\nu)$ and density of the medium $n(x, y, z)$,

$$\mathcal{A} = 1 - \frac{1}{\mathrm{A}} \int_x \int_y dxdy\ exp(-\int_{z_{init}}^{z_{final}} \sigma(\nu) n(x, y, z) dz) \tag{3.48}$$

where A is the beam area. For atoms inside a magnetic trap,

$$n(x, y, z) = n_0 exp(-\frac{< \mu > H(x, y, z)}{kT}) \tag{3.49}$$

Therefore, we can extract the number of atoms and the central density from the absorption profile if the magnetic field distribution, temperature, beam geometry and the absorption cross section are known.

Note that the absorption cross section for untrapped Eu with random orientation is different from that of trapped Eu atoms. This is because both $S(\nu)$'s and B_{if}'s (line strength and Einstein B coefficient) are different for trapped and untrapped atoms. This is due to the fact that only $M_J = 7/2$ states are trapped and that the atoms are oriented according to the magnetic field distribution (see eqn. 3.42). The above model was implemented as a program in determining the number of Eu atoms and the density in the trap.

Chapter 4

Preliminary Experiments

In this chapter, the procedures and results of several preliminary experiments (before the actual trapping of Eu) are discussed. This includes spectroscopic detection of oxygen molecules, and attempts to produce Eu atoms using various techniques. Some of this early work is directly relevant to the trapping of Eu. Some, although not directly relevant, is included for completeness and to assist others in future work on trapping of molecules and atoms.

4.1 Laser Ablation

The application and basic theory of laser ablation have already been discussed in Chapter 3.1. In this section we present work on laser ablation and detection of solid Eu using the table top, room-temperature cell.

Although laser ablation has found broad application in material science, it has rarely been used as an atom source. One of the great advantages of laser ablation is its versatility. By choosing the right precursor and ablation laser intensity, many different atoms and molecules in a variety of internal states can be produced. Atoms, molecules and ions are produced simultaneously during a single laser ablation pulse. By tuning the experimental parameters, the yield of a certain species can be enhanced. Another

advantage is the simplicity of implementing laser ablation: it can be used in almost any apparatus with an optical access.(e.g., in contrast to a thermal beam which itself requires an apparatus for its production.)

Because laser ablation is a rapid, nonequilibrium process, it heats the sample (e.g. chunk of solid Eu) only locally and over a small surface area (determined by the beam spot size). Thus the energy required to vaporize the sample can be small compared to other methods. With a single 10 mJ, 5 ns pulse, focussed down to about 100 μm, more than 10^{13} neutral Eu atoms are produced. (The initial number of atoms in the trap is about 10^{12}. Because only one out of seven M_J states is trapped, we expect the actual production of atoms to be at least 10 times higher. See Chapter6.2.)

4.1.1 Apparatus

Figure 4.1 shows the basic arrangement of the apparatus used in preliminary studies of laser ablation. The pulsed beam enters through the window opposite the Eu lump and is focused on its surface. This is inside a vacuum cell made out of a CF 4-way cross. The focusing lens is mounted on a translational stage to allow fine tuning of its focal position (and thus the diameter of the beam spot on the ablation target).

A probe beam is used to detect the ablated atoms and it enters the cell perpendicular to the pulsed YAG beam and exits on the other side. The distance between the probe beam and the ablation target, Eu lump, was varied between 1-10 mm. The cell was connected to a small gas handling system for introducing and pumping out the buffer gas to the cell and measuring its pressure.

Measurements were carried out over different ranges in pressure, pulse power, and with different buffer gases. The frequency of the probe laser was often fixed at one of the Eu lines (710.841 nm).

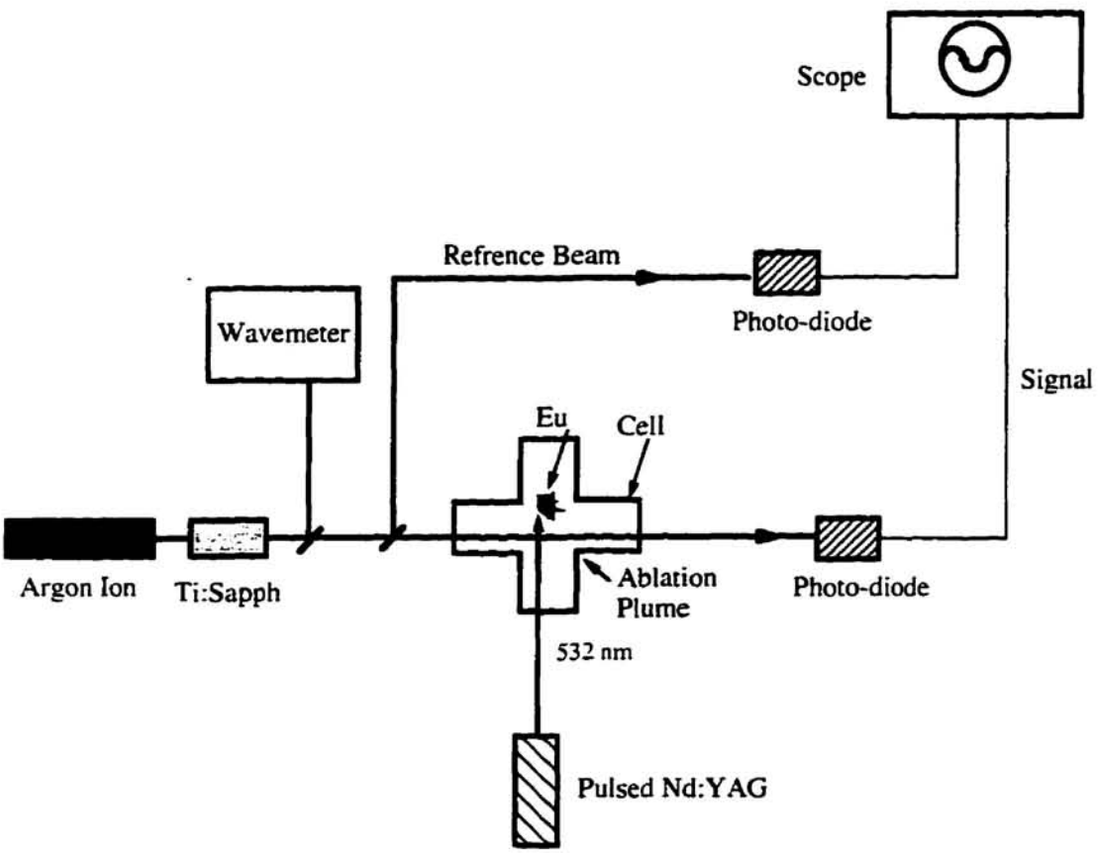

Figure 4.1: A table-top setup for ablation and detection of Eu.

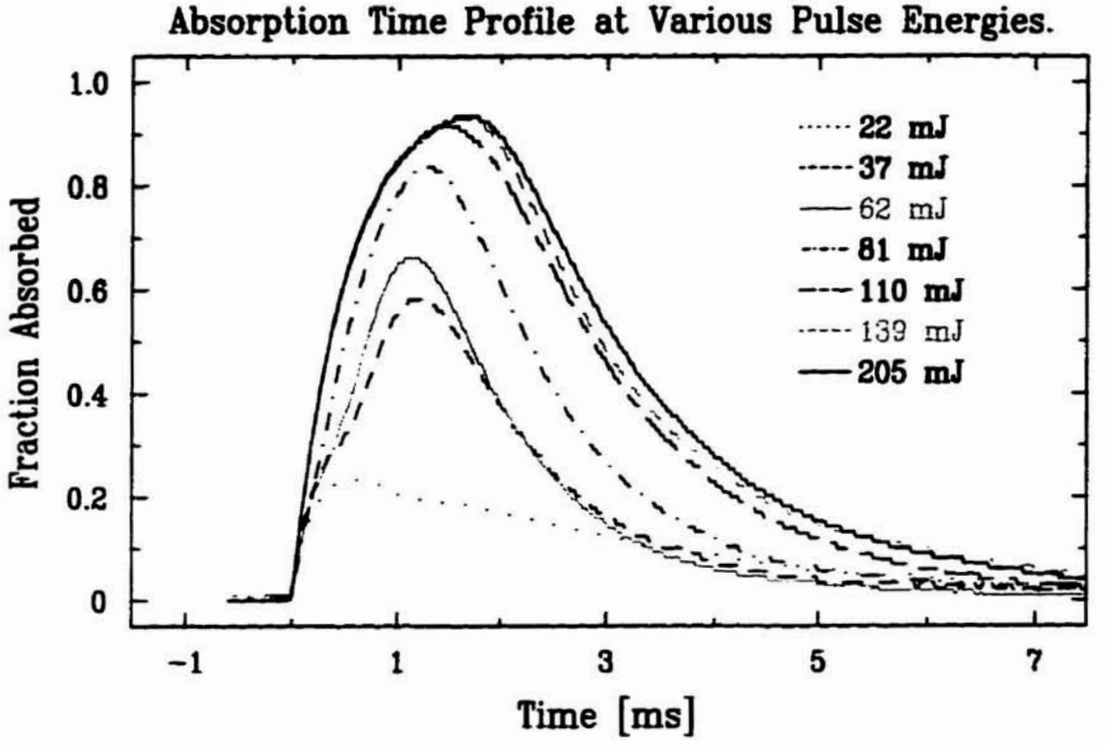

Figure 4.2: Typical absorption profiles of ablated Eu atoms at different pulse energies. The probe beam was perpendicular to the plume propagation at about 1 cm away from the Eu metal surface. 5 Torr of argon buffer gas was used.

4.1.2 Observations

As expected. it was observed that the absorption signal increased when the pulse energy was increased (Figure 4.2). The signal was also sensitive to how tightly the ablation beam was focused. By changing the focus size, we were able to increase the signal significantly for a given pulse energy.

Interestingly. we observed two peaks in the absorption time profile. These were seen even more clearly when the pulse energy was low. (37 mJ) One possible explanation is that these two peaks correspond to a hyper-thermal and thermal beam that often occur in an *invacuo* ablation event[54]. In our experiment. the peaks were probably slowed

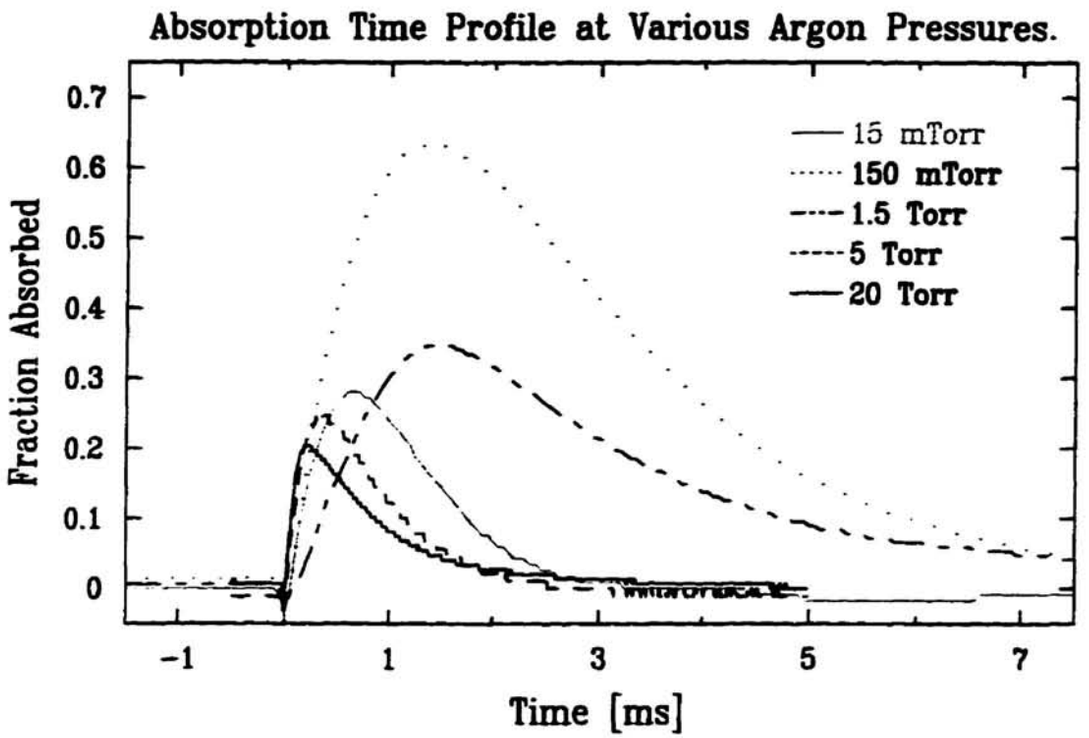

Figure 4.3: Eu ablation signal at various pressures of Ar buffer gas. The probe beam passed perpendicular to the propagation of the plume at about 2 cm away from the Eu metal surface.

down and more spread out due to collisions with background gas (see below).

The absorption time profile changes with the buffer gas pressure. Figure 4.3 shows several time profiles for various pressures of an Argon background gas: similar behavior was observed with a ^{3}He buffer gas. However, the delay between the ablation and the peak arrival was a factor of 4-5 shorter than for the argon buffer gas, and the pressure at which it reached the maximum absorption signal was a factor of 10 higher. This is probably due to the fact that ^{3}He is much lighter than ^{40}Ar and therefore requires about 9 times more collisions for the ablated Eu atoms to thermalize. (see section 3.2.2).

Because ^{3}He is the buffer gas used in the actual trapping experiments, we investigated it in some detail. (See Figure 4.4 and 4.5.) The peak absorption initially

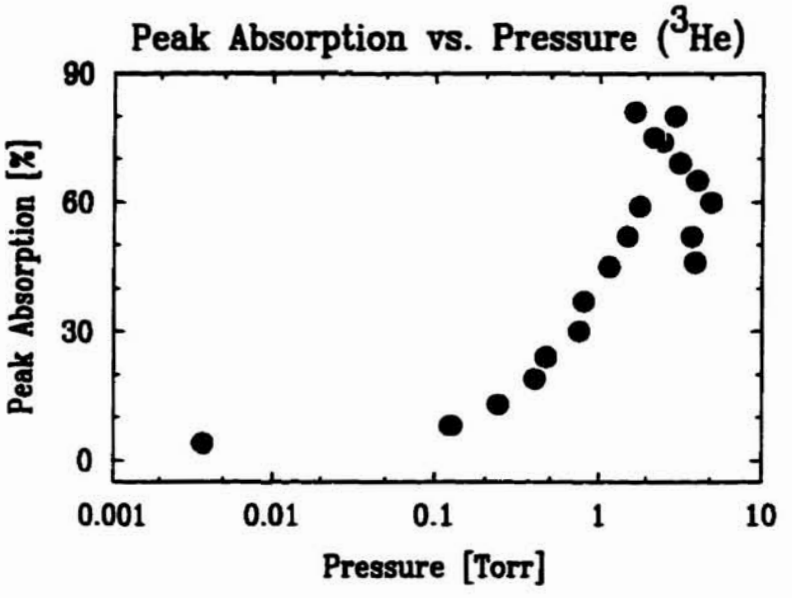

Figure 4.4: The peak absorption vs ^{3}He buffer gas pressure.

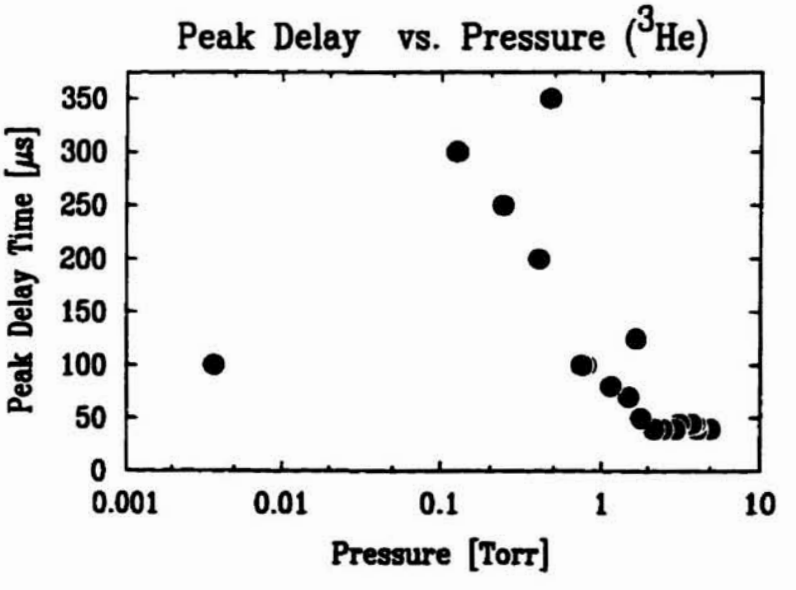

Figure 4.5: The delay time between the firing of an ablation pulse and the arrival of the peak an absorption signal at different ^{3}He buffer gas pressures.

increases with pressure, peaking around ~3 Torr and becoming smaller as the pressure further increases. At low pressures the timescale increased with pressure (consistent with diffusive loss), but above ~500 mTorr the plume disappeared much more quickly. We found in the literature [65] cases where the presence of the buffer gas facilitates dimer and cluster formation of ablated neutral atoms. One possible explanation for our data is that at low pressure, the absorption signal is small because the plume is hot (as indicated by the Doppler broadening.) Because the frequency of the probe laser is fixed, the broadening of the linewidth would then reduce the oscillator strength. Also, at low pressure the density of the plume could be lower because of its larger volume compared to the volume at higher pressure: then the signal would increase with pressure. At even higher pressures, it is likely that neutral atoms begin to form dimers and clusters before reaching the probe beam, resulting in a reduction of the signal.

Analysis of the temporal behavior is consistent with this model. When the pressure is low, the plume travels quickly across the probe beam because the Eu atoms are not fully thermalized. Therefore, the signal lifetime is short and the peak occurs after a relatively short delay time with respect to the ablation pulse. As the pressure increases, the lifetime decreases because the atoms are consumed by dimerization and cluster formation.

In another table-top experiment, the arrangement of the cell was altered such that the ablation laser and the probe laser were parallel to each other. (See Figure 4.6.) The cell was filled with a ^{3}He buffer gas. Figure 4.7 shows a corresponding typical ablation time profile with 100 mTorr of ^{3}He. At this pressure, the presence of the two peaks is more prominent. We surmise that the early peak is due to a nonthermal, ballistic part of the plume and the later peak to the fully thermalized one. We investigated the nature of these peaks further by either taking a spectrum of the fast peak only (by sampling the first 10 μs) or of both peaks together. (by sampling the first 200 μs) the fast peak by and the combined peaks. One can see from Figure 4.8 that the two peaks

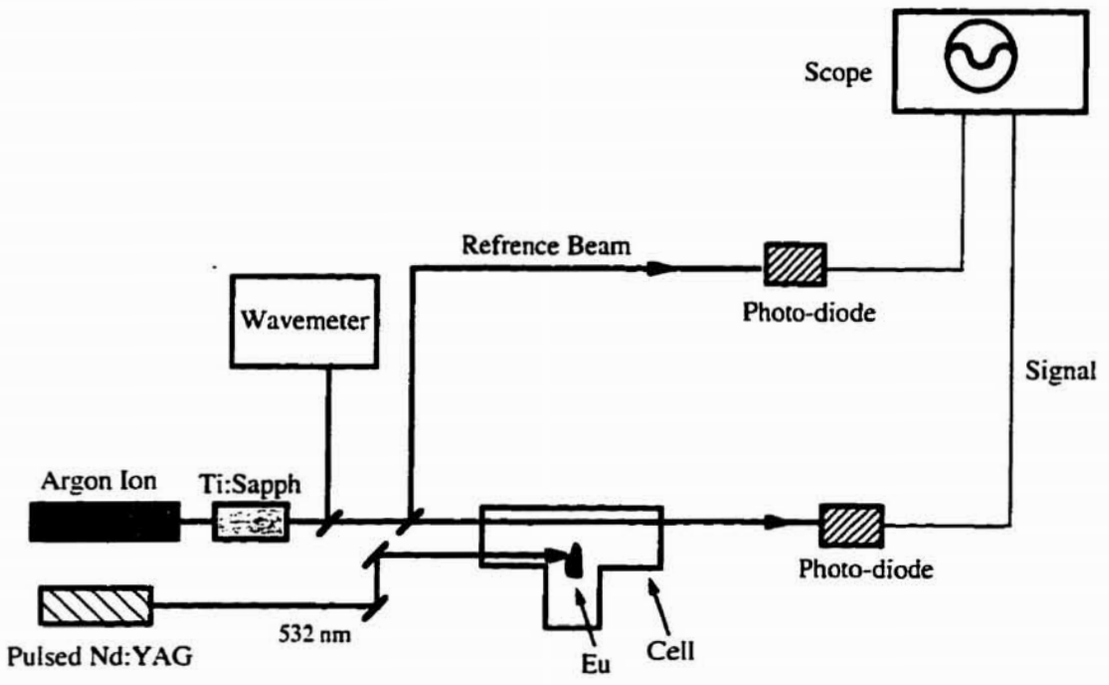

Figure 4.6: A table-top setup for Eu ablation. Note the probe laser in parallel to the ablation laser.

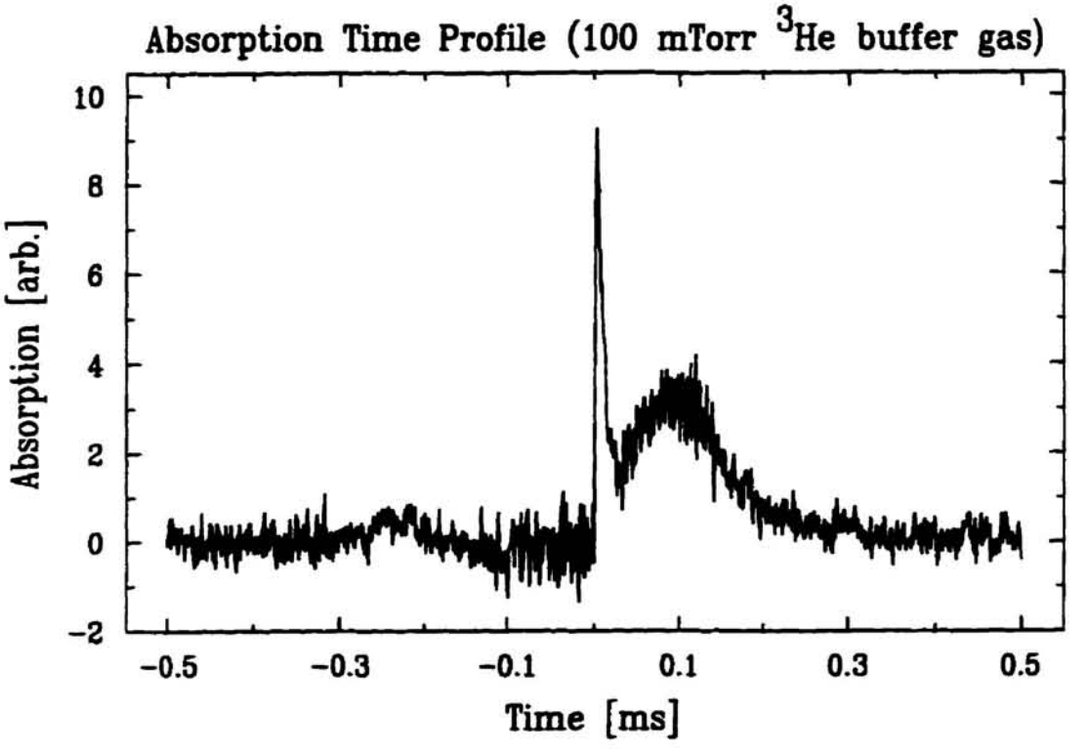

Figure 4.7: A typical absorption time profile at 100 mT of ^{3}He buffer gas. Note the presence of a early narrow signal preceding a wider and slower signal.

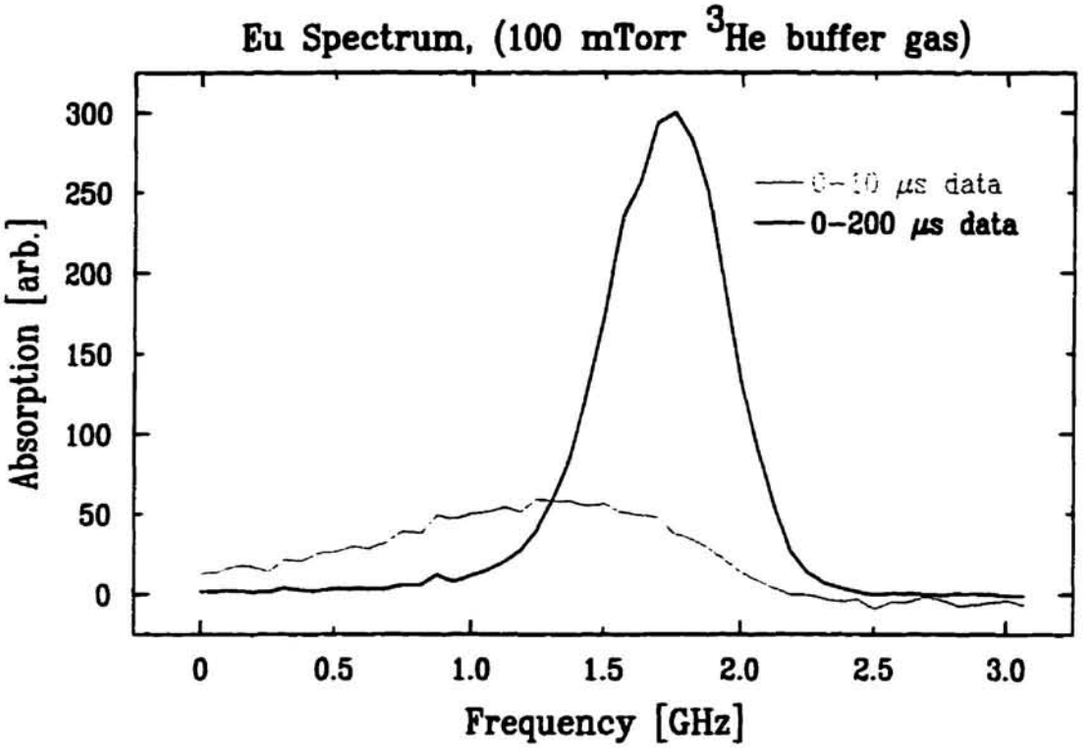

Figure 4.8: Eu spectra from integrating the first 10 μs vs integrating the first 200 μs. The spectra was taken with 100 mTorr of ^{3}He buffer gas. Note the fast traveling peak is red-shifted more than the slow one because atoms move antiparallel to the probe laser beam.

have different widths, 1.44 GHz for the fast peak and 0.63 GHz for the combined peak. The linewidth due to Doppler broadening is given by

$$\Delta\nu_D = 2\frac{\nu}{c}\sqrt{\frac{2ln2\ kT}{M}} \tag{4.1}$$

where ν is the transition frequency, T is the temperature, k is the Boltzman constant, and M is the mass of the atom[66]. This corresponds to a temperature of about 3400±500 K for the fast peak and and about 660±200 K for the combines peak. If we assume the number of atoms in the slow peak to be 10 times greater than the number of the hyperthermal atoms (reasonable assumption given our Figure 4.7), the temperature of the slow peak is ~380 K, suggesting that the thermalization of the Eu atoms is not complete. This is consistent with our model of collisional relaxation. (See below.) At 100 mTorr, an Eu atom undergoes about 60 collisions with ^{3}He on a path of 2 cm whereas about 75 collisions are needed for a thermalization within 10% of 300 K for atoms coming off of a surface at 1000 K (see Chapter 3.2).

The fast peak is red shifted with respect to the combined peak, by 0.62 GHz. One possibility is that this is due to the plume traveling antiparallel to the probe laser. Forward traveling atoms (with respect to the surface of the metal) have a most probable velocity, v_p, given by [11]

$$v_p = 1.22\sqrt{\frac{2kT}{m}} \tag{4.2}$$

At this velocity, the laser frequency is shifted by,

$$\begin{aligned} \delta\nu &= -\frac{v_p}{c}\nu \\ &= -\frac{v_p}{\lambda} \end{aligned} \tag{4.3}$$

The negative sign indicates that the atoms are traveling antiparallel to the laser. Hence the spectrum of the fast peak (3400 K) should be red shifted with respect to the spectrum of the combined peak by 0.58 GHz. This is consistent with our data within 10%.

The tabletop cell allowed us to gain a qualitative feel for what factors influenced the magnitude and duration of the Eu absorption signal. We found the ideal buffer gas pressure was about 1 Torr. The signal or the plume size was the largest when the surface wa

s first ablated. A more tightly focused pulse produced greater yield, but was more susceptible to "drilling". That is, the same spot was repeatedly ablated, material is removed in a more or less narrow cylinder carved into the substrate. Ablated atoms liberated at the bottom of the channel then readsorb in the channel before being liberated into the plume. Hence, when the surface was drilled, the plume size and the signal decreased. The number of pulses required for this depends on pulse energy. To deal with the drilling problem, we simply moved the ablation beam to a fresh spot and readjusted the focus. (Typically after about 20-30 shots of 20 mJ pulse.)

The level of the Eu surface contamination (formation of oxides) also affected our signal strength. Eu oxidizes rapidly in air: we found it tarnishes visibly in 5-20 seconds. In order to provide a clean metal target for the ablation beam, we loaded the Eu samples in a home-built glove box filled with dry nitrogen. The surface of the Eu lump was scraped with a razor blade to expose untarnished metal underneath. Despite our best efforts, in many cases the Eu lump was significantly tarnished by the time we were ready to ablate it.

A clean cell improved the signal significantly (as much as a factor of 2), and we found it helpful to periodically pump out the cell and refill it with fresh ^{3}He, presumably flushing out contaminants.

4.2 Oven

Before the work with ablation a set of experiments was done with Europium in an oven. This allowed an easy way of finding the spectral lines.

Heating in an oven is the oldest and the most popular method of vaporization. Such

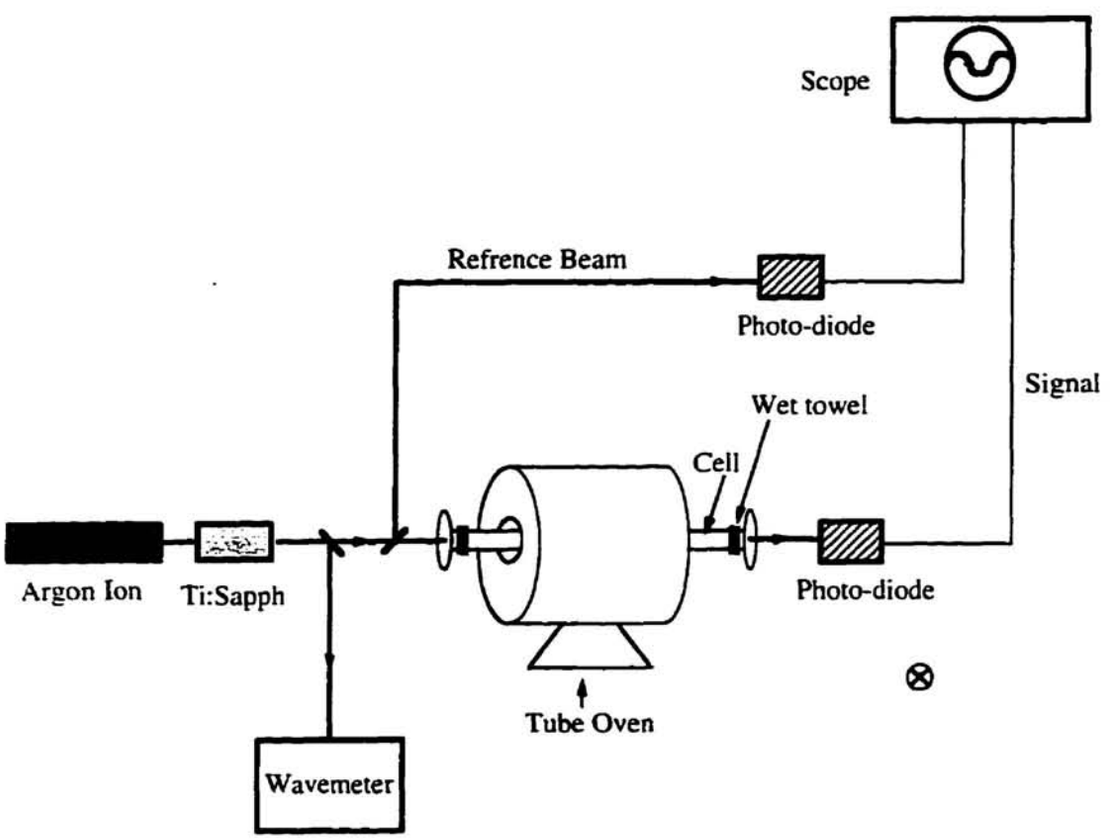

Figure 4.9: Table-top setup for Eu oven spectroscopy

popularity stems from its generality and simplicity. Eu is particularly easy to work with because it is soft and has a low melting point compared to most metals (817 °C). At 500 °C, its vapor pressure is already 1 mTorr[67].

Our first attempts at Eu spectroscopy were done using a simple long stainless tube with windows at each end. The central portion of the tube was placed inside a tube oven (maximum temperature 1200 °C)[68]. At 500 °C, we observed strong Eu absorption signals. We found empirically that the europium had to be heated to a much higher temperature than expected (based on the published vapor pressure curves). (A process called "cracking" as will be explained.) Europium is a highly oxidizing material and readily forms Eu_2O_3 on the surface when exposed to atmosphere, the oxides having a much higher melting temperature than the metal. Although care was taken to expose a freshly cut Eu lump to air as little as possible, some oxides were formed. As a result, it became necessary to heat the lump to the point where cracks formed in the oxide layer, allowing the surface of pure Eu to be exposed. Thus the term "cracking".

It was found that the cleanliness of the cell improved the absorption signal and an effort was made to keep the cell clean. In the end only a few simple precautions were necessary: the cell made out of a clean stainless steel, it was pumped and baked thoroughly, and filled with an inert gas.

Figure 4.9 shows the set-up. The cell contained 1 torr of He buffer gas. The He provided a stable background pressure and decreased the rate at which the windows were coated with Eu. Cooling the tube near the windows helped alleviate coating problems by condensing the vapors on the tube wall before they reach the windows. The absorption spectra are shown Figure 4.10. The data were found to be in excellent agreement with the published spectra [63]. This data gave us an absolute reference point for studying europium ablation and also confidence in our wavemeter.

Despite its simplicity and the successful demonstration of production of Eu vapors, the oven was not considered a viable atom source for the trapping experiment because

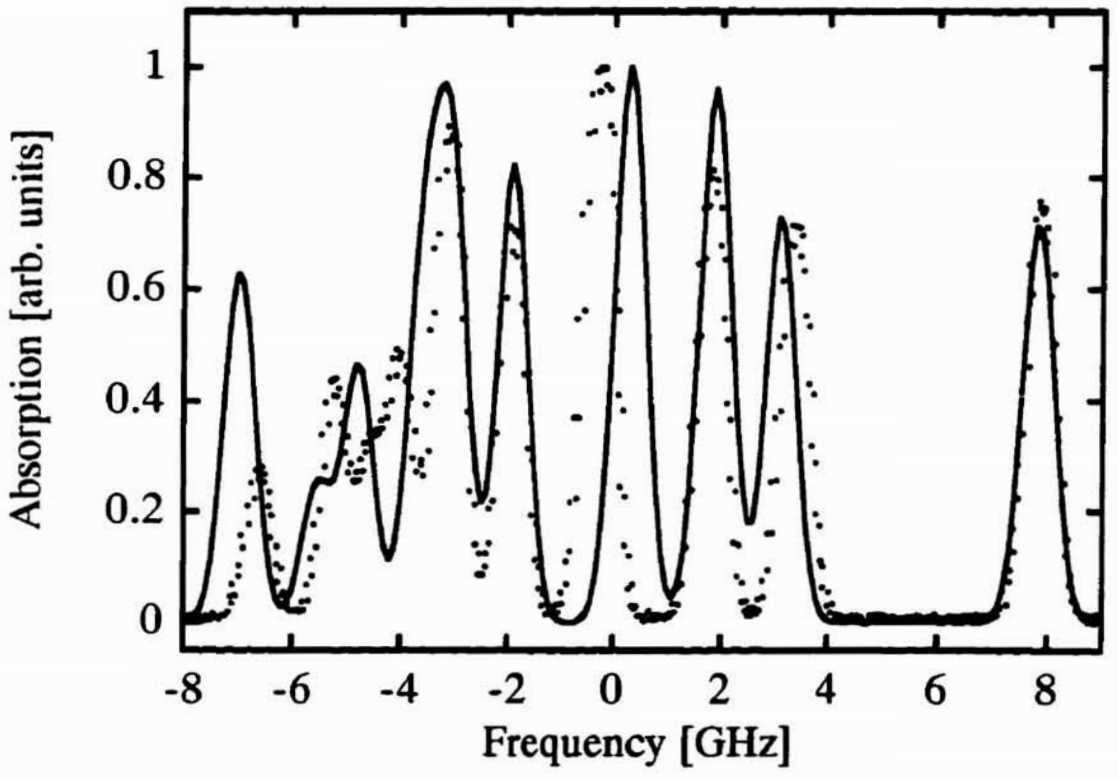

Figure 4.10: Eu spectrum at 570 °C. The data (dots) is shown with the theoretical spectrum (line). The laser was scanned 25 GHz starting at 14067.47 cm^{-1}. The entire scan took 2 s.

of the difficulty introducing the vapor into the cryogenic cell. The oven cannot be placed close to the cell because of the tremendous heat load it would entail. If it were to be placed outside the refrigerator, most of the vapor would condense on the pipe wall before it reached the cell. Although this method would still work, it would be technically difficult. Local heating of the Eu precursor very close to the trap region is much preferable.

4.3 RF Discharge

After successful work with O_2 spectroscopy it was thought that initial tests with the trapping apparatus might benefit from the use of a simpler atomic species. Europium was chosen because of its large paramagnetism (makes it easy to trap) and the high oscillator strength of its visible transitions (makes it easy to detect).

Our initial attempt at creating atoms employed a RF discharge. The discharge creates a europium plasma where a host of different species of particles are released from the precursor, including positively charged ions, neutral atoms, radicals and many different molecules and clusters. These process are not well understood (as with the laser ablation described in Chapter 3.1). RF discharge was our natural choice because in other experiments a low temperature discharge had been successfully implemented to create atomic hydrogen[38].

The first test was done with a table top cell as shown in Figure 4.11. A coil of copper wire(2 mm dia.) was wound 10-15 turns around a glass tube.(2.5 cm dia.) The tube had a window at each end to allow a probe beam to pass through. The tube was filled with a millitorr of either argon or helium buffer gas and the precursor material rested at the bottom of the tube. The coil was excited in the $\lambda/4$ mode and had a primary resonance near 66 MHz. The coupling was made close to critical by tuning the input tapping fraction of the coil while using a directional coupler to monitor the reflected power. When $\approx$10 Watt of power was applied to the coil at its resonant frequency, the

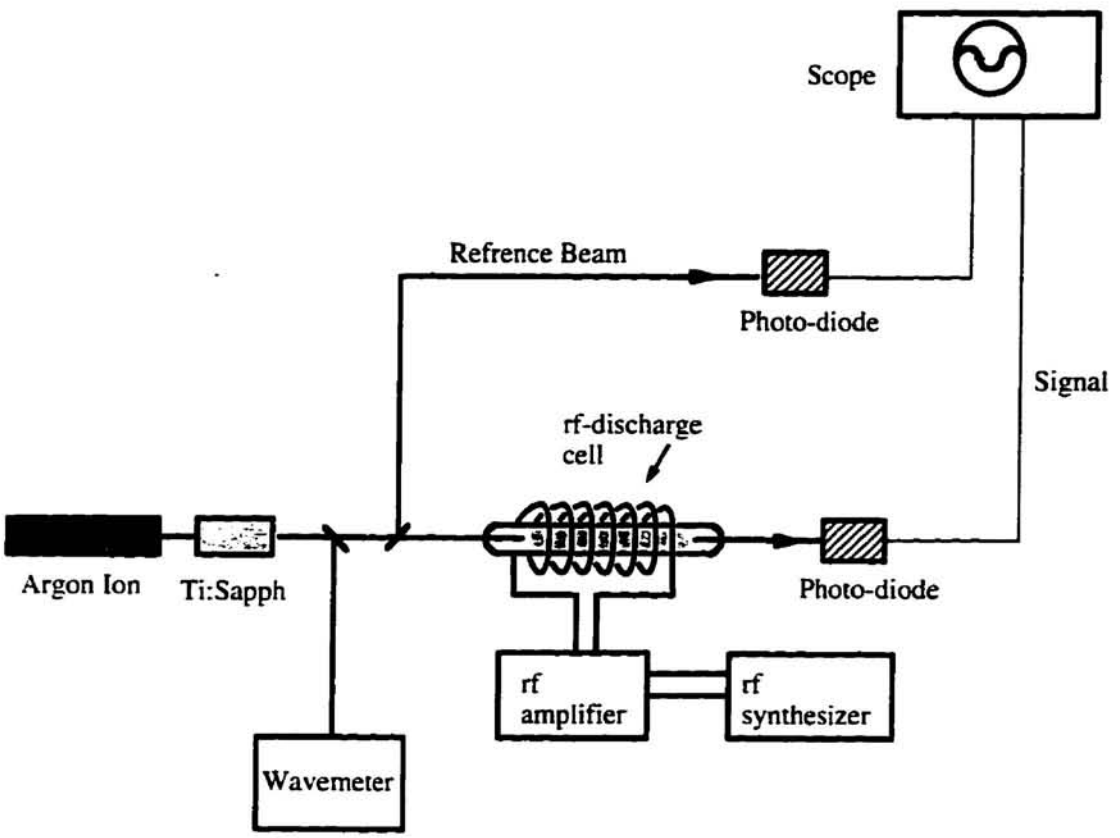

Figure 4.11: A table-top setup for rf-discharge cell.

discharge produced a bright pink glow. (Higher power is needed to start the discharge initially, roughly 40 Watt or so.)

A probe laser beam passing through the glass cell was tuned to the transition frequency of the atoms of interest and the absorbed power was monitored. The laser was also scanned in the region of the known optical absorption lines. Initial attempts at producing Eu vapor in the discharge included using solid Eu metal precursor, powdered particles of Eu metal, and then $EuCl_3$. No signal was seen. We also tried using strip of woven graphite fiber wetted with the solution of $EuCl_3$, similar to the method used in heat discharge experiments[69]. We hoped that spreading out the precursor over a larger surface would increase the interaction between the precursor and the plasma but, again, we did not see any sign of the atomic europium vapor. Later, a different cell was made out of stainless steel Conflat components in order to minimize the amount of glass in the cell as we suspected glass to be more likely to contaminate the discharge. This set-up required the discharge coil to be placed inside the cell, making the design considerably more complicated. Many attempts were made using the new cell with only negative results. This approach to Eu vaporization was then abandoned.

4.4 Spectroscopy of O_2 ($b^1\Sigma_g^+ \leftarrow X^3\Sigma_g^-$)

Although spectroscopy of O_2 is not directly related to the trapping of Eu, this experimental work is included for completeness in the hope it will be useful for future experiments on the trapping of O_2.

Our initial candidate for demonstrating molecular trapping was $O_2(X^3\Sigma_g^-)$. O_2 is naturally occurring, stable, and paramagnetic (2 μ_B, Hund's case (b)). It also offers an electronic transition in the near infrared part of the spectrum (762 nm), easily accessible with our Ti:Sapphire laser. The oscillator strength for this magnetic dipole transition ($b^1\Sigma_g^+ \leftarrow X^3\Sigma_g^-$, Einstein A coefficient of .087 s^{-1}) is too weak to get a reasonable absorption signal under ordinary conditions. However, the long lifetime naturally lends

itself to time resolved fluorescence detection of trapped O_2.

We initially set up a table-top apparatus for doing laser induced fluorescence (LIF) spectroscopy of O_2. (Figure 4.12) The cell built from a CF 4-way cross was filled with pure oxygen gas (99.9999% purity) to 10-40 torr. A probe beam passed through the cell and was modulated with an optical chopper (which turns the beam into a square wave.) and was detected using a photodiode. A cooled photomultiplier[70] tube was placed directly in front of the window located 90° with respect to the probe beam. The signal from the PMT was sent to a preamplifier. amplifier and then to a multichannel scaler(MCS).

In order to successfully apply LIF to O_2, several difficulties had to be overcome. First. the Ti:Sapphire laser had to be isolated from the atmosphere. When exposed to the atmosphere (the normal situation), the laser did not lase at the resonant frequencies of oxygen. Absorption by oxygen molecules in the cavity lowered the gain at these frequencies (relative to other competing modes). The problem was solved by placing the laser cavity inside a nitrogen-filled box with holes cut out for the input pump beam and exit probe beam. The box was flushed and then slightly over-pressured with dry nitrogen.

Second. it was discovered that nonradiative quenching of the excited state is very sensitive to the presence of nitrogen and organic impurities in the cell[71]. Without a clean cell and pure oxygen gas, the fluorescence was quenched by non radiative processes and no measurable signal was detected. The use of 99.9999% pure oxygen gas and a freshly pumped out UHV-grade cell led to success. The cell had to be pumped out periodically and filled with fresh oxygen gas because the gas slowly became contaminated with impurities. presumably emanating from the cell walls. In the case of fluorescence measurement. major effort is required to reduce the background light. In order to reduce the room light into the PMT[70], the experiment was carried out in dark. For reducing the scattered laser light into the PMT. two sets of 6 (or sometimes 7) baffles were placed

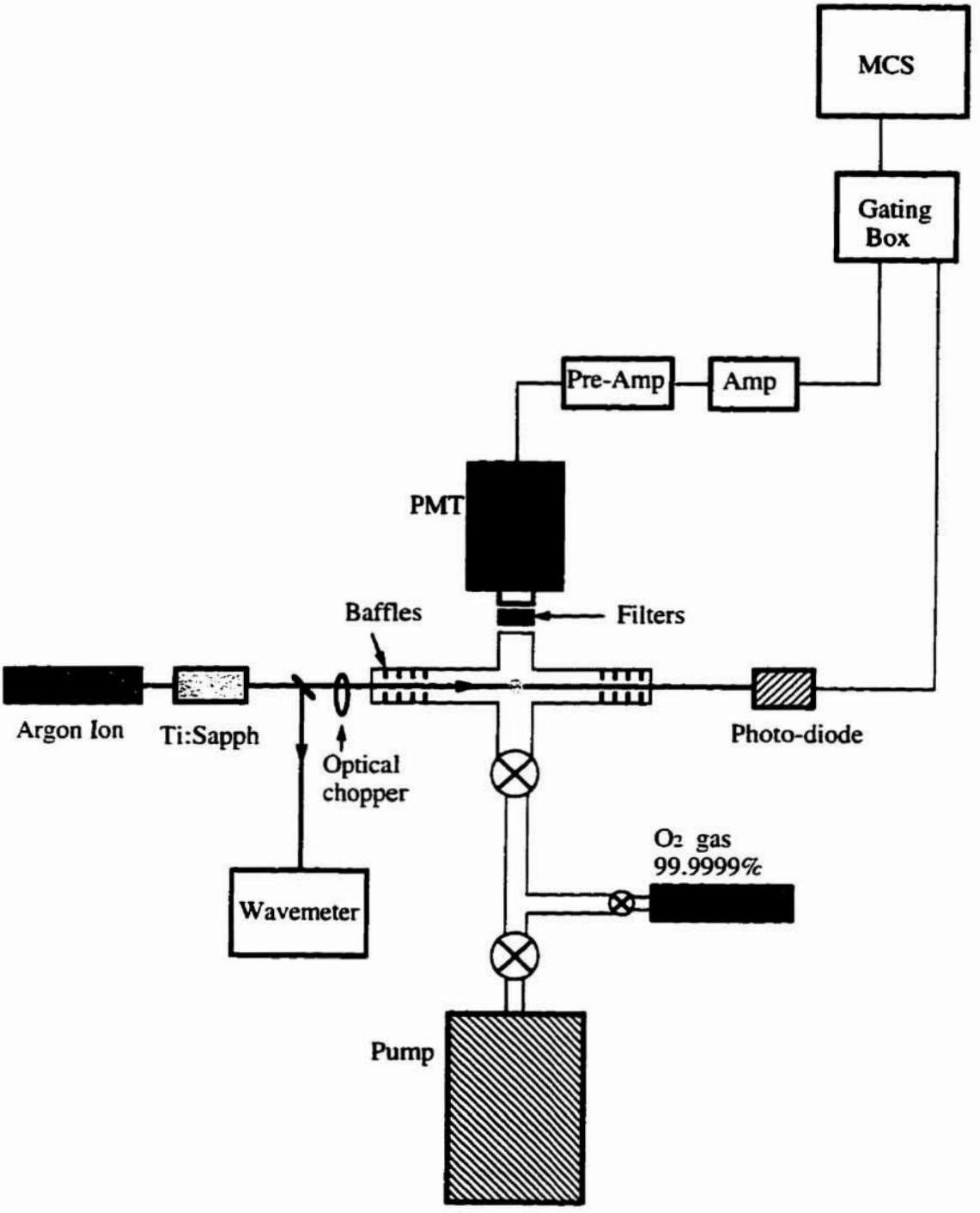

Figure 4.12: A table-top setup of laser induced fluorescence (LIF) spectroscopy of O_2

between each probe-beam window and the cell. The baffles were made out of aluminum disks with 5 mm holes at the center and were anodized black[72]. Our initial cell used Brewster windows, but it was found this did little to reduce scattered light.

Efforts were also made to reduce the dark current of the PMT. This was accomplished by avoiding exposure of the cathode to the room light and by cooling the tube. By keeping the PMT in the dark for several hours and cooling it to -20° C, its dark count rate was reduced to less than 25 counts/s.

4.4.1 Data Taking

Data was taken either using (a) time resolved LIF technique or by (b) continuous LIF.

(a) For the time resolved fluorescence detection, the laser beam was modulated with a mechanical chopper. After passing through the cell, the beam was detected by a photodiode. The photodiode signal was converted to a TTL signal using a comparator. Using a home made gating device, this signal was converted to a variable-width TTL signal with an adjustable delay. The MCS board counted pulses only when the laser beam was off.

(b) The $b^1\Sigma_g^+(\nu' = 0)$ excited state can decay either to the original ground vibrational state with $\nu'' = 0$ or to the vibrational state $\nu'' = 1$. Roughly 7% of the fluorescence photons are due to $\nu' = 0 \rightarrow \nu'' = 1$ transition and their frequency corresponds to 863 nm[71]. This makes it possible to do continuous LIF using cut-off filters that block the excitation frequency and transmit the fluorescence of 863 nm. By placing a stack (2 to 4) of specially coated filters(0.1% transmission for 762 nm, 85% transmission for 863 nm for each filter[73]) in front of the PMT, we were able to remove most of 762 nm photons and detect only 863 nm photons with a signal-to-noise ratio better than 100 for an integration time of 500 ms.

The laser power used was different for each method. Typically 5 to 20 mW was used for time resolved fluorescence and 200 mW to 300 mW for continuous LIF. (Before

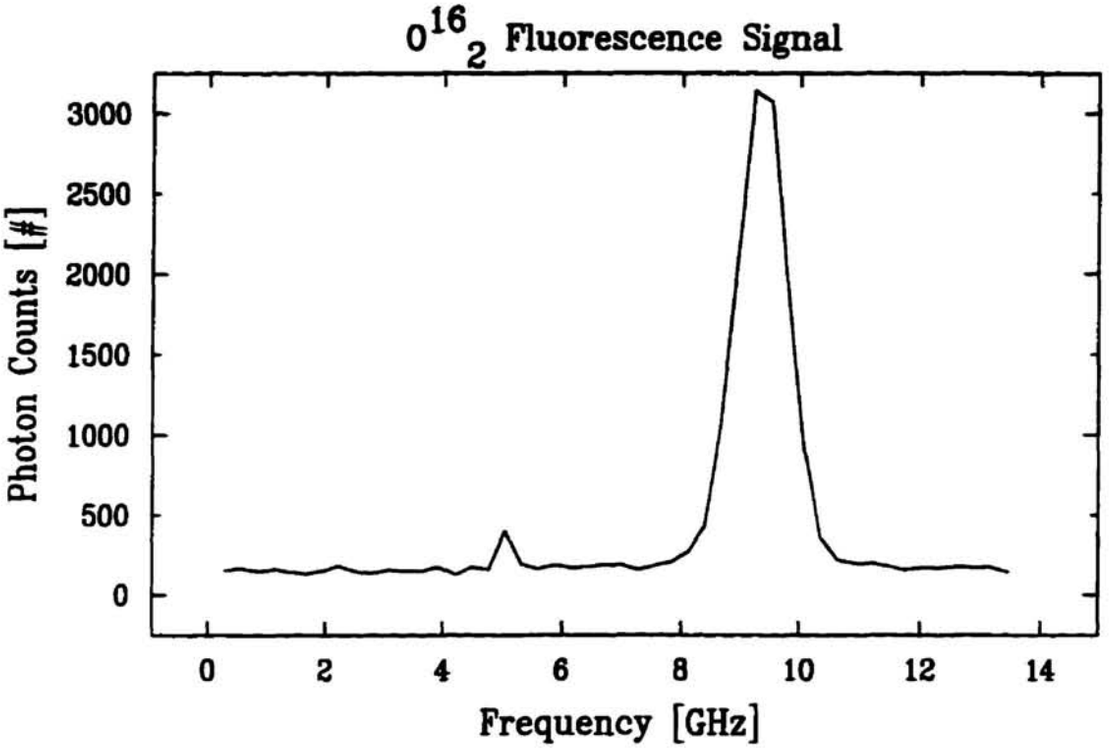

Figure 4.13: Fluorescence signal of $^{16}O_2$ molecules. The pressure inside the cell was 13 Torr.

each run. the beam power was adjusted appropriately so that the electronics were not saturated. In extreme cases of electronic saturation. increasing the power decreased the count rate due to pulse pileup.)

4.4.2 Results

Figure 4.13 shows a typical spectrum obtained by scanning the laser over 14 GHz about 13118.036 cm^{-1}. (J:1→0, K:1→0, ^{P}P branch[74]). The linewidth shown here is ~1 GHz. This agrees reasonably with expected Doppler broadening of 0.6 GHz and a pressure broadening of 0.5 GHz. We also detected $^{16}O^{18}O$ at 13141.537 cm^{-1} (J:7→7, K:6→7, ^{R}Q branch) [74] which has 0.2% natural abundance.(Figure 4.14) By increasing integration

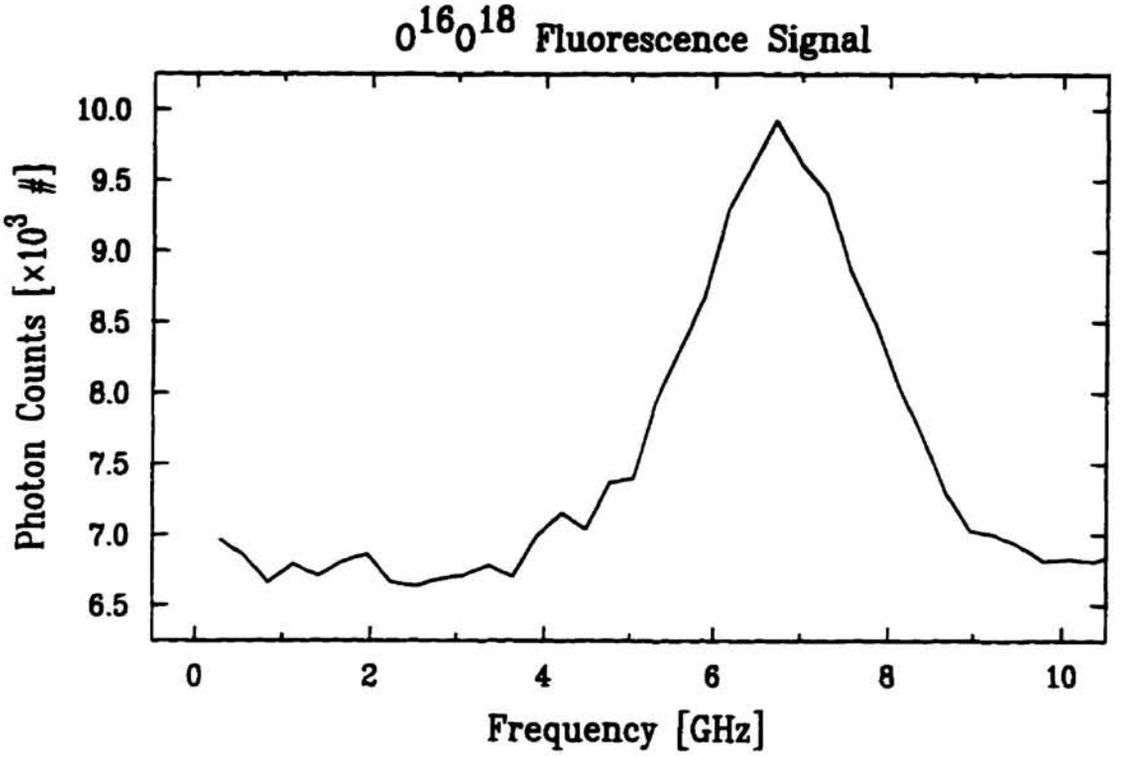

Figure 4.14: Fluorescence signal of $^{16}O^{18}O$ molecules. The pressure inside the cell was filled with 11 Torr of oxygen gas.

time by a factor of 120 (to 12 s). we were able to achieve the same signal to noise ratio as 13118.036 cm^{-1} line.

As mentioned above, the signal would deteriorate, presumably due to impurities desorbing from the cell walls. Figure 4.15 shows the deterioration of the signal over a period of 800 s.

We also found that the fluorescence signal was sensitive to variation in pressure. Below 5 Torr of O_2, the signal was small because not enough molecules were excited and also, perhaps, because the contaminants could more easily diffuse to the center of the cell. Above 200 Torr, presumably nonradiative self-quenching of oxygen reduced the signal. (See Table 4.1).

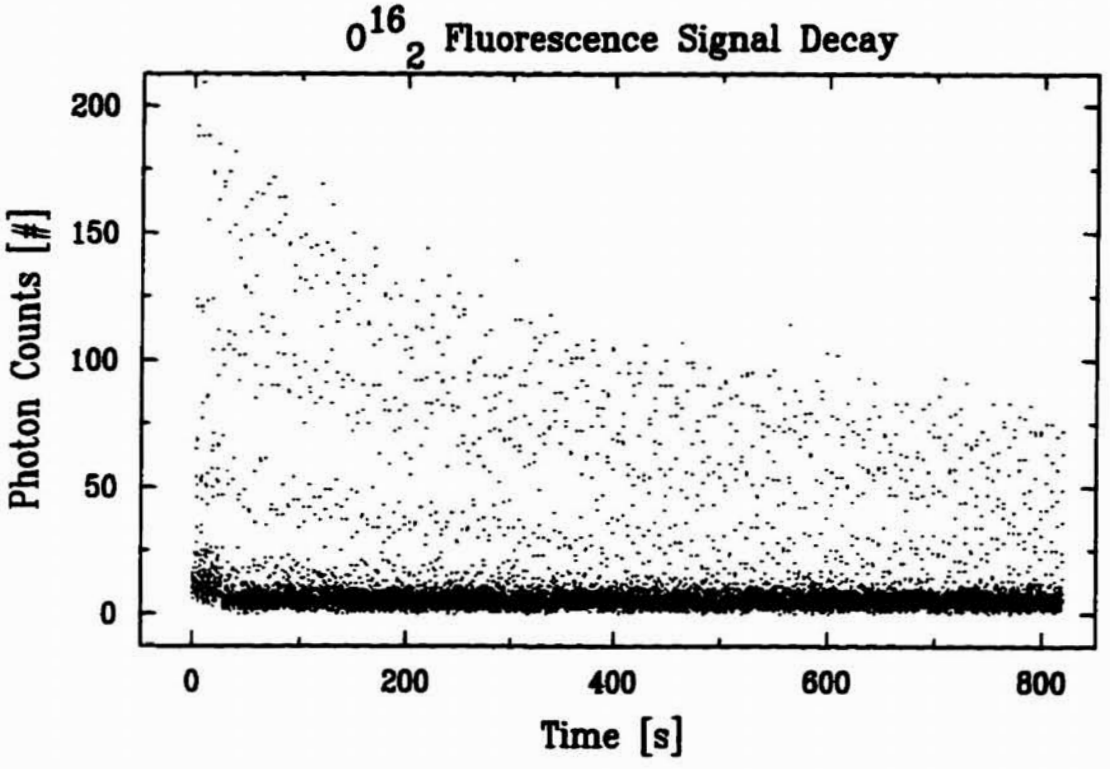

Figure 4.15: Decay of O_2 fluorescence signal over time. The laser was scanned 14 GHz at 0.2 Hz around a resonant frequency (13118.036 cm^{-1}) and the signal was monitored continuously for 800 s. The decay is probably due to contamination of O_2. The cell was initially filled with 13 Torr of 99.999% chemically pure oxygen gas. The resolution of this plot is insufficient to resolve individual peaks, but the maximum fluorescence can be seen to be dropping significantly.

P(Torr)	Counts	Linewidth (GHz)
495	245	4.5
228	390	-
92	490	2.0
46	586	-
20	305	1.1
11	150	1.1
4	57	1.1
1.8	20	1.1

Table 4.1: Fluorescence counts vs. Pressure. The measurements were made by filling the cell with the oxygen to 500 Torr and pumping it down to smaller pressure values in a single run. The pressure is measured with a convectron gauges[75] and they are unadjusted values.

Chapter 5

Experimental Procedure

5.1 Apparatus

In this section, the experimental apparatus is described. The apparatus can be divided into two main parts: the cryogenic cell assembly and the optical system. The cryogenic cell is surrounded by the superconducting magnet that produces the trapping fields. The center of magnetic trap is in the center of the cryogenic cell. The cell is connected rigidly and thermally to a dilution refrigerator. The optical system consists of an ablation laser for producing atomic vapors, a probe beam for doing absorption spectroscopy of the trapped atoms, and photodetectors for measuring the absorption of the probe beam. A simplified schematic of the experimental setup is shown in Figure 5.1.

5.1.1 Cryogenics

The use of a cryogenics in the experiment, especially the employ of a dilution refrigerator, requires that the experiment to be very well planned and efficiently executed. The cost of helium($\approx$\$150/day) is a major factor. Besides the cost of helium, the low temperature components and technologies are custom and thus refits are doubly expensive. Also the behavior of some materials and devices are not well understood. Cooling down and

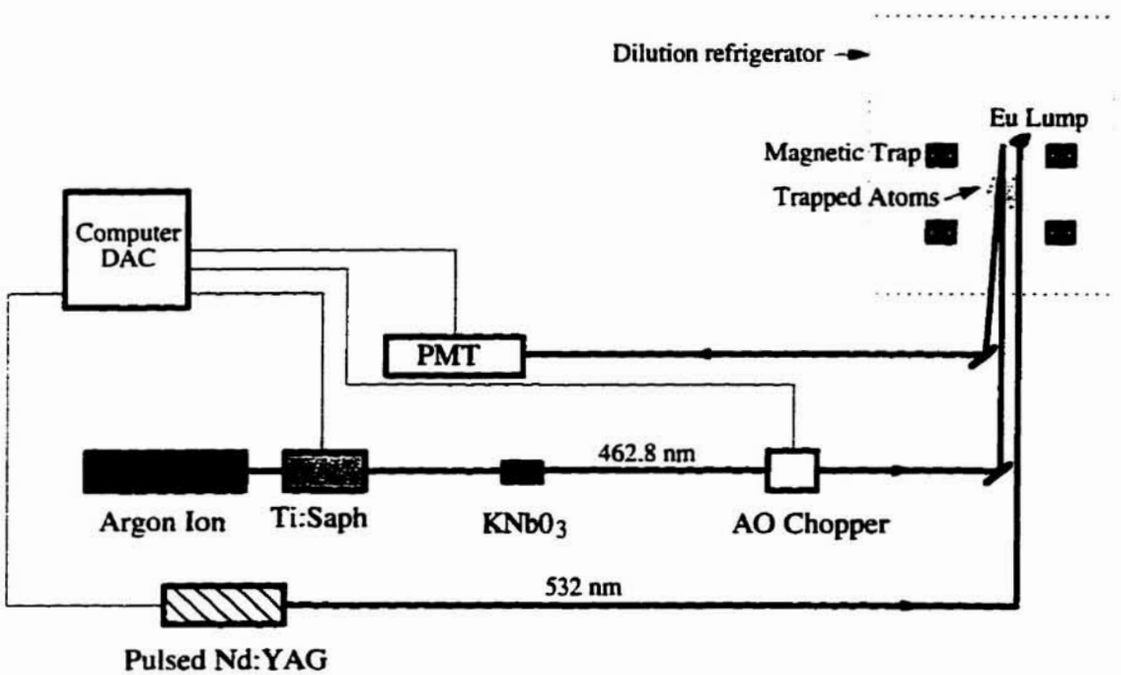

Figure 5.1: A schematic diagram of the experimental setup.

warming up the refrigerator takes 2-3 days and about 1 person-week. This puts some constraints on the flexibility of the experiment. Making a change to the cell is impossible to do during a run. Similar considerations put restrictions on the cell design and the optical access to the cell.

Despite these drawbacks, the dilution refrigerator makes many aspects of buffer-gas loading more straight-forward; a wide and low temperature range can be accessed. Also, because even the best magnetic traps would offer depths of not more than about 5 Tesla, only a 3.5 K deep trap is possible for 1 μ_B species. This is important because "incipient trapping" (an atom lifetime of 1 s) starts to occur when the temperature of the atoms are 10 times lower than the trap depth, making it necessary to have a buffer gas at 350 mK or lower.

The restriction of loading temperature eases with higher Bohr magneton species (and, therefore, greater trap depth). In fact, a simple He pumped cryostat with operation temperature around 1 K may be sufficient for trapping atoms with high magnetic moments[76]. Such a system is attractive because of the low production and maintenance costs, smaller size, and, perhaps best of all, much shorter turnover time compared to a dilution refrigeration system. This is currently being implemented and will be tested in the near future for atomic species such as Eu, Gd and Ho (magnetic moments $> 5\ \mu_B$).

One important side benefit of using a cryogenic system is the facility of achieving very high vacuum. Unlike a room temperature magnetic trap, which often can have a problematic atom loss due to collisions with the background gas, a cryogenic cell can easily achieve a gas pressure of $< 10^{-20}$ Torr by simple cryopumping.

Another advantage is the natural inclusion of a superconducting magnet.

Dilution Refrigerator: Theory of operation

A brief description of the principle behind a dilution refrigerator is given here (For more detailed description see ref. [77]). When a mixture of ^{3}He and ^{4}He is cooled below a

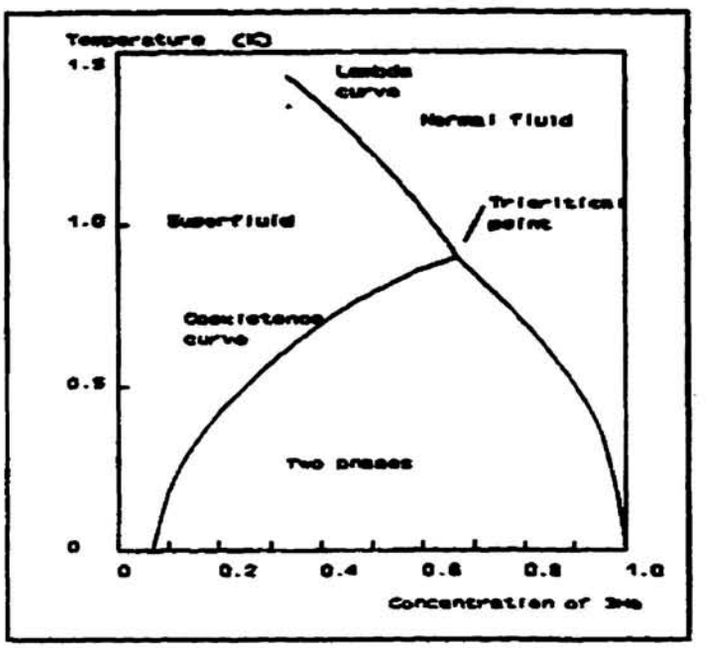

Figure 5.2: A Phase diagram of ^{3}He and ^{4}He mixture at low temperature

critical temperature $\approx$ 0.8 K, it separates into two phases; the lighter "concentrated" phase which is rich in ^{3}He and the heavier "dilute" phase which is rich in ^{4}He. The concentration of ^{3}He in each phase is dependent on the temperature as shown in Figure 5.2. Because the enthalpy of ^{3}He in the two phases is different, cooling can be obtained by evaporating ^{3}He from the concentrated phase into the dilute phase. This is accomplished by pumping on the dilute phase which, in turn, preferentially removes the lighter, higher vapor pressure, ^{3}He. As the ^{3}He in the concentrated phase crosses over to the dilute phase to establish an equilibrium, energy is removed and cooling takes place. The closed pumping cycle forces the ^{3}He mixture back to the mixing chamber where the mixture is condensed and separates into two phases.

Cooling power decreases with the temperature but remains finite even near 0 K because the concentration of ^{3}He in the dilute phase remains finite. A schematic diagram

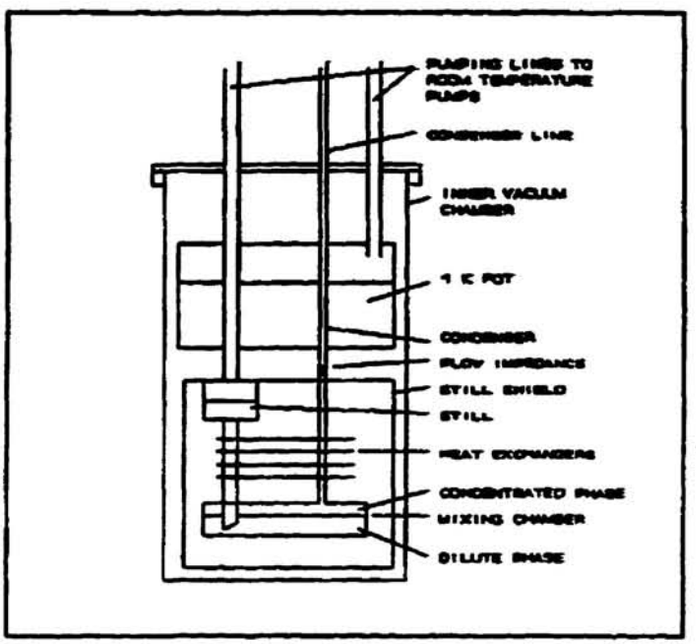

Figure 5.3: A schematic diagram of a dilution refrigerator.

of a dilution refrigerator is shown in Fig 5.3. The dilute phase of the mixture has a liquid vapor boundary in the still where ^{3}He is evaporated and pumped away. The vapor travels through the closed pump system and is forced back into the dilution unit through the inlet line which is thermally anchored to the 1 K pot. The 1 K pot holds liquid ^{4}He and its temperature is maintained close to 1.3 K by pumping. After the vapor is cooled to 1.3 K, it travels through a flow impedance which condenses the vapor to liquid. As it passes through the heat exchanger, its temperature falls even further. It then enters the mixing chamber. The sample to be cooled is either mounted directly on the mixing chamber or is connected to it via a heat link. The entire unit is separated from the liquid helium bath by an inner vacuum chamber.

Our ^{3}He-^{4}He dilution refrigerator is a Kelvinox 300 made by Oxford Instruments with the nominal cooling power of 300 μWatt at 100 mK. Our initial test showed also

300 μWatt at 100 mK and a base temperature of 15 mK. Later, when the dilution refrigerator was modified to have an optical access, the additional heat load due to blackbody radiation from the room limited the lowest accessible temperature to about 70 mK.

Dilution Refrigerator: Schematic

Figure 5.4 shows a typical Kelvinox 300 dilution refrigerator inside the dewar and the physical dimensions. (Our dilution refrigerator was modified to provide a space for the magnet, cell and optical accesses.) There are two places where vacuum has to be maintained: the Dewar vacuum which is used for insulating the liquid nitrogen jacket from the room and also between the nitrogen jacket and the helium dewar. A high vacuum gas handling system with a diffusion pump backed by a rotary pump was used to pump out the dewar vacuum. The Inner Vacuum Chamber (IVC) insulates the dilution unit from the liquid helium. A UHV gas handling system with a turbo pump backed by a dual stage rotary pump was used for pumping on the IVC and the cell.

Three different types of thermometers were employed for monitoring the temperature during a run. A silicon diode thermometer, model DT-470 from LakeShore, was mounted on the top of IVC flange and was used for monitoring the temperature of the dewar. The diode is sensitive from room temperature down to 4 K. Calibrated thermometers monitored the dilution refrigerator. These were supplied by Oxford along with calibration charts for each of the different thermometers. They were ruthenium oxide resistors that were calibrated against a primary thermometer [78]. Their resistance was measured with a resistance bridge [79]. The resistance of the RuO_2 thermometer increases with decrease in the temperature. RuO_2 thermometers are convenient, inexpensive and can be used over a wide temperature range, typically from 1 K to 50 mK. RuO_2 thermometers were also used for monitoring the temperature of the cell and the ^{3}He can.

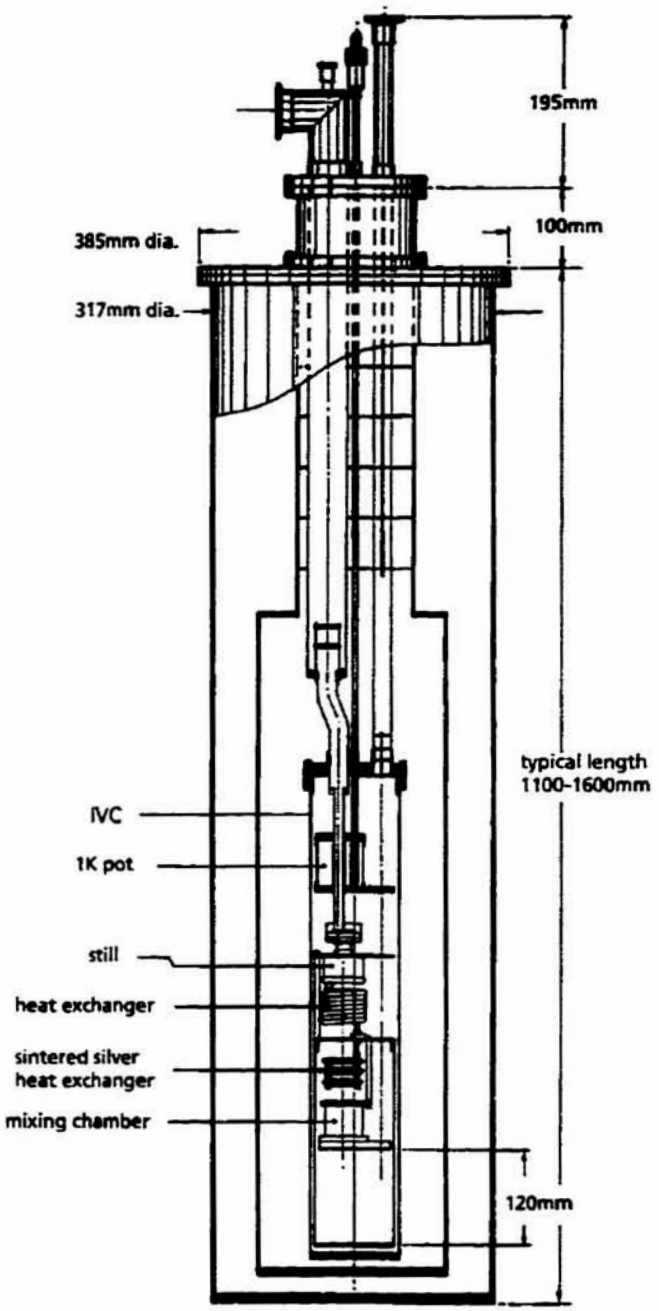

Figure 5.4: A typical dilution refrigerator. Our dilution refrigerator has more space below the mixing chamber for the magnet.

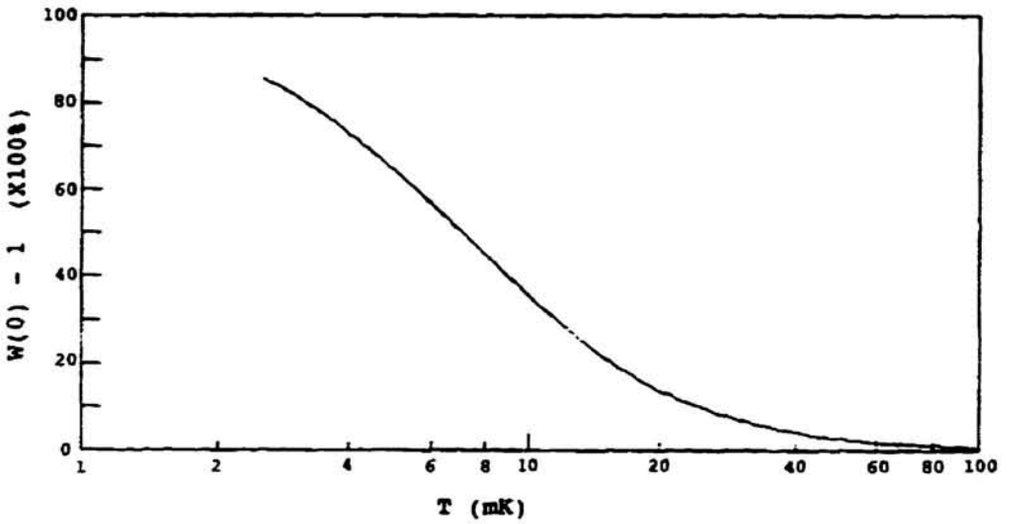

Figure 5.5: Anisotropy of ^{60}Co radiation vs. Temperature.

To measure temperature accurately below 80 mK, a nuclear orientation thermometer was employed. A Co^{60}Co crystal was mounted on the mixing chamber and a gamma detector (a photo-multiplier tube with a scintillator) was positioned outside the dewar. At low temperatures (< 5 mK) the ^{60}Co nuclei are almost entirely aligned with the high internal magnetic field of the ferromagnetic crystal, and the gamma radiation is highly anisotropic. At high temperatures, (> 80 mK) the nuclei are completely unaligned, and the gamma radiation is isotropic. The ratio of radiation rates between the on-axis and off-axis positions [or warm vs. cold counts on-axis] is therefore a good indicator of temperature between 5 and 80 mK (See Figure 5.5)

During initial test of the refrigerator we calibrated the resistance thermometers with the nuclear orientation thermometer over the 5-50 mK range.

The temperature of an object is accurately measured only when a good thermal contact between the thermometer and the object is established. When mounting our

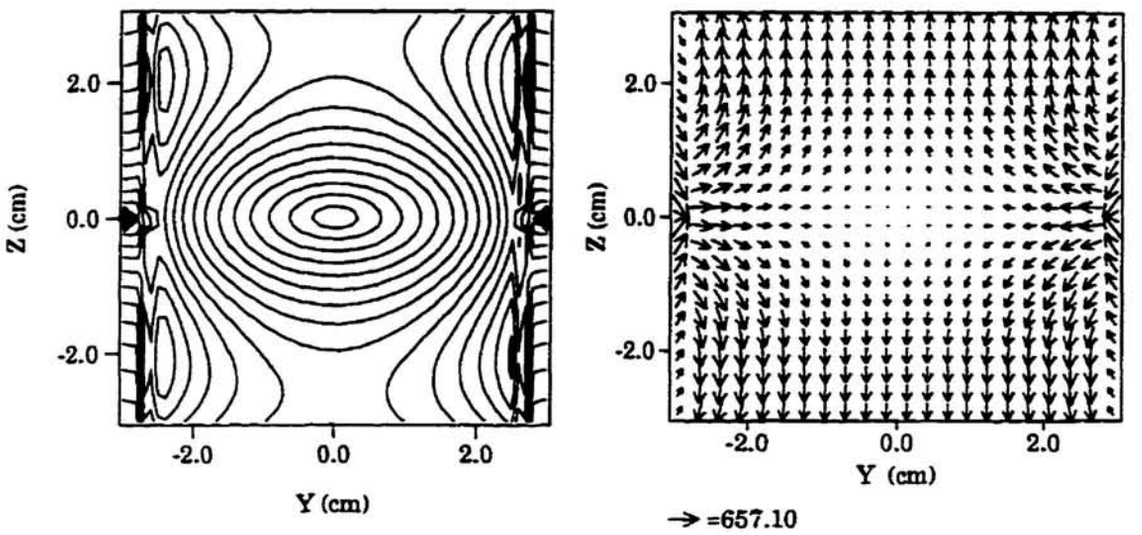

Figure 5.6: Contour map of the constant magnetic field magnitude and the direction of the field's orientation. Z-axis is the axis of symmetry. The scale of the arrow given at the bottom represents the field strength in units of Gauss for 1 A in the magnet. The field strength varies linearly with the current in the magnet.

thermometers, we polished the mating surfaces smooth and applied enough pressure such that the surfaces pushed strongly against each other. We also used high thermal conductivity materials such as copper with reasonably large surface areas. Epoxies were also used for mounting the thermometers directly to certain surfaces.

5.1.2 Magnet

The magnetic trapping field is generated by two superconducting solenoids run in the anti-Helmholtz configuration. This creates a spherical quadrupole field and hence provides an elliptical confinement of atoms around the trap center.(Figure 5.6) This ellipticity is due to the steeper z-axis field gradient, where the z axis is the axis of symmetry. One reason for choosing the anti-Helmholtz configuration (as opposed to, for example, the Ioffe configuration) is the simplicity of construction and operation. Another

advantage, although not really important to these experiments, is that the spherical quadrupole field provides the tightest confinement of trapped atoms in all three dimensions. The potential is linear with the distance from the origin. This can play a role in determining certain aspects of evaporative cooling. Although an Ioffe type trap provides close to the same confinement, such a trap is technically more difficult to make.

The anti-Helmholtz configuration has some disadvantages compared to other trap geometries. The only change that can be made to the magnet is the change of the field strength. The field geometry is preset and cannot be altered. In the case of density-limited trapping, more atoms can typically be trapped in a properly designed Ioffe geometry because of its large trap volume.

Also, the anti-Helmholtz configuration system has a zero field at the center which cannot be removed by simply adding a bias field. A zero field can induce loss of trapped atoms via Majorana spin flips and will limit the lifetime of the trapped atoms in the absence of other loss mechanisms. Despite these drawbacks, the anti-Helmholtz configuration system was used in these initial experiments due to its technical simplicity.

Magnet Construction

The individual solenoids are wound around a titanium bobbin with 5.08 cm clear bore[80]. All the titanium used in the construction of the magnet is 6-4 ELI annealed. Both solenoids are 2.77 cm thick with an inner and outer diameter of 5.3 and 13.0 cm respectively and 2.83 cm in length. Their centers are separated by 3.3 cm and there are approximately 5220 turns for each solenoid. The wires used are multifilamentary NbTi (niobium-titanium) embedded in a copper matrix (2 twists/inch). The use of twisted multifilamentary wires help eliminate the flux jumping that can occur in single filament conductors.

The magnets are wet wound in epoxy to inhibit the movement of the wire (due to Lorentz forces). To counter the huge force repelling the two coils apart when run in the

anti-Helmholtz configuration, the magnet is encased in a titanium cask (again 6-4 ELI annealed alloy). The cask was designed to withstand more than 2.5 $\times 10^5$ N without plastic deformation or failure. The particular titanium alloy was chosen because it has been carefully characterized at low temperature and is relatively light weight.The entire magnet assembly is immersed in liquid helium. Vapor-cooled current leads are used to lower helium boil-off.

Prior to the experiment, the magnet was tested inside a helium dewar and was "trained". Training consists of increasing the current until the magnet quenches. With each quench, the wire moves closer toward its equilibrium position and therefore the quenching field initially increases and then asymptotes toward a stable value. When the magnet quenches, the resistance of the superconducting magnet suddenly increases to its normal value and heat is generated as the energy stored in the magnet is dumped into the (normal) wire. Rapid boiling of the liquid He typically ensues. (This can be dangerous if the exhaust for the He bath is not properly set-up to handle the sudden increase in pressure.)

If a quench were to occur during the running of the experiment, it would not only increase the cell temperature (due to Eddy current heating) but also shut down the dilution refrigerator (due to the rapid temperature increase), disrupting the experiment. Therefore, it is necessary to know the quenching current of the magnet before the refrigerator is turned on and to stay safely below that current. During our magnet training, the magnet was quenched seven times at currents of (in chronological order) 65 Amp, 79.2 Amp, 86.2 Amp, 86.1 Amp, 86.1 Amp, 83.9 Amp, and 86.3 Amp. At 86 Amp, the trap depth is 3 Tesla making it possible to trap atoms with magnetic moment 1.5 Bohr magneton or higher at 250 mK. (See Chapter 3.2.1.)

5.1.3 Cell Assembly

The cell assembly is comprised of three main sections: the heat link, ^{3}He can and cell. Figure 5.7 shows a cross section of the apparatus. As shown in Figure 5.7, there are two separate heat links. A copper rod of 2 cm diameter connectes the mixing chamber and the ^{3}He can and a second copper rod of 1.3 cm diameter provides thermal anchoring from the top of the cell to the mixing chamber. This design was employed in order to have the ability to maintain two separate temperatures in the ^{3}He can and the cell. The mating areas of the heat links were gold plated for better thermal contact.

The purpose of the ^{3}He can was to allow the helium buffer gas to be cryopumped out of the cell. By lowering the temperature of the ^{3}He can, the buffer gas can be cryopumped into the ^{3}He can region, thus, hopefully, ensuring no future interference with the trapped atoms in the cell. The ^{3}He can has 21 holes of size 5 mm dia. with depth 5 mm for increasing the surface area. It is connected to the cell by a thin-walled stainless steel tube (2.54. cm dia., 0.0508 cm thickness) which allows gas to flow freely between the cell and the can. A buffer gas is introduced to the ^{3}He can and to the cell through a 1/8 inch stainless steel tubing with the wall thickness of 0.7 mm. The tube which originates at from room temperature is thermally anchored at 4 K and at 1 K before reaching the ^{3}He can. It is coiled in order to prevent room temperature radiation from making it to the cell and to limit ballistic travel of gas from the room temperature end of the tube into the ^{3}He can.

The cell is positioned at the center of the magnet. It resides in vacuum and is separated from the magnet (and the liquid helium) by a stainless steel vacuum can. The vacuum can, a tube of 5 cm diameter and 0.8 mm wall thickness, is directly around the cell. The cell has inner and outer diameter of 4.27 cm and 4.5 cm respectively and is 6.8 cm long. It is made of OFE copper with 4.4 cm diameter fused silica window attached at the bottom [81] (described in detail below). A special design was required for the window at the bottom of the cell. Because the thermal expansion coefficients are

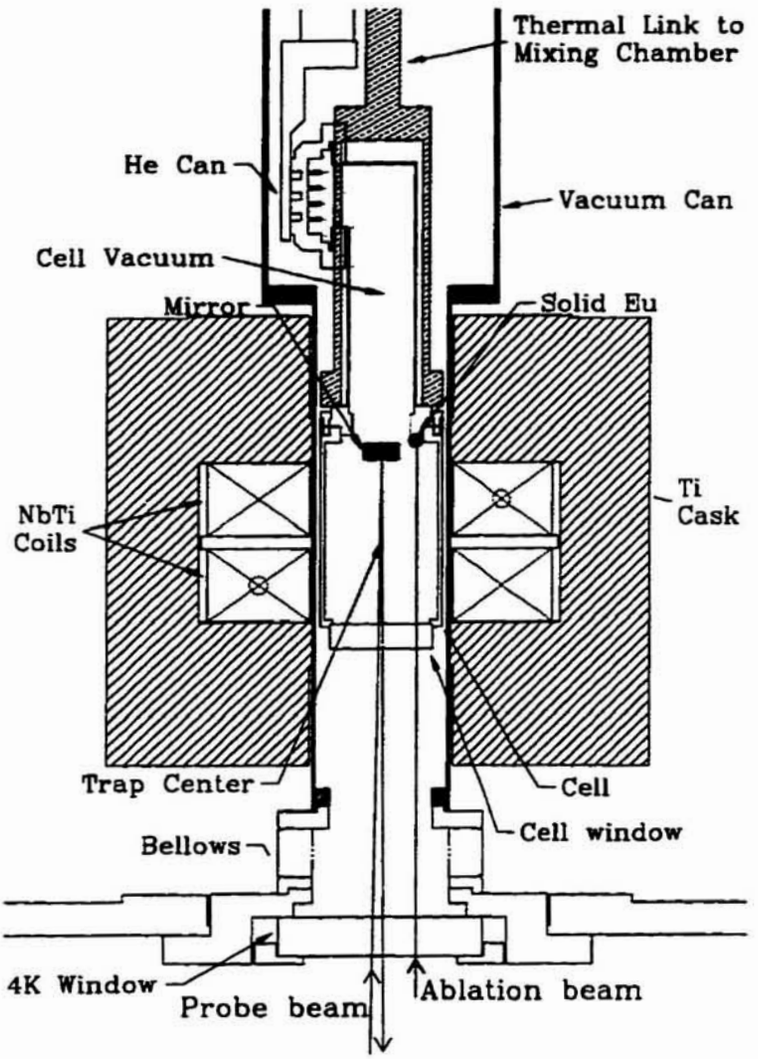

Figure 5.7: Schematic diagram of magnetic trapping and optical detection apparatus. The superconducting magnet is immersed in liquid helium. Optical access to room temperature is provided by a set of borosilicate and fused silica windows at the cell temperature, 4 K, 77 K and 300 K. Only the 4 K window is shown in the figure. The 77 K and 300 K windows lie directly below the 4 K window. The YAG beam and the probe beam enter the same set of windows.

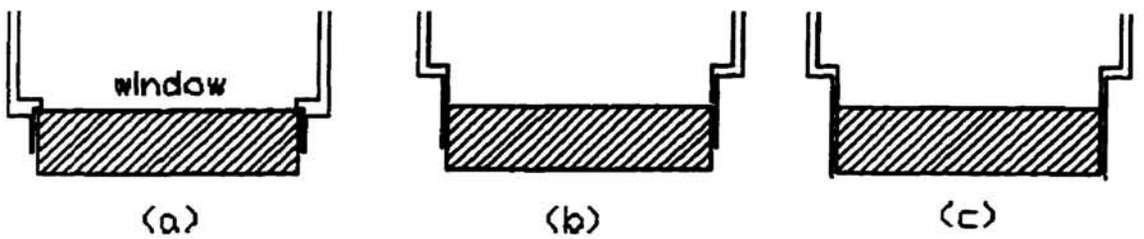

Figure 5.8: Different designs employed for attaching window at the bottom of the cell. (a) and (b) caused the window to shear into an upper and lower piece when the temperature of the cell was lowered below 77 K. The problem was solved by by making the fin longer and thinner (as shown in (c)).

different for copper and fused silica, a very high stress can develop if care is not taken. In our first cell design (Figure 5.8(a)), the window was sheared parallel to the face of the window and separated into an upper and lower section as its temperature was lowered below 77 K. Undoubtedly this was due to the stress from the copper contracting on the window. Two things were concluded from this initial failure. First, the copper fin that was in contact with the perimeter of the window should be made as thin as possible in order to minimize the radial force on the window. Second, the fin seal should cover the full thickness of the window, not half way. In a later design, the fin was machined to less than 0.13 mm thickness and covered the entire thickness of the window. (See Figure 5.8(c).)

A 1 cm diameter aluminum on BK-7 mirror is mounted on top of the cell for retroreflecting the probe laser beam. Next to the mirror and opposite to each other are two sample holders made out of copper. Solid lumps of Eu and Gd were mounted inside. (Initially, Gd was also considered for trapping.)

During initial runs, we found that the cell swayed from side to side due to unavoidable vibrations from pumps, etc. This was indicated by movement of the retroreflected beam that, in turn, induced noise on the absorption signal. Because the dilution refrigerator

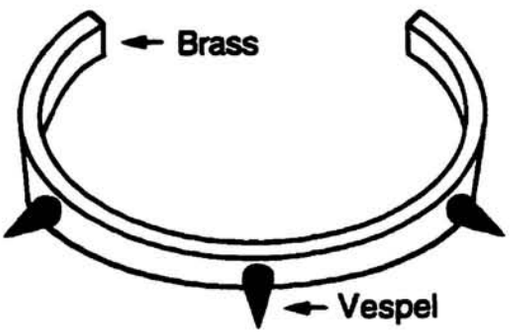

Figure 5.9: Cell centering device (the "dog collar"). The tip of the sharpened vespel rods are in contact with the IVC wall but due to a poor thermal contact, the heat load on the cell is negligible.

was hung from the top, at the end of a long lever arm, the cell was particularly sensitive to vibration. We also discovered that the cell moved when the magnet was ramped up or down (possibly due to magnetic force on the lump of Gd, which is ferromagnetic). In some cases, this caused enough displacement such that the cell touched the vacuum can and this led to intolerable heating of the cell. To remedy this problem, a device which resembles a dog collar was put around the cell for centering it with respect to the IVC (shown in Figure 5.9). It was made of a brass ring with 3 Vespel-22 [82] rods screwed to the ring. Vespel was chosen for its low heat conductivity[83]. The rods were sharpened to less than 0.35 mm dia. in order to minimize heat conduction between the vacuum can and the cell. With the dog collar, there was much less oscillation. The additional heat load through the vespel rod was estimated (and determined vial experimental tests) to be less than 10 μW.

In order to provide optical access the dewar and the IVC were modified. This was done by installing a set of three windows; the first window separated room from OVC, the second window was thermally anchored to the nitrogen jacket and the 4 K window separated the OVC from IVC. The 77 K and 4 K windows block IR that would otherwise

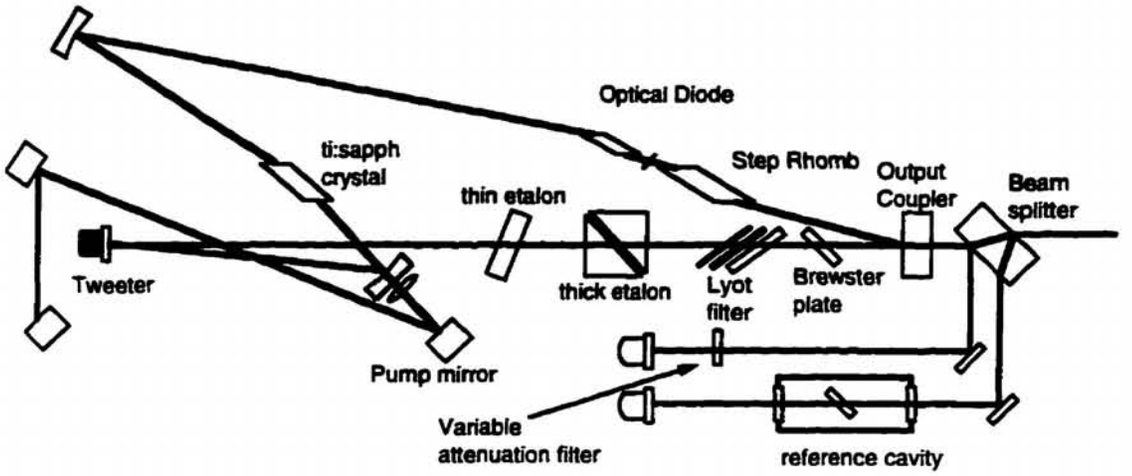

Figure 5.10: Schematic of Coherent 899 ti:sapphire laser with active stabilization.

cause intolerable heating on the cell. The 4 K window was made of uncoated laser grade BK7 glass. This was chosen because BK7 has somewhat lower IR transmission (in 3-4 μm regime) than fused silica. The 77 K and the room temperature windows were made of laser grade fused silica anti-reflection (AR) coated at 760 nm. (These were originally specified for fluorescence detection of trapped oxygen molecules.)

5.1.4 Ti:Sapphire Laser and doubling crystal

For the probe laser beam in infrared region, we used a ti:sapphire laser with a tuning range from 700 nm to 1000 nm. This was pumped with an Argon Ion laser, a Coherent I-200 Argon Ion laser (maximum power of 25 W), 15 W, multiline, and an aperture setting of 10 (for the best Gaussian beam) was typically used.

The Ti:sapphire laser is a model 899-21 CW ring laser from Coherent with active frequency stabilization.(See Figure 5.10.) The output beam is linearly polarized along the vertical direction and is 0.2-1 watt depending on the operation wavelength. Two electronically controlled etalons ensure single-frequency laser operation with a linewidth of less than 20 MHz. The frequency can be further stabilized to less than 1 MHz using

an electronic servo system that locks the laser frequency to a stable passive reference cavity. With the scanning Brewster plate placed in the laser cavity, the frequency of the laser can be scanned up to 25 GHz.

The power fluctuation of the laser is approximately 15%. A noise eater (a laser intensity stabilizer, Thorlab CR200-B, max. input power 25 mW, operating wavelength 700-1000 nm, 4 kHz bandwidth) was sometimes used to stabilize the beam power (~2%) which helped eliminate one source of noise from our absorption signal.

Frequency jumping was, at times, a more serious problem. It can be caused by vibration, air currents, gain loss due to absorption by molecules in air, mistuning of electronic components, failure in the feedback system, unstable lasing positions on the mirrors, and misalignment of the reference cavity. It can also occur if the laser frequency is set in a region between two adjacent modes with equal gain coefficients. When the frequency of the laser does not lock reliably, all these possible culprits have to be systematically tested and ameliorated to ensure proper scanning and maintaining a single-frequency operation. The wavelength of the emitted laser light was determined by splitting part of the beam into Bureleigh WA-20VIS Wavemeter.

In order to probe the stronger (see Table 3.2) Eu transition at 462 nm, the ti:sapphire beam was doubled from 925.7 nm by passing it through a $KNbO_3$ crystal. The crystal was cut at an angle of 51 degree to the c-axis to satisfy the phase matching condition for 925.4 nm[84]. The crystal is effective at doubling over a wavelength range of ± 20 nm. It was mounted on a rotational stage for angle tuning. Because the crystal is sensitive to pressure and can be easily damaged, care must be taken during mounting. The first and second harmonic beams were separated from each other by passing it through a prism after which the first harmonic was removed.

The conversion efficiency of the doubling crystal varies with the input beam power. For 1 Watt input power, the conversion efficiency is low resulting in only a few microwatts of 925.4 nm power. However, this was sufficient for doing absorption spec-

troscopy of Eu.

5.1.5 YAG Laser

Laser ablation of Eu was achieved by employing a pulsed doubled Nd:YAG laser[85].A fourth harmonic generator (BBO) was present in our unit. (The fourth harmonic was used for a different experiment.) With this setup three different wavelengths are produced; 1064 nm, 532 nm, and 266 nm. These beams are separated from one another by a set of dichroic mirrors.

For safety and convenience, we chose the 532 nm beam for laser ablation. At 532 nm, our eyes have high sensitivity. White cards and very low laser powers can be used to guide the beam easily without requiring a visual aid. The pulsed YAG at 532 nm has a temporal width of $\approx$ 5 ns and the maximum energy of 250 mJ per pulse. The energy per pulse can be varied by adjusting Q-switch delay time (the time between the firing of the flash lamp and the Q-switch). (See Figure5.11.) The pulse can be generated as a single shot (triggered externally) or in a continuous train at 10 Hz. The shots can be fired either manually (with a pushbutton) or electronically (with a TTL pulse). The pulse power fluctuates $\pm$20%. The pulse power was measured by using a glass slide to reflect 8% of the beam into a pulse power detector[86].

It should be noted that only specially coated mirrors, beam splitters and beam dumps that are designed to withstand the intense laser power should be used for guiding the ablation laser[87]. (50 MW/cm^2.) Other mirror types such as Al-coated mirrors got damaged when hit by the pulse laser.

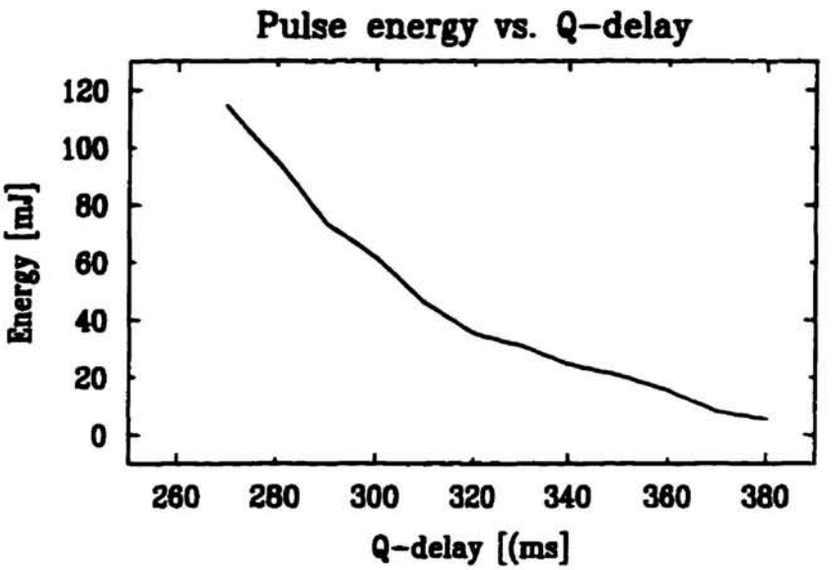

Figure 5.11: Pulse energy vs. Q-delay time. (Note: As the flash lamp deteriorates this dependence changes.)

5.2 Detection Method

5.2.1 Detectors

For most beam detection in the experiment, detectors based on the photovoltaic operation of UDT PIN-6DP photodiodes were used. In photovoltaic mode, there is no external bias voltage across the photodiode. This allows greater sensitivity to low light levels albeit with a lower frequency response. The detector circuit design is as shown in Figure 5.12. R_F, and C_F were chosen to compromise between maximum signal amplification and maximum frequency response.

During the detection of trapped europium atoms, the probe beam power was often reduced below a small fraction of a microwatt to prevent optically pumping the atoms out of the trap. For measuring absorption at this low light level, the photodiode detector was replaced with a photo-multiplier tube. A bialkali photo-multiplier tube[70] was operated in current mode for this purpose. In current mode, the average DC current

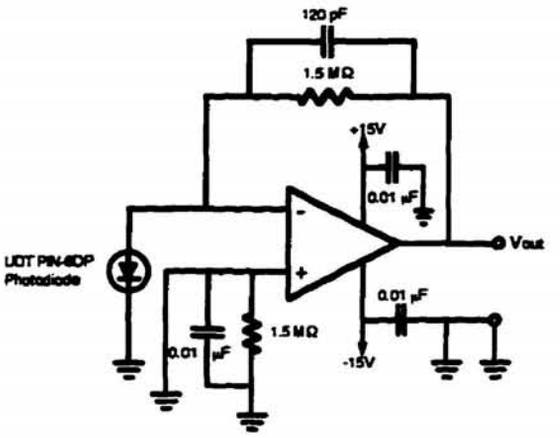

Figure 5.12: Circuit Diagram of the photodiode detector (in photovoltaic mode).

signal from the tube is converted to a voltage signal with a resistor. The voltage signal was then sent to a preamplifier for amplification before it was displayed on the oscilloscope.

Scattered light from the YAG beam can be problematic causing saturation in these detectors. The 532 nm YAG photons are filtered out by placing RG-655 (for 710 nm probe laser) or BG-12 (for 462 nm) Schott glass filters in front of the detectors.

5.2.2 DAC System

The data acquisition system consisted of the following components: a CAMAC timing module, an oscilloscope, a function generator, and a computer. The timing card, the oscilloscope, and the function generator was interfaced to the computer using GPIB (IEEE 488.2). A sequence of triggering events were controlled by a CAMAC timing module[88]. The module has an internal 1 MHz clock. Each of its 12 channels can be programmed to execute time related TTL signals. The unit has the ability to output a different 12 bit word at any fixed time up to 16,777,215 clock intervals, with a minimum interval of 1 μsec. The timing card was used for triggering acousto-optic module (AO) (sometimes used for switching the probe laser), YAG laser, and the oscilloscope. The

event sequences were transferred to the timing card through a GPIB module in the CAMAC crate.

The laser power level (the absorption signal) was recorded with a four channel, 500 MHz, 8-bit digitizing oscilloscope[89]. The digitized data from the scope was transferred via GPIB to the computer for storage and analysis.

A function generator[90], was used for scanning the laser frequency. A saw tooth shaped voltage wave from -5 V to $+5$ V was connected to the external sweep input of the laser control box. The laser frequency could be scanned by as much as 25 GHz. The function generator was triggered by the timing card.

5.2.3 Data-taking Sequence

Three different data acquisition (DAC) sequences were used during the experiment.

Time Profile

For studying the density of atoms in the trap, the laser frequency was fixed at the resonant frequency with the highest absorption, and the scope monitored the time profile of an absorption signal. The sequence used was as follows:

- A baseline (zero absorption reference) for the absorption signal is acquired for 1-100 sec with the scope.
- The YAG laser is fired and atoms are ablated.
- The scope begins sampling data (one channel for the absorption signal, another channel for the reference beam, and a third channel for monitoring the temperature of the cell)
- After the scope stops(1-150 sec), the data is downloaded to the computer.

The pulse energy of the YAG laser at a fixed Q-delay has poor repeatability unless it is warmed up. The flash lamp is therefore flashed at 10 Hz for 20 sec before the actual

laser pulse is fired. The cell temperature is recorded by sending the analog output from the resistance bridge to the scope.

Spectrum

The Eu spectrum over all visible lines is necessary for determining the absolute density of Eu in the cell and for identifying which states are trapped. Other information such as the temperature of the atoms, the position of the probe beam may also be obtained from the spectrum data. The DAC sequence for taking the spectrum can be done in either the pulse-and-sweep mode (for taking a snap shot of the spectrum some delay after the atoms are ablated.) or the fast sweep mode (for studying spectral evolution of the trapped atoms over a long period). The pulse-and-sweep mode proceeds as follows:

- The laser is set on external control. In this mode the frequency of the laser can be controlled by an external ±5 V analog signal. We typically scan 1-8 GHz. Initially the input is set to -5 V, the low end of the range.
- After being warmed up, a single pulse of the YAG laser is fired.
- The scope is triggered after a (typically 3 sec) delay from the YAG firing. The delay is present with the idea to allow untrapped and marginally trapped Eu atoms to escape.
- The laser is frequency scanned about 1 sec. The scope records the scanning voltage, the reference beam power, and the signal beam power during the scan.
- The scope data is downloaded to the computer.

The fast sweep mode has the following sequence:

- The laser is set on external control, as above.
- A triangle wave (-5V to 5V) at 5-10 Hz is sent to the laser.

- The scope is set up to be triggered on the rising edge of the triangle wave. The scope is usually run in "average mode". In this mode, 10-30 scope traces are averaged

The following sequence is repeated.

- A reference scan is taken (no atoms in the trap) to correct for etalon effects. (Etalon effects came from the many entrance windows to the cell.)
- The scope is reset and the average is cleared.
- The YAG laser is warmed up and fired.
- After a delay to allow for sufficient averaging, the data is downloaded.

It should be noted that this procedure records the average spectrum over a significant time, so strict interpretation of time-varying spectral features must be done with care. This mode enabled us to monitor the change in the spectrum of the Eu atoms in the trap continuously, and provided us with our cleanest data. (See Figure 6.2)

5.3 Buffer Gas Loading of Eu

A typical, actual loading procedure is described here. More detailed discussion of variations on this will be described in the results section. First, a torr of ^{3}He or ^{4}He Gas is introduced to the cell at room temperature. This enough to provide the saturated vapor pressure at below 1 K. (See Figure 3.3.)

The cell is cooled to 250 mK for ^{3}He and 800 mK for ^{4}He. The magnet is energized to 15 Amps (0.52 Tesla) for ^{3}He and 50 Amps (1.7 Tesla) for ^{4}He. This creates a potential deep enough to trap only the M_J=7/2 state. The probe laser is set on the center of one of the absorption lines of Eu. The typical power used to probe the atoms is 0.1 μW. The 3.5±1.5 mm diameter beam enters at an angle about 2° with respect to the cell axis and passes through the cell center with an offset of 3±1.5 mm. The beam

then reflects from the mirror at the top of the cell, passes the cell center again, exits the cell, and is detected by a photo-multiplier tube. A YAG pulse of approximately 15 mJ ablates the solid Eu creating Eu vapors. The pulse energy was kept as low as possible while still being able to produce enough flux of Eu atoms because a large heat load on the cell obstruct efficient loading of the atoms. Also, the lower the power, the slower the coating of the mirror with layer of Eu atoms. Eu atoms that are released by the ablation pulse thermalize with the cold buffer gas and are loaded into the trap. Buffer gas is then pulled away by lowering the cell temperature leaving a trapped sample of atoms which eventually escape slowly. We take scans of data or record the decay of absorption signal at fixed frequency. Detailed description of procedure and data are given in Chapter 6.1.2, and 6.2.

Chapter 6

Results and Data Analysis

In this chapter, results of the experiment and the data analysis are presented. Data was taken in one of two ways: either absorption time profiles at a fixed wavelengths or the laser was scanned over the entire absorption band of about 14 GHz at certain fixed delay times after the ablation pulse. The first method provided information on the loss dynamics of the trapped atoms while the second method provided the spectral evolution of the trapped atoms, the number density and temperature.

6.1 Spectra

This section presents spectra of trapped and untrapped Eu. Experimental and theoretical spectra are compared.

6.1.1 Thermalization

We investigated thermalization of laser ablated Eu as a function of the buffer gas temperature. The cell (filled with ~1 Torr of ^{3}He gas) was cooled down from the room temperature to 4 K. An Eu absorption spectrum was taken at 300 K, and 77 K employing the pulse-and-sweep (see Chapter 5.2.3). (The temperature was monitored by the diode thermometer.) We scanned over one of the hyperfine lines in the red $z^{10}P_{7/2} - a^8S_{7/2}$

band (4 μs natural lifetime, λ= 710.8 nm). The natural linewidth of this transition is less than 0.1 MHz. The width due to Doppler broadening is estimated to be between 24-423 MHz for T =1 K-300 K. (See eqn. 4.1) A simple calculation predicts the collisional broadening (γ) due to 1 torr of ^{3}He buffer gas to be about 1-17 MHz for T = 1-300 K (Note: $\gamma = 2nv\sigma$ [91] where n is the density of the buffer gas, v is the mean velocity of atoms, and σ is the cross section for phase randomizing collisions.) For T = 1-300 K, the Doppler broadening is much greater than either the natural linewidth or the pressure broadening. Therefore, it should be possible to infer the temperature of the Eu vapor directly from the width of the line. Figure 6.1 shows the lineshape at 300 K and 77 K. The linewidths of 500±30 MHz, and 275±30 MHz correspond to temperatures of 400±50 K, and 125±30 K respectively. From this data, we concluded that the ablated plume had thermalized with the buffer gas.

6.1.2 Spectra of Trapped Atoms

Figure 6.2 shows sample spectra of the trapped ensemble measured in a time period between 0-20, 0-40, 0-60 sec after the ablation pulse. This sample was loaded into a 0.52 T deep trap with the cell at 250 mK. One can see that the main features of the spectra change little with time but their integrated absorption intensities are decreasing.

The trap spectra were assigned on the basis of the spectral constants of ^{151,153}Eu given in Table 3.2 [63] and the distribution function of the number of atoms in the beam path subject to a given magnetic field, $N(H)$. $N(H)$ was determined for a given magnetic state, M_J, the loading temperature, the calculated spatial distribution of the magnetic field (Biot-Savart integration of the known currents), and from factors accounting for the probe beam geometry such as the beam diameter, the offset from the center and the polarization direction of the probe laser. The density was assumed to have a Boltzman distribution, $e^{\frac{-<\mu>H(r)}{kT}}$. At our loading temperature, the splitting between different M_I's is less than 2 mK. Therefore, as an initial assumption, an equal weight

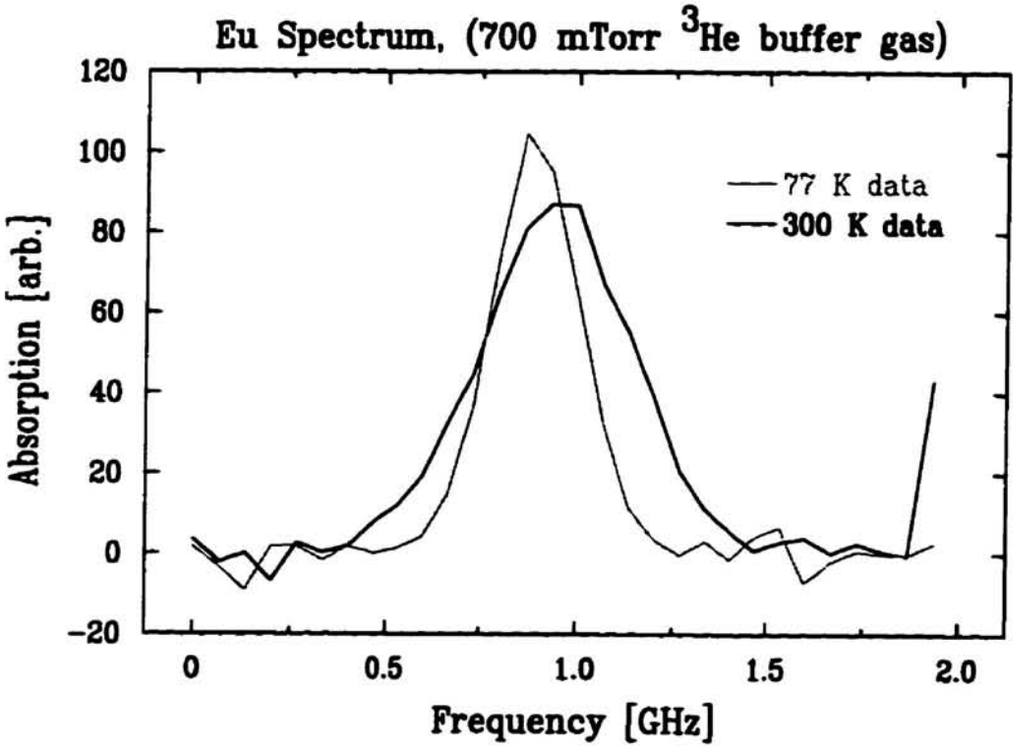

Figure 6.1: Eu ablation spectra (around 14068.17 cm^{-1} with 700 mTorr of ^{3}He buffer gas) taken at 300 K and 77 K. The linewidth becomes narrower with decrease in temperature as expected.

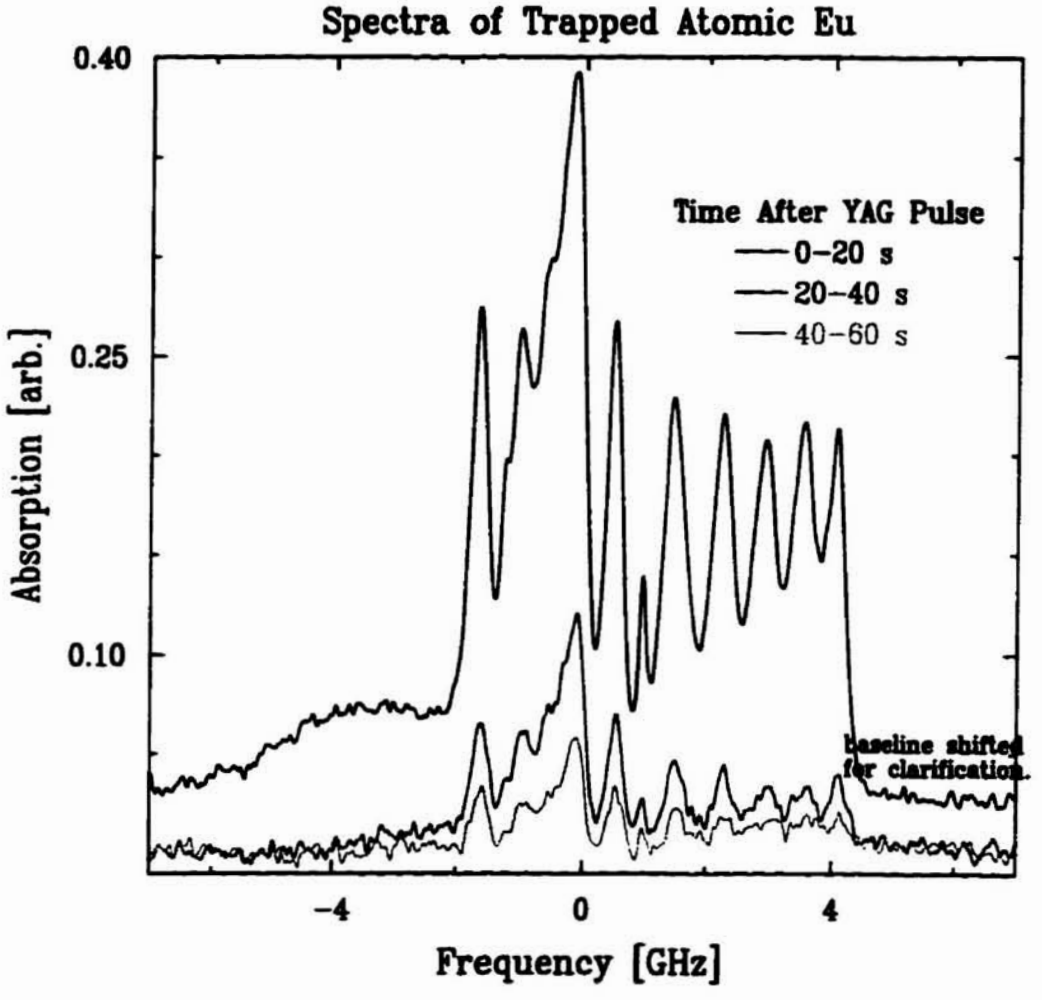

Figure 6.2: Sample absorption spectra of the trapped ensemble of Eu in a 0.6 T deep trap at 462.7 nm measured at 20 s, 40 s, and 60 s after the ablation pulse.

was assigned to each hyperfine state. This was corroborated by our measurements.

The spectra of the trapped atoms were simulated by summing up computed spectra pertaining to all field strengths (H) and weighting each by the corresponding factor $N(H)$. This is valid in our density regime which lies in the low optical density regime. The spectrum for a given H was calculated by summing all allowed electric dipole transitions (weighted by S_q, the linestrength factor given below) of a given M_J state for each isotope. The natural abundance of each isotope (48% for ^{153}Eu and 52% for ^{153}Eu) was also taken into account by a factor f_i. All hyperfine states M_I (-5/2 to 5/2) were weighted equally, as mentioned above. Each transition was given a Lorentzian line shape, $L(\nu - \nu_{res})$, with the linewidth given by the sum of the natural linewidth (26 MHz for lifetime of 6 ns [92]) and the Doppler width (14 MHz at 250 mK).

However, the observed spectrum is insensitive to these widths because magnetic broadening is much larger (~270 MHz). This determination of $A(\nu)$ can be summarized by

$$A(\nu) \propto \sum_{H=0}^{H_{max}} \sum_{i=151}^{153} \sum_{M_J'=-\frac{7}{2}}^{\frac{7}{2}} \sum_{M_I=-\frac{5}{2}}^{\frac{5}{2}} \sum_{M_I'=-\frac{5}{2}}^{\frac{5}{2}} L(\nu - \nu_{res}) N(H) f_i S(M_J', M_I'; M_J, M_I) \tag{6.1}$$

where

$$L(\nu - \nu_{res}) \propto \frac{\delta\nu}{(\nu - \nu_{res})^2 + \frac{\delta\nu^2}{4}} \tag{6.2}$$

$$\nu_{res} = \frac{1}{h} E(M_J', M_I') - E(M_J, M_I) \tag{6.3}$$

$E(M_J, M_I)$ is calculated from eqn. 3.18. $E(M_J, M_I)$ was used for all $N(H)$ instead of $E(F, M)$ because at $H_{max} = 0.6$ T, more than 90% of the detected trapped atoms are subject to $B > 0.05$ T where the strong-field limit is reached. $S(M_J', M_I'; M_J, M_I)$ is the line strength factor of electric dipole transition between states $|M_J', M_I' > \leftarrow |M_J, M_I >$. It takes into account the distribution of the orientation of the atoms. The details of this formula are given in Chapter3.3.3. (See eqn. 3.42)

$$S(M_J', M_I'; M_J, M_I) \propto \sum_{q=-1}^{q=+1} F_q S_q(M_J', M_I'; M_J, M_I) \tag{6.4}$$

where $q = 0$ for parallel and $q = \pm 1$ for perpendicular transitions. F_q represents fraction of $N(H)$ that will have $\delta M = q$ transition and it depends on the direction of the laser polarization with respect to the orientation of the atoms. (See eqn. 3.38)

The spectrum was simulated for different M_J's. The result clearly indicated that the trapped atoms correspond to M_J=7/2 state. This is consistent with our model of loading: the lower M_J states are not as tightly confined and leave the trap quickly. The spectrum for M_J=5/2 was also simulated and was added to the M_J=7/2 with different weights in order to determine if the spectrum can be simulated equally well with both states present. We found that the simulated spectrum started to deviate from the actual spectrum if more than 10% atom fraction of M_J=5/2 is included.

Because we were not equipped to image the trapped atom cloud directly, and careful measurements of the beam diameter and offset were not taken, the final determination of the parameters had to be inferred from the spectrum data. In the simulation, it was found that as the offset is increased, the location of the $\Delta M = -1$ peak shifts lower in frequency space with respect to $\Delta M = 0$ peaks. At zero offset, much of $\Delta M = -1$ peak of ^{153}Eu overlaps with the $\Delta M = 0$ peaks and is indistinguishable. At higher off-set, however, the peak is more visible due to wider separation. Our best fit indicated the beam offset of 5 ± 1 mm.

The width of the $\Delta M = -1$ peak gave us information on the beam diameter. The best fit was obtained for a beam diameter of 5 mm assuming the temperature of the cell to be 250 mK. Our knowledge of the beam size before it entered the cell and the geometrical consideration of the beam path, limited the beam diameter to 3.5 ± 1.5 mm and the offset to 3 ± 1.5 mm. Our estimate of the beam diameter and the offset from the simulation based fits are consistent with this limit.

In the simulation, the probe beam was assumed to travel vertically and thus have

only one offset value. This was done for ease of calculation. However, in the real experiment, the beam hits the retro-reflecting mirror at a small angle from 90° in order to separate the input and exit beam. Therefore, the location of the entering beam and the exiting beam are different in the trap region. A rudimentary effort was made to improve the spectrum by mixing the simulated spectra with two different offsets but this did not improve the simulation.

Also unknown was the direction of the beam polarization with respect to the direction of of the offset in the x-y plane (where z is the axis of the beam propagation and the axis of symmetry for the trap). We discovered that the ratio of the $\Delta M = -1$ and $\Delta M = 0$ transition in our simulation was determined by the direction of the offset with respect to the direction of laser polarization. This gave us information about the direction of the laser polarization with respect to the offset. The angle between the offset and the polarization is $45 \pm 5°$.

Figure 6.3 shows the assignment of the lines according to the isotope and hyperfine substates. It is clear from the theoretical fit to the spectrum that all of the hyperfine states of Eu are trapped and that all of the hyperfine states persist throughout the trap lifetime. (See Figure 3.5 for the correlation diagram.) However, their relative intensities change disproportionately with time. We believe this may be due to spin exchange processes. However, it may also be that different hyperfine states have different dipolar relaxation rates. Figure 6.4 shows the individual spectrum after 20 s, 40 s, 60 s separately. It can be clearly observed the states other than $M_I = 5/2$ state go away faster.

The linewidth of the hyperfine lines are due to magnetic broadening. The temperature of the trapped atoms can be inferred from the magnetically broadened hyperfine line. At 250 mK and 15 A, the number of atoms vs. the magnetic field strength is shown in Figure 6.5 for our best estimate of the beam geometry. The FWHM of this graph (ΔH) is $\sim$ .085 T. For $\Delta M = 0$ transitions, the width is due to the difference in

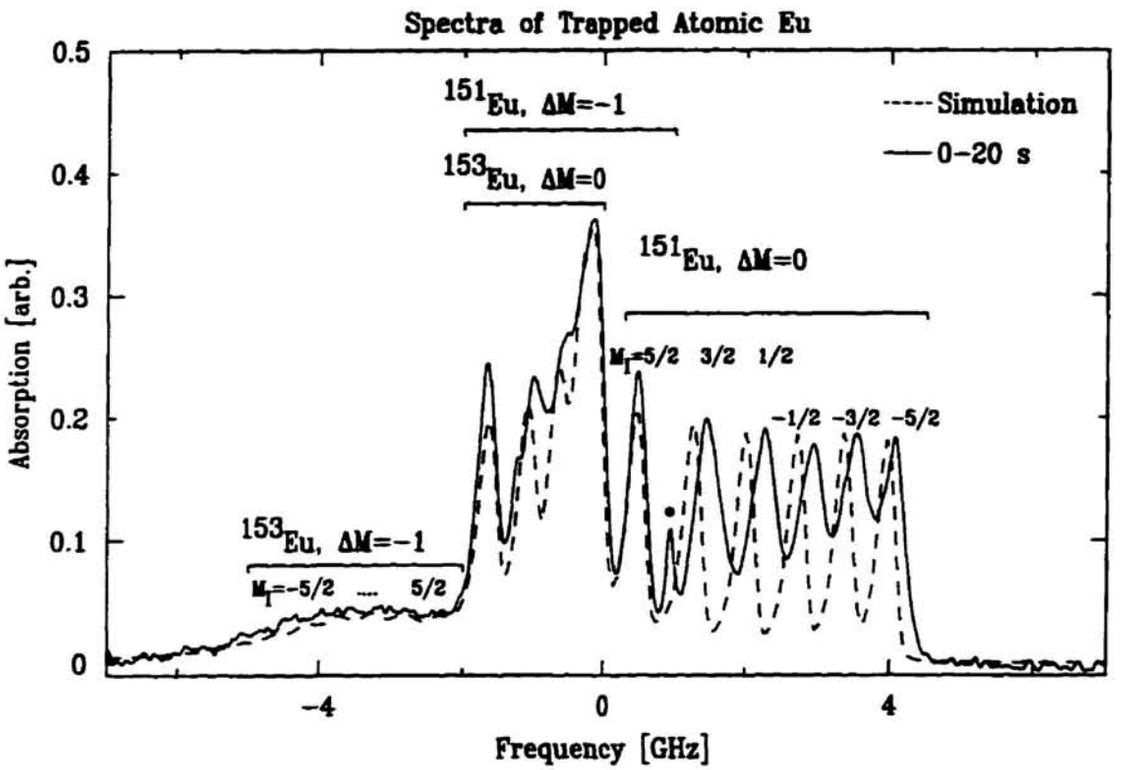

Figure 6.3: Simulated spectrum and the assignment of the hyperfine lines. All features are due to the $M_J = 7/2$ state of Eu($^8S_{7/2}$). For each isotope, there are two sub-bands of magnetic hyperfine transitions, with $\Delta M_J = 0$ and -1. The location of the $\Delta M_J = 1$ sub-bands shifts to the left (i.e to the red) with respect to $\Delta M_J = 0$ bands as the beam offset from the center of the trap is increased. Note that for the $\Delta M_J = 0$ transitions in ^{151}Eu, all six M_I nuclear spin states are clearly resolved.

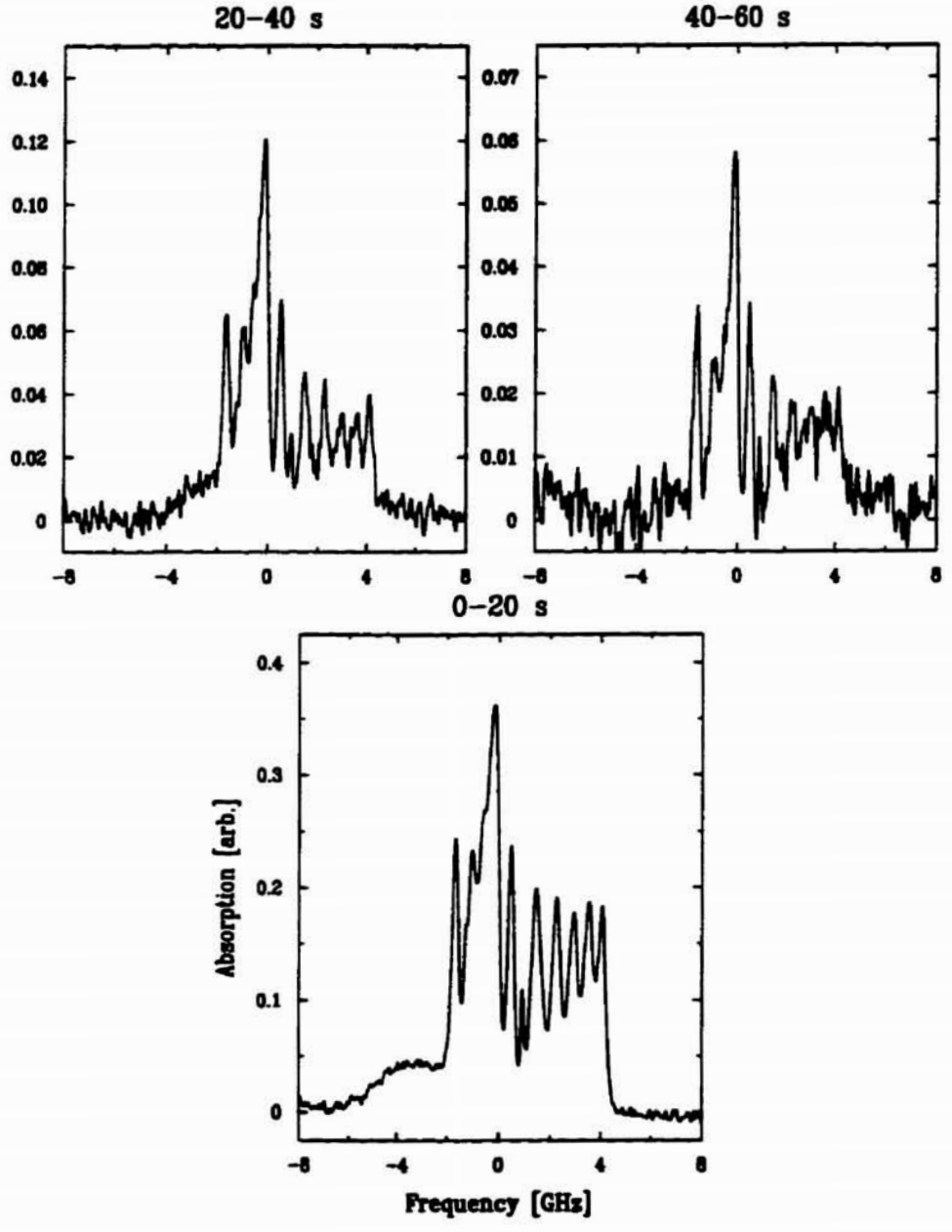

Figure 6.4: Figure 6.2 drawn separately for each delay time. Note that the $M_I = 5/2$ states have narrower linewidth than other states and decays more slowly than other M_I states.

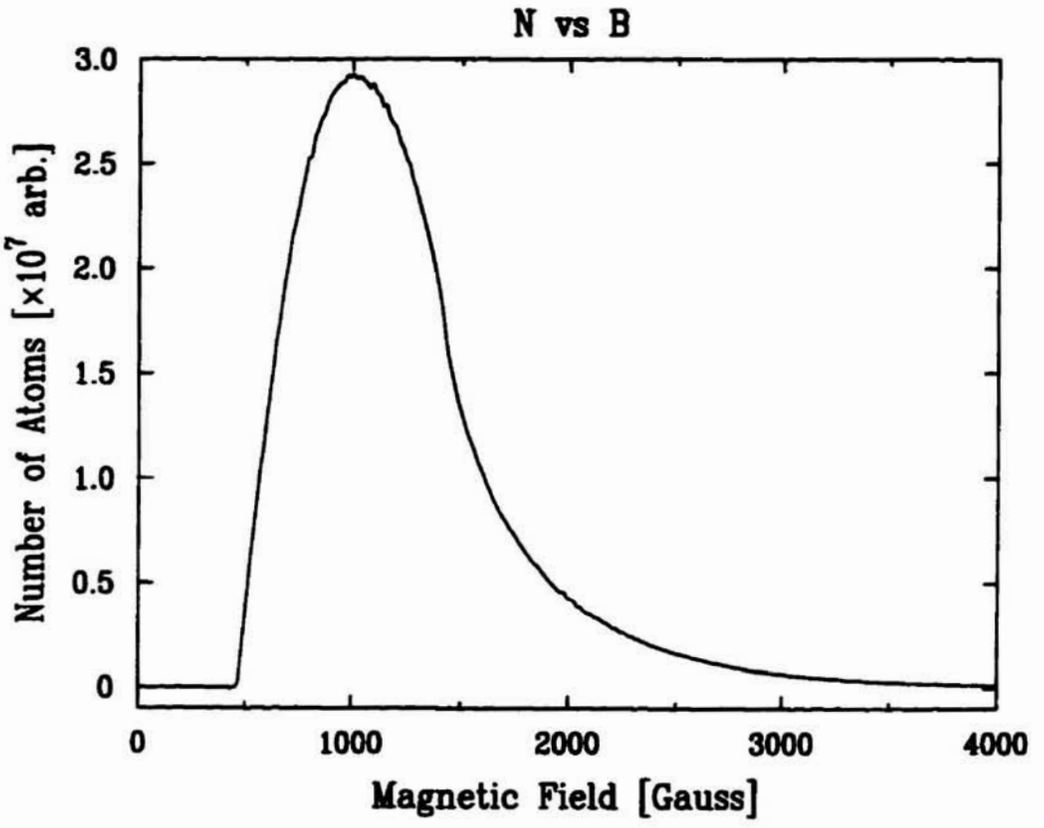

Figure 6.5: Calculation of atom number vs. magnetic field strength for a beam of 0.5 cm dia. with 0.5 cm offset at T= 250 mK. The trap is 0.52 T deep.

the ground state and the excited state g-factors, g_g and g_e respectively. It is given by

$$\delta\nu = \frac{1}{h}(g_e - g_g)M_J\mu_B\Delta H \tag{6.5}$$

$\approx$ 250 MHz.(Figure 6.3) The observed linewidth of $\Delta M_J = 0, M_I = 5/2$ hyperfine lines are 270 ± 10 MHz. Given the uncertainty of our beam geometry, the predicted and observed linewidths are rather in good agreement. The reason that the observed linewidth is greater is probably due to the fact that during the first 20 s after the ablation, the temperature of the cell is slightly higher than 250 mK. The maximum possible measured $\delta\nu = 280$ MHz would indicate a temperature of 400 K.

Figure 6.6 shows a 100 mK, 200 mK, 300 mK, and 400 mK fit to the data. These fits were made using our best estimate of the beam geometry. More accurate temperature information, which would be vital for studying evaporative cooling, could be gained by better control of the beam geometry.

The transition has a natural linewidth of 25 MHz, corresponding to a temperature of 10 mK. This transition can therefore not be used to measure the temperature of atoms much colder than 30 mK. However, many narrower transitions exist and these could, in the future, be used to measure lower temperatures.

Procedure for Taking Spectra of the Trapped Sample

Trapping is ideal for high-resolution spectroscopy. The atoms can be probed for a long time, and can be held at a temperature far below their freezing point, leading to narrow transitions.

To take our spectrum, first the magnet is energized to a desired value (typically 15 Amps, $H_{max} = 0.52$ Tesla). The laser is scanned 14 GHz (7 GHz before doubling) at 1-10 scans/sec. The YAG laser fires a pulse creating a pulse of atoms. The absorption spectra of the atoms in the trap region are integrated for about 20 scans. The data are monitored and recorded. (See Chapter 5.2.3 for details.) The spectrum shown in Figure 6.2 represents an average of 19 trap loads, integrating for 20 seconds per load.

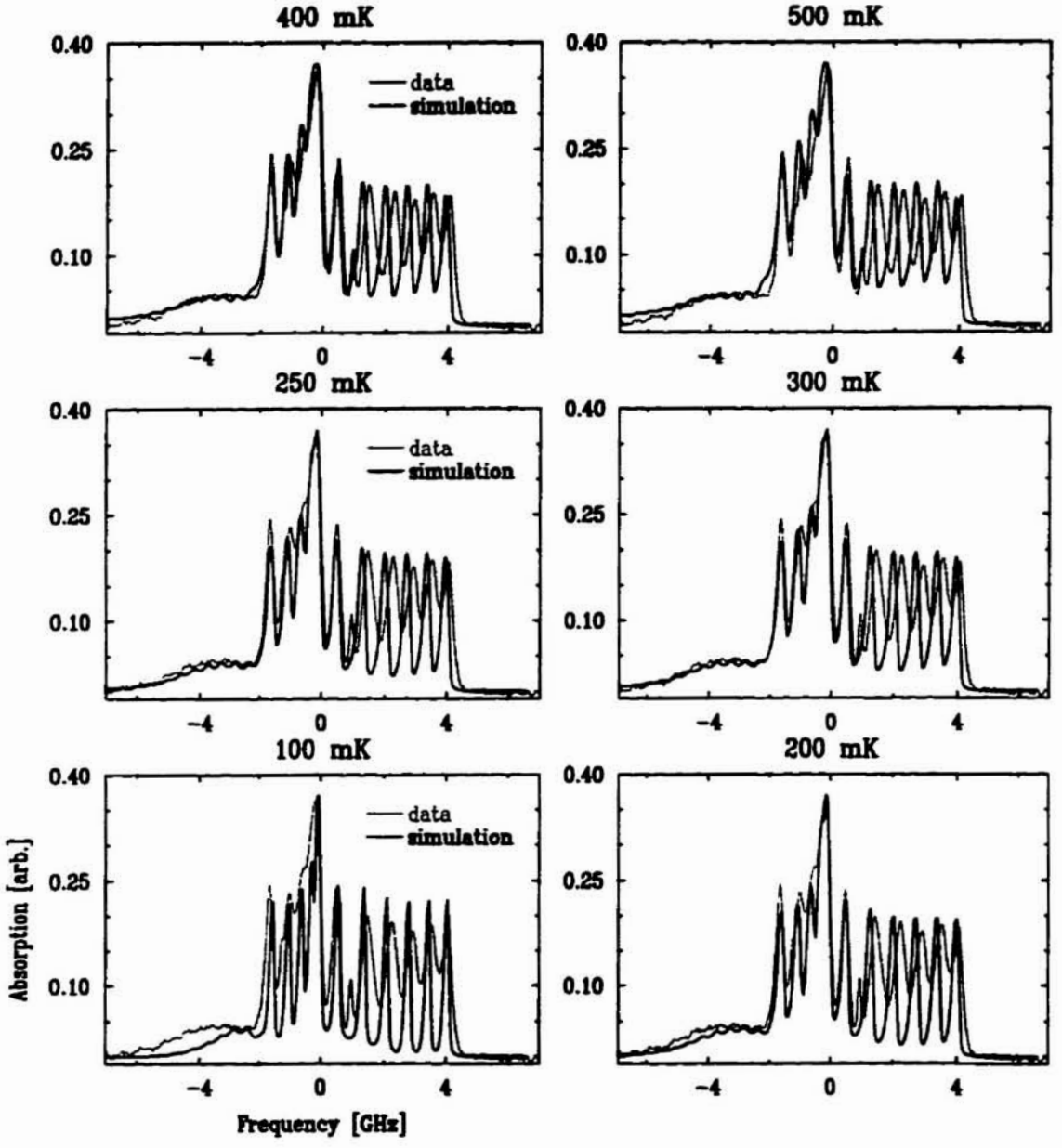

Figure 6.6: Eu spectrum simulation at various temperatures for our best beam geometry. The best simulation is for T = 250 mK and 300 mK.

Special Features of the Spectrum

Although almost all the features of the trap spectrum have been reproduced in our simulation, one peak (marked by • in Figure 6.3) is not reproduced. Efforts to reproduce this peak using 2 different beam offsets for the entering and exiting beam and also including lower M_J states were made but were unsuccessful. The peak was extremely repeatable, and persisted for the entire lifetime of the trapped sample, which makes it seem unlikely that it was a laser glitch or other artifact. Also unexplained is the difference in the linewidth between the simulated hyperfine lines and the actual data. Except for $M_I = 5/2$ lines, the width of other hyperfine lines of the actual spectrum were much greater than the simulated spectrum. It is not clear why the hyperfine lines have different linewidths.

The beam geometry was not as well controlled as it should be. Although the beam position and polarization relative to the trap can be extracted from the spectrum, more information could be learned from the spectrum if this geometry was better quantified. Unfortunately, we did not successfully simulate the spectrum until after the trapping run was complete, so the dependence of the spectrum on beam position was not verified.

We attempted to image the atom cloud onto a CCD camera, but our camera system was rather unsophisticated and we were not successful. A more elaborate imaging system is being developed for future experiments.

Optical Pumping

It was found that by raising the probe beam power to $\approx$10 μWatt, we could optically pump the atoms out of the trap. Figure 6.7 shows the absorption vs. time for a number of different beam powers. For this run, we were primarily interested in avoiding optical pumping, so we limited our power to 10 times lower than the lowest power where optical pumping was observed. One might be able to use this to evaporatively cool the sample by tuning the beam to eject those atoms residing in high magnetic fields (and therefore

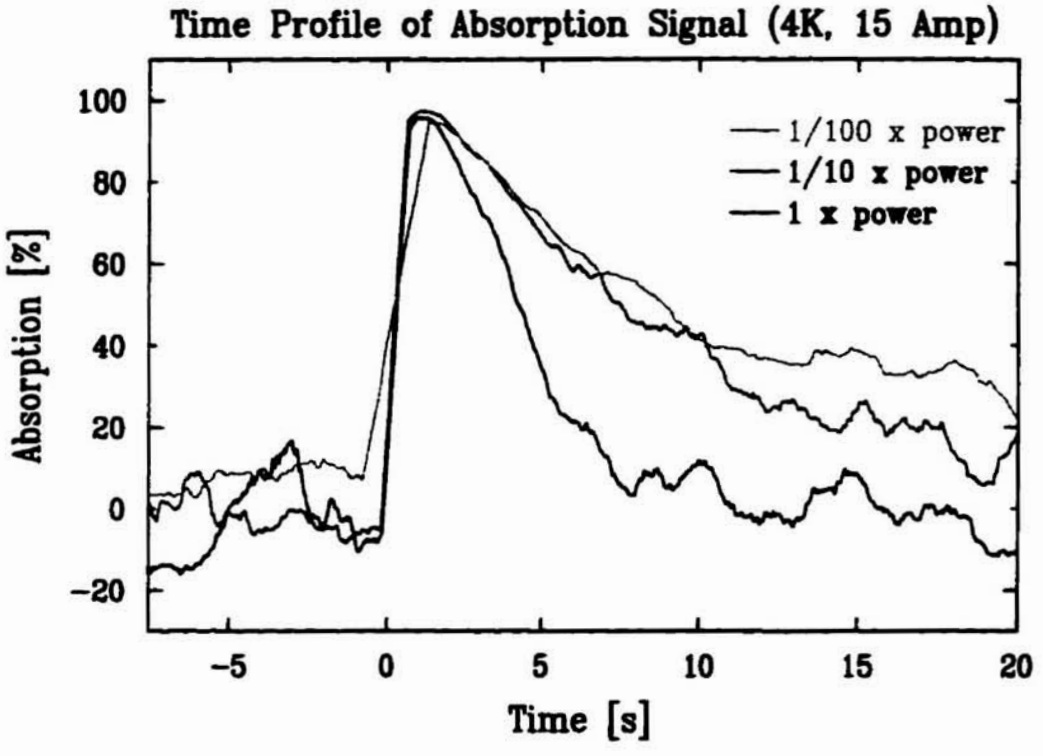

Figure 6.7: Evidence of optical pumping is shown above. When the laser probe beam power is lowered by factor 10 and 100 from the initial power, the number of atoms after a fixed delay is higher.

high energies). This is analogous to the rf-knife [35], potentially allowing separate control of the trap depth and field gradient.

6.2 Time Profile

6.2.1 Incipient Trapping

We investigated lengthening of the sample lifetime ($\sim$ 1 s) by looking at the time profile of absorption signal at various magnetic fields. The magnet current was ramped up to a desired value slowly so that the cell temperature did not rise high enough to shut down the fridge. The cell temperature was kept at 250 mK except when the Eu was ablated which caused the temperature of the cell to rise for a short time. After an ablation pulse, the temperature equilibrated back to 250 mK within 20 sec. The absorption signal was monitored at the wavelength of 462.7 nm which is in the blue $z^{10}P_{7/2} - a^8S_{7/2}$ band (6 ns lifetime [92]).

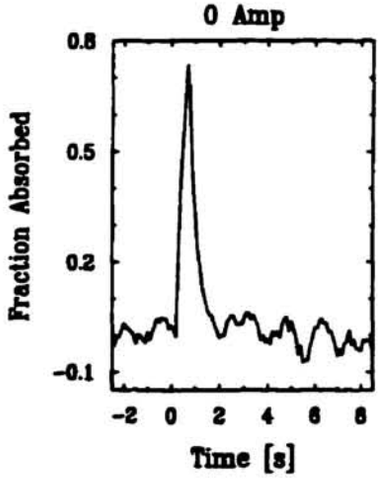

(Continued on the next page.)

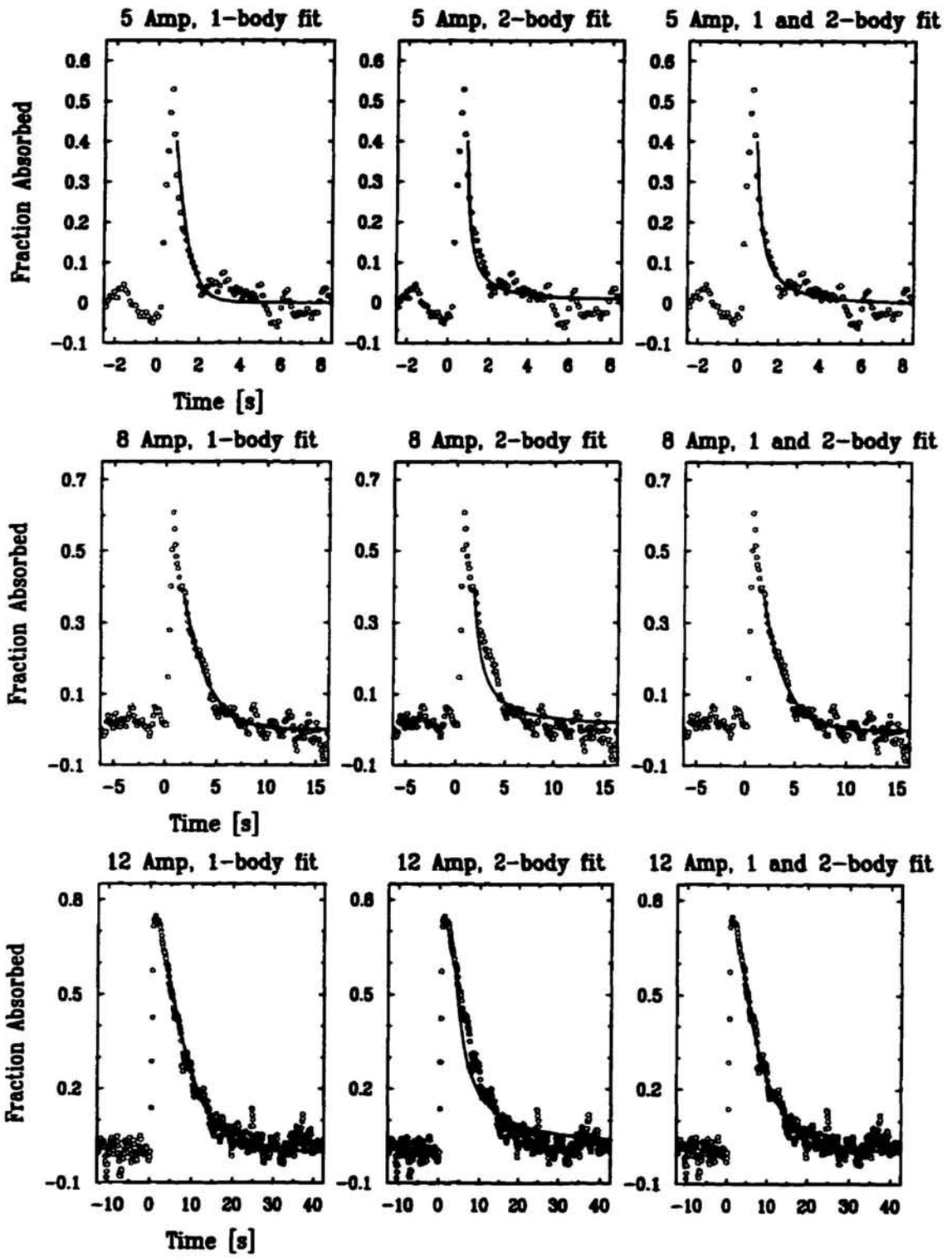

(Continued on the next page.)

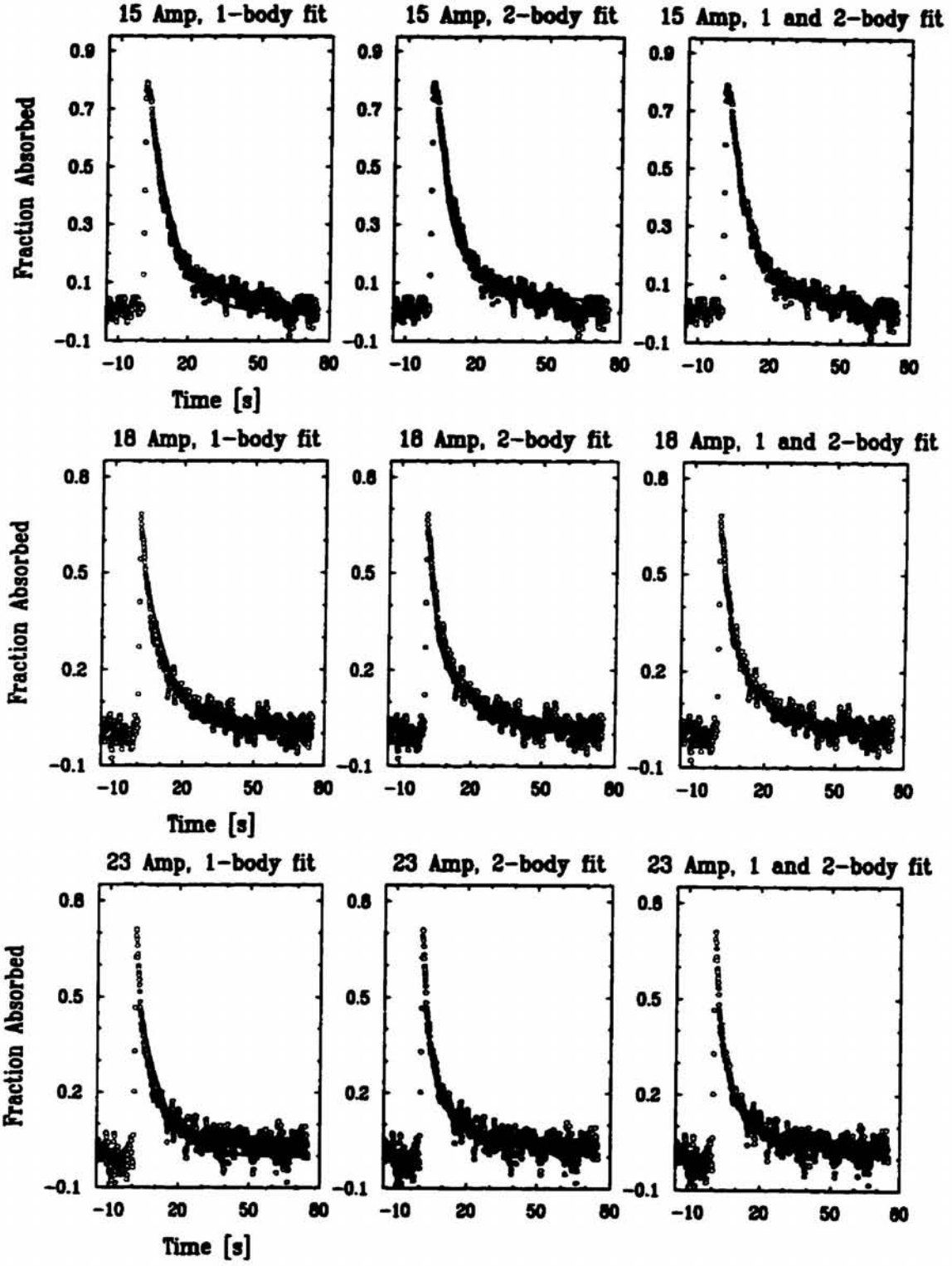

(Continued on the next page.)

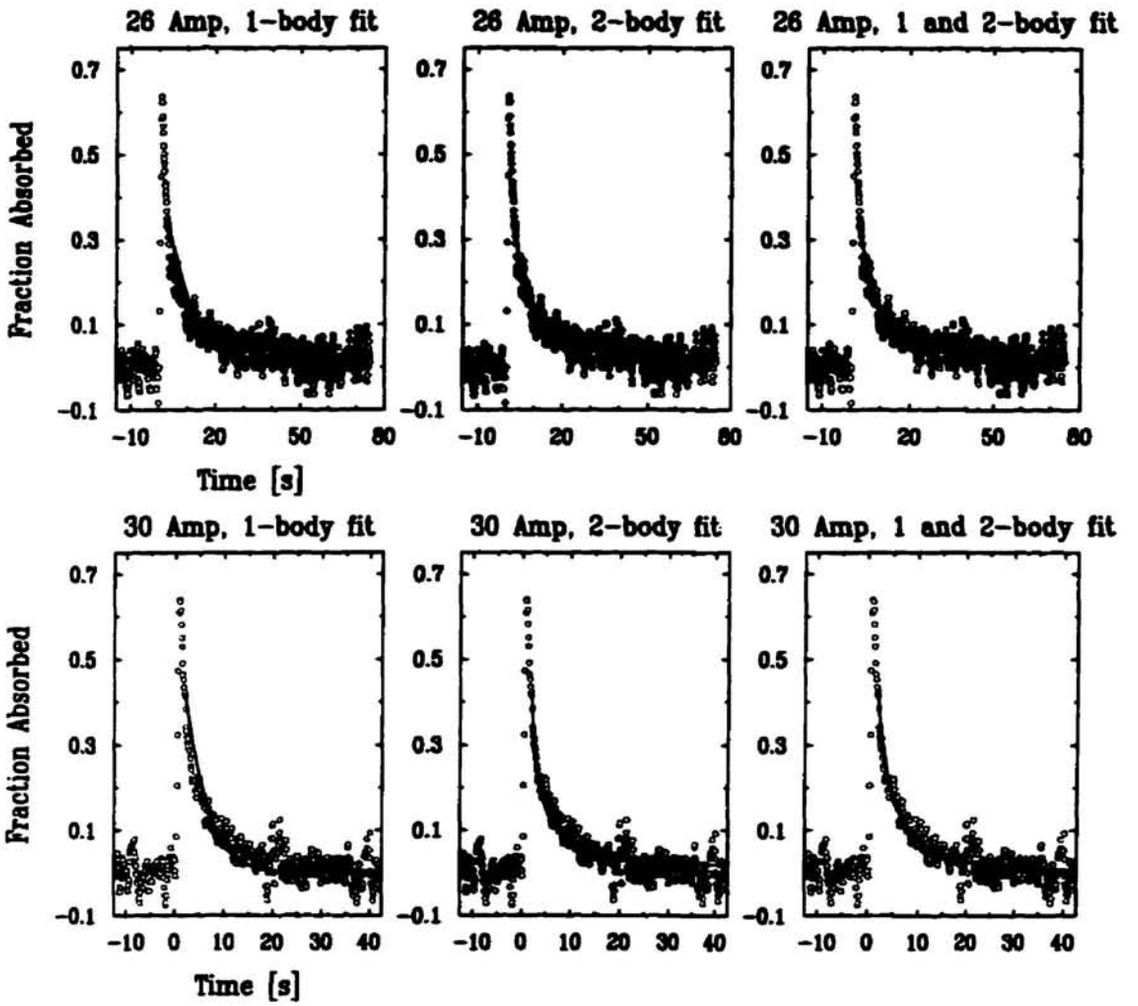

Figure 6.8: Absorption time profile at various magnetic fields, 0-30 Amps (0-1.04 Tesla). The frequency of the probe laser was the same for each time profiles. The atoms were loaded at 250 mK. However, due to the ablation pulse the temperature rises above 250 mK then falls back to 250 mK. Except for 0 Amp, 1-body, 2-body and a combination of 1 and 2-body fits are given for each time profile data. Note that at low magnetic field strength 1-body fits are better but at high field strength 2-body fits approximate the decay better. The data shown in the figure was smoothed over 4 bins.

Figure 6.8 shows the absorption time profile at various magnetic fields. According to the figure, the longest trap lifetime occurs at 15 Amps (0.52 Tesla). At this field strength, η of our trap is 9.5 for $M_j = 7/2$. η is the ratio of the trap depth to the thermal energy, given by

$$\eta \equiv < \mu > H_{max}/kT = gM_j\mu_B H_{max}/kT \tag{6.6}$$

where $< \mu >$ is the magnetic moment and g is the gyromagnetic ratio. Initially the lifetime of the signal increases with the increase in the field . Above 20 Amp, (0.7 Tesla, eta = 12.7) however, the signal decays faster as the field is further increased. This is most likely due to the increase in density at the center of the trap at higher fields which in turn causes the 2-body decay term to increase.

The loss mechanisms of atoms from the trap region can be classified into 1-body ($\propto$ to n, where n is the local density), 2-body ($\propto$ to n^2) and, 3-body ($\propto$ to n^3) loss terms corresponding to decay curves of $e^{-t}, 1/t, 1/t^2$ respectively where t is the time.

For a fixed atom number, 2 and 3 body losses would be accelerated in more tightly confining traps (higher currents in our configuration). This is because the atom cloud is concentrated in the center of the trap, resulting in a higher density for the same number of atoms.

At low fields, the dominant 1-body loss mechanism is atoms leaving over the edge of the trap and sticking to the walls. In the absence of diffusion, which could slow this loss but not accelerate it, the loss rate would scale as $e^{-\mu B/kT}$ and be strongly suppressed at high fields. (See Chapter 6.2.4.) Other 1-body loss mechanisms, such as Majorana transitions at the trap center, could remain significant at higher fields, but are expected to provide a trap lifetime on the order of 1000 sec (see Chapter6.2.4). We therefore expect 1-body losses to dominate at low fields, and 2 or higher order processes to dominate at higher fields.

Figure 6.8 illustrates time profiles for a selection of different trap depths. Each load was done at 250 mK (the equilibrium temperature in the absence of heating due to the

Current	fit	$a(s^{-1})$	$b(cm^3s^{-1})$	Current	fit	$a(s^{-1})$	$b(cm^3s^{-1})$
0 Amp	1-body	1	-	-	-	-	-
5 Amp	1-body	2	0	8 Amp	1-body	0.51	0
	2-body	0	2.8×10^{-10}		2-body	0	3.1×10^{-11}
	1&2-body	0.411	1.6×10^{-10}		1&2-body	0.51	7.6×10^{-13}
12 Amp	1-body	0.20	0	15 Amp	1-body	0.10	0
	2-body	0	2.7×10^{-12}		2-body	0	8.5×10^{-13}
	1&2-body	0.13	6.9×10^{-13}		1&2-body	0.041	4.5×10^{-13}
18 Amp	1-body	0.11	0	23 Amp	1-body	0.12	0
	2-body	0	6.9×10^{-13}		2-body	0	4.1×10^{-13}
	1&2-body	0.033	4.1×10^{-13}		1&2-body	0.011	3.3×10^{-13}
26 Amp	1-body	0.13	0	30 Amp	1-body	0.27	0
	2-body	0	4.1×10^{-13}		2-body	0	4.5×10^{-13}
	1&2-body	0.0083	3.7×10^{-13}		1&2-body	0.076	2.6×10^{-13}

Table 6.1: 1 and 2-body rate coefficients from fitting the absorption time profiles at various magnetic field strength. (See Figure 6.8.) The rate coefficients a and b correspond to the constants in $\dot{n} = -an - bn^2$. The temperature was assumed to be 250 mK at all time. It was also assumed that the line strength stays the same with the change in magnetic field. (The line strength factor at 15 A was used for fitting the data.)

ablation laser), pulse energy of ~10 mJ and the probe laser fixed at 28,136.26 cm^{-1}. Each plot shows the observed time profile, the best-fit time profile for a combination of 1 and 2 body losses, and the 1 and 2 body components of this loss shown separately. Each fit was determined by adjusting a parameter (in case of 1-body or 2-body fit) or parameters (in case of 1 & 2-body fit) until it produced the least mean square difference between the fit and the data. The time profile at 0 field is included for comparison, but losses in this case are qualitatively different (consistent with diffusion through the ^3He gas), so no curve fits are provided.

Table 6.1 shows the 1 and 2 body rate coefficients at various magnetic field strength. The conversion factor between the current in the coils and the maximum $|\vec{H}|$ is 345 Gauss/Amp. The rate coefficients are given from 1-body and 2-body fits separately and from the combination of 1 and 2-body fit. The two body term, $\frac{\dot{n}}{n^2}$, has been corrected for the changing overlap of the atom cloud and the beam at higher fields. It is, however, a rough estimate because the exact position of the beam and the detailed spectrum were not recorded. (Note: the 1-body term is independent of the density.) This information was recorded for the data taken at 15 Amps, leading to an estimated 2-body loss cross section of $4.5 \pm 2.7 \times 10^{-13}\text{cm}^3\text{s}^{-1}$ (see Chapter 6.2.2). For other data sets, the same line strength at 15 Amp was assumed in calculating the rate coefficients. (In order to measure the rate coefficients accurately, the actual line strength, taken from the spectrum at each current value, should be used.) Also, the temperature of the cell rises immediately after ablation to about 1 K and then falls back to to 250 mK in about 20 s. This prohibits a strict interpretation of the results of the fit that includes data for which $t < 20$ s. In spite of these uncertainties, the dominance of 1-body losses at low fields and 2-body losses at higher fields can be clearly seen. This was also confirmed by comparing the mean square differences of each fit. The mean square difference of 1 & 2-body fit (with two adjustable parameters) was always smaller than that of either 1-body fit or 2-body fit which have only one adjustable parameter. At low magnetic fields (< 15 A), the mean square difference of 1-body fit was smaller than that of 2-body fit (and closer to that of 1 & 2-body fit). At high magnetic fields (> 15 A), the mean square difference of 2-body fit was smaller than that of 1-body fit. Figure 6.9 shows our data taken at 23 amps with a 1-body, 2-body, and 3-body fit for $t > 20$ s. 1-body losses are clearly a poor fit, but we have no data which clearly indicates a 2-body rather than 3-or-more body loss mechanism. 2-body losses have been assumed since the rate coefficient for 3-body loss is more than 10000 times higher than that of alkali atoms ($\sim 10^{-28}\text{cm}^6\text{s}^{-1}$ for sodium atom[93]) (and therefore seemed unreasonable).

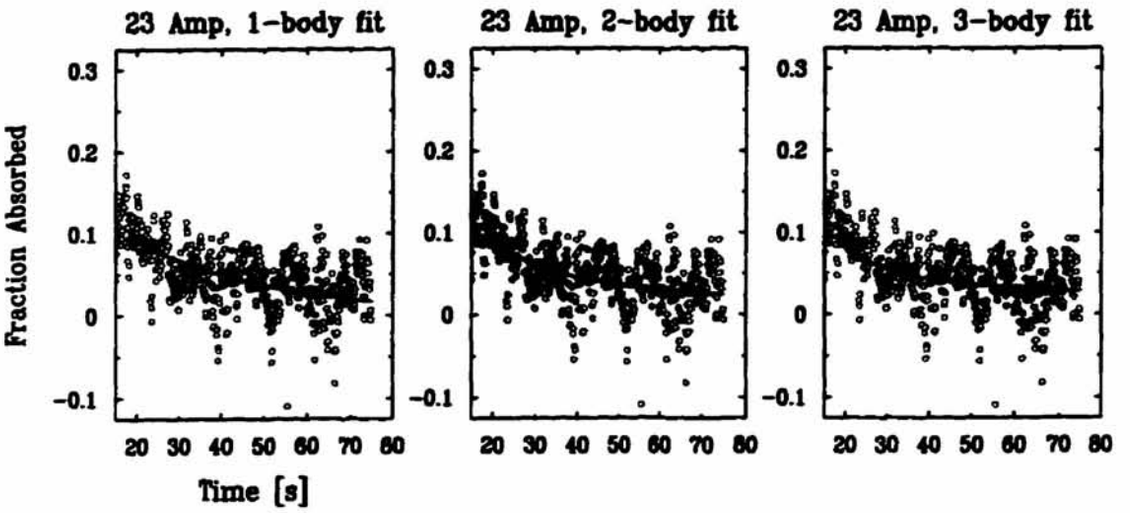

Figure 6.9: 1-body, 2-body, and 3-body fits of the absorption time profile at 23 Amp (0.8 Tesla) and 250 mK. The rate coefficients for 1-body, 2-body, and 3-body decays are 0.032 s^{-1}, $4.5 \times 10^{-13} cm^3 s^{-1}$ and $3.0 \times 10^{-24} cm^6 s^{-1}$ respectively. The mean square differences for 1-body, 2-body, and 3-body were 0.005969, 0.005919 and 0.005914 respectively.

6.2.2 Eu Density Calculation

The density of the Eu atoms was extracted from absorption as follows. In order to calculate the density, first we have to determine the absorption cross section at our laser frequency for a given experimental condition. The absorption cross section is given by

$$\sigma(\nu) = \frac{h\nu}{c} B\mathcal{S}(\nu) \tag{6.7}$$

(See Chapter 3.3.3.) where B is the Einstein B-coefficient and $\mathcal{S}(\nu)$ is the normalized linestrength factor (i.e. $\int S(\nu)d\nu = 1$). For typical experimental conditions for the time profile measurement (250 mK, 15 A) σ is about $1.78\times10^{-12}\text{cm}^2$. If the optical density is low, $\mathcal{S}(\nu)$ is simply given by the absorptance at ν divided by the area under the spectrum. With the determined absorption cross section, a computer program calculates the absorption according to the following formula,

$$\mathcal{A}(\nu) = 1 - \frac{\sum_{x_{beam}} \sum_{y_{beam}} dxdy\ e^{-2\sigma(\nu)\int_{z_{min}}^{z_{max}} n(x,y,z)\ dz}}{\sum_{x_{beam}} \sum_{y_{beam}} dx\ dy} \tag{6.8}$$

$$n(x,y,z) = n_0 e^{\frac{-<\mu>H(r)}{kT}} \tag{6.9}$$

where the z-axis is along the direction of beam propagation. (Note: the factor of 2 is due to the fact that the beam passes through the cell twice.) The summation is over the area of the beam diameter(in x-y plane). For a given temperature T, beam geometry and the magnet current, the code calculates the absorptance at several different values of n_0. Eqn. 6.8 was approximated by a 5th order polynomial relating $n_0$to$\mathcal{A}(\nu)$ and $\mathcal{A}(\nu)$ton_0 The conversion from the absorption to the density at the center of the trap is made using this function which approximates n_0 to $\mathcal{A}(\nu)$.

One source of error with this method is that it does not take into consideration the temperature variation that takes place in the cell over approximately the first 20 seconds. The temperature affects the spatial distribution of the cloud, changing both the spectrum and the overlap of the probe beam with the trapped atoms.

n_0 was calculated using this method for the time profiles of absorption vs. time. The total number of atoms in the trap is given by

$$N = n_0 V \tag{6.10}$$

$$V = \int e^{\frac{-<\mu>H(\vec{r})}{kT}} d^3\vec{r} \tag{6.11}$$

where V is the "effective volume" of the trap. For a linearly varying potential as ours, V is

$$V = V_0 \eta^{-3} \tag{6.12}$$

where $\eta = <\mu> H_{max}/kT$. For our trap geometry, V_0 is calculated to be 245 cm^3. For our typical trapping condition (15 A, 250 mK) and beam geometry (5 mm beam dia. and5 mm offset), the relationship between N_{tot}, the total number of atoms in the trap, and n_0 and between N_{beam}, the number of atoms in the beam path, and n_0 are given by

$$N_{tot} = 0.28 n_0 \tag{6.13}$$

$$N_{beam} = 0.02 n_0 \tag{6.14}$$

where n_0 is given in cm^{-3}.

6.2.3 Trapped Eu with ^{3} Buffer Gas

The procedure for trapping Eu is as follows: The trapping current is set at 15 Amps (0.52 Tesla trap depth). (See the previous section 6.2.1.) The cell temperature is raised to 250 mK. A single YAG pulse ablates the Eu atoms and the heater on the cell is turned off immediately following the ablation pulse.

It was observed that the temperature of the cell rose quickly for 1 sec and dropped over the next 20 sec to 170 mK. 170 mK was the lowest temperature the cell could reach when the experiment was performed. The probe laser frequency was fixed at frequency

which yielded the highest absorption and the time profile of the absorption signal was monitored with a scope.

From Figure 6.10, it is clear that the atoms remained in the trap for a longer time when the ^{3}He gas is cryopumped to 170 mK as compared to 250 mK data. At 170 mK, the density of ^{3}He is $4 \times 10^{13} \mathrm{cm}^{-3}$ compared to $1 \times 10^{16} \mathrm{cm}^{-3}$ at 250 mK. At this density, the Eu-He mean free path is $\sim$ 3 cm assuming an elastic scattering cross section of 10^{-14} cm^2. In calculating the density, we assumed that the trapped atoms were in thermal equilibrium at 170 mK.

In Figure 6.11, the time profile was fitted using 1-body and 2-body decay separately and also in combination for both 170 mK and 250 mK data. Because the temperature of the cell varies significantly during first 20 s, only the data after the first 20 sec was used in our fit. For the same reason, determination of n_0 during first 20 sec is approximate (within a factor of 1.6). The actual n_0 during the first 20 s would be lower if higher temperature was used for the density calculation .

6.2.4 Trap Loss Mechanisms

Possible 1-body decay mechanisms for the trapped atoms are the loss over the trap edge, Majorana spin-flips, and Eu-He 2-body (or 3-body) processes. For 2-body decay, the possible loss mechanisms are Eu-Eu dipolar relaxation, spin exchange, and Eu-Eu-He 3-body processes.

Decay Rate Calculation

For 1 and 2-body decay, the loss rate can be written as

$$\dot{n} = -\frac{n}{\tau} - Gn^2 \tag{6.15}$$

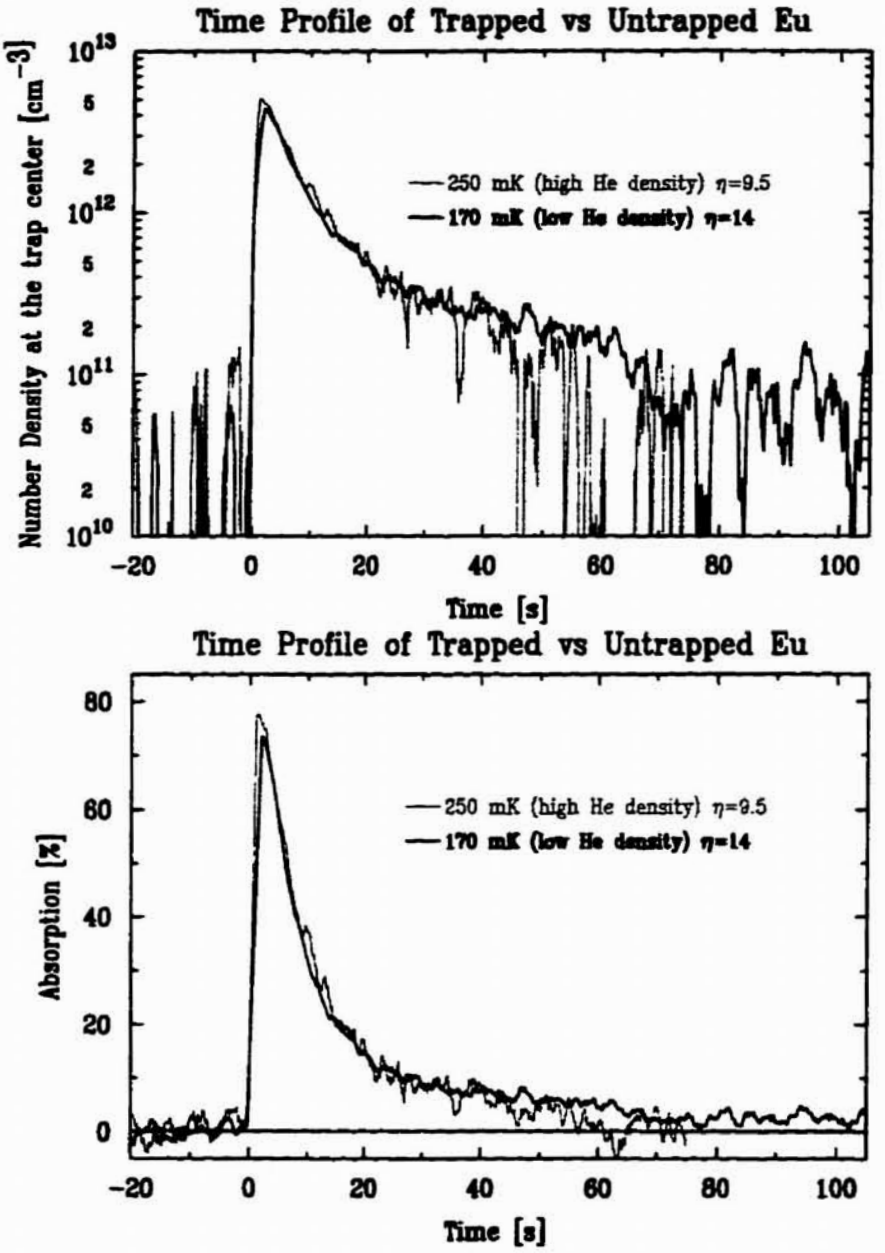

Figure 6.10: Time profile of trapped vs. untrapped Eu. The magnet current was 15 A in both cases. The trapped Eu was created by cryopumping ^{3}He to 170 mK at about 20 s after the ablation pulse.

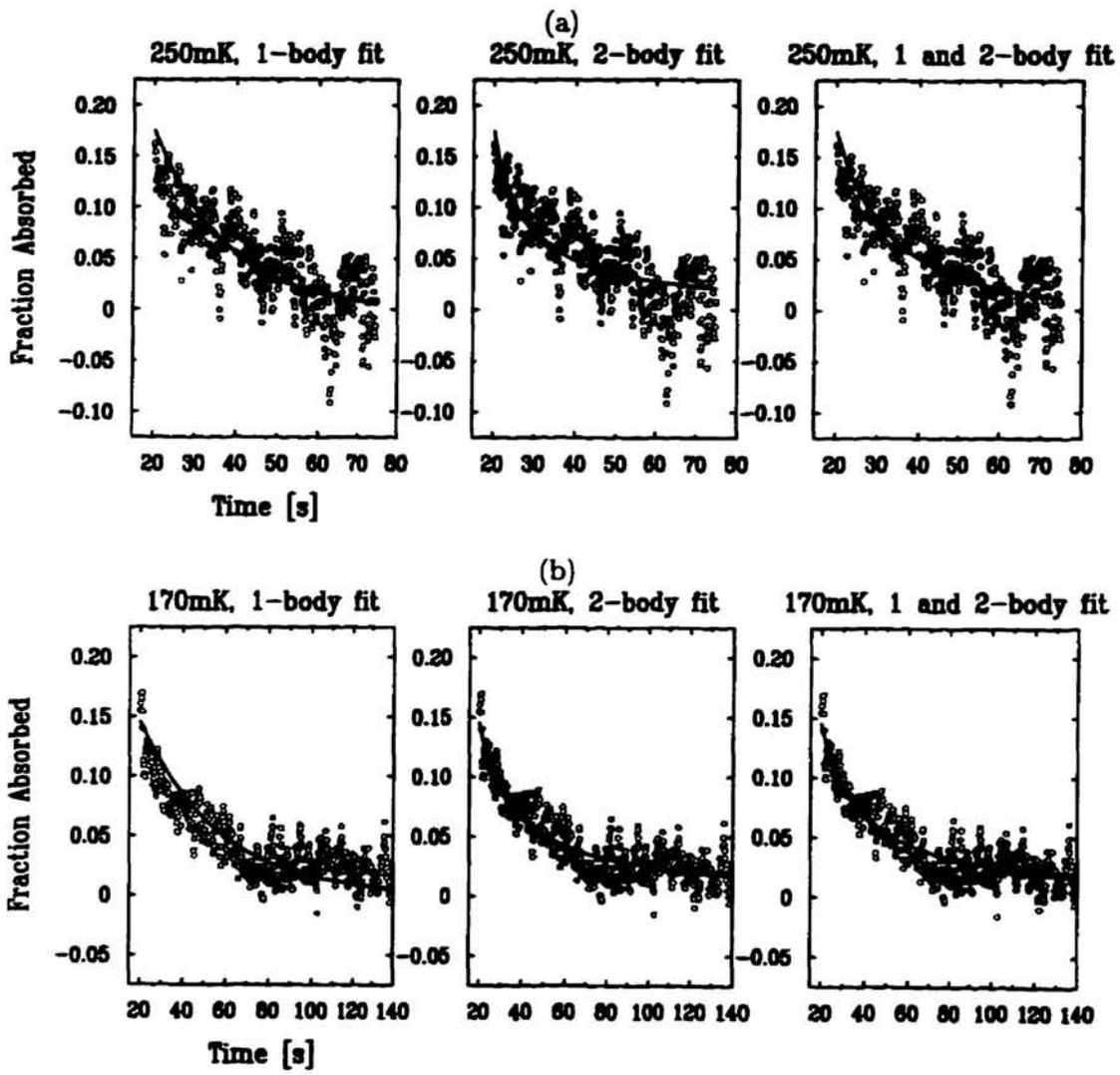

Figure 6.11: Curve fits for absorption time profiles at 170 mK and 250 mK. $a = 0.03\text{s}^{-1}$ and $b = 8 \times 10^{-13}\text{cm}^3\text{s}^{-1}$ for 250 mK data and $a = .001\text{s}^{-1}$ and $b = 3.7 \times 10^{-13}\text{cm}^3\text{s}^{-1}$ for 170 mK data (from 1 & 2-body fit).

Using eqn. 6.9 and integrating over $d^3\vec{r}$, this becomes

$$\begin{aligned}\dot{N} &= -\frac{N}{\tau} - Gn_0^2 \int e^{-\frac{2<\mu>H(\vec{r})}{kT}} d^3\vec{r} \\ &= -\frac{N}{\tau} - Gn_0^2 V_0 (2\eta)^{-3} \\ &= -\frac{N}{\tau} - (\frac{1}{2})^3 G n_0 N \\ \dot{n_0} &= -\frac{n_0}{\tau} - (\frac{1}{2})^3 G n_0^2\end{aligned} \tag{6.16}$$

The general solution to this differential equation is

$$n_0(t) = \frac{1}{(\frac{1}{n_0(0)} + (\frac{1}{2})^3 G\tau) e^{\frac{t}{\tau}} - (\frac{1}{2})^3 G\tau} \tag{6.17}$$

For pure 1-body decay, this becomes $n_0(t) = n_0(0) exp^{-\frac{t}{\tau}}$ For pure 2-body decay, $n_0(t) = ((\frac{1}{2})^{-3} Gt + \frac{1}{n_0(0)})^{-1}$

Loss Over the Trap edge

The loss of atoms over the trap edge is given by the rate at which the atoms in the trap collide with the physical walls in the region where the wall is inside the trap plus the rate at which the atoms escape the trap edge for the rest of region.

If we assume that any atom that strikes the wall or escapes the trap boundary is lost, then the rate is given by

$$\begin{aligned}\dot{N} =& \frac{\int_0^{2\pi} d\phi \int_0^{\pi/2} nAv cos\theta d(cos\theta)}{\int_0^{2\pi} d\phi \int_0^{\pi} d(cos\theta)} \\ =& nvA/4\end{aligned} \tag{6.18}$$

θ and ϕ define the direction of the velocity vector with respect to the normal to the surface. n is the local density on the surface, $n = n_0 e^{\frac{-<\mu>H(\vec{r})}{kT}}$. n_0 is the density at the center of the trap and $<\mu>$ is the magnetic moment of the atom. A is the area of the surface defined by the physical wall and by the trap edge. v is the mean velocity given by $\sqrt{\frac{3kT}{M}}$ (640 cm-s^{-1} at 250 mK for Eu atoms). nA averaged over the surface of our

Current (Amp)	$\eta = \frac{<\mu>H_{max}}{kT}$	A_{eff} (cm^2)
5	3.17	1.9
10	6.34	5.7×10^{-2}
15	9.51	1.9×10^{-3}
20	12.67	6×10^{-5}
25	15.85	2×10^{-6}
30	19.03	7.3×10^{-8}

Table 6.2: A_{eff} computed at various values of η. A_{eff} was integrated over surface area partly defined by the wall and partly by the equipotential surface of the highest magnetic field strength that encloses the center of the trap.

trap edge can be written as $n_0 A_{eff}$ cm^{-1} where $A_{eff} \equiv \int_{Trap\_Surface} e^{\frac{-<\mu>H(\vec{r})}{kT}} d\vec{a}$. For several values of η, A_{eff} has been tabulated in Table 6.2 for our trap geometry. The total number, N, of the trapped atoms is given by eqn. 6.10. The lifetime due to the loss over the trap edge is then

$$\begin{aligned} \tau^{-1} &= \frac{\dot{N}}{N} \\ &= \frac{v A_{eff} \eta^3}{4 V_0} \end{aligned} \tag{6.19}$$

For M_j= 7/2 Eu atoms at 250 mK and 15 A (H_{max} = 0.52 Tesla), τ is 1 s. This is short compared to the observed lifetime of the sample (7 s initially and 25 s or longer 20 s after the ablation pulse). For 170 mK, τ is 200 s.

This is true in the absence of diffusion through the buffer gas. It is unlikely the presence of a buffer gas slows down the loss over the trap edge by very much. In the absence of magnetic field, atoms leave the trap region via diffusion. According to 0 Amp data (See Figure 6.8.), the lifetime is ~1 s. If we take this as our diffusion time constant, it is possible that initially atoms are hot relative to the depth of the trap potential and the loss rate is limited by diffusion time rather than the loss rate over the trap edge (in

absence of other loss mechanisms). When the temperature of the sample comes to an equilibrium (20 s after the ablation pulse), the lifetime will depend on the temperature. If the temperature of the sample is above 250 mK, we expect the lifetime will be limited by the diffusion time (1 s) since diffusion is longer than τ. At 170 mK, τ =200 s. The diffusion time at this temperature (according to a simple scaling law) should be a factor of 16 lower due to the decrease in density of the buffer gas (^{3}He). Therefore, we expect the trap lifetime to be limited by τ (not by the diffusion time).

Majorana Decay

As can be seen from the magnetic field profile of our trap (Figure 5.6, the direction of the field varies with the position in the trap. Atoms moving around inside such a trap will perceive a rotating magnetic field. For a moving atom to follow the changing field direction and keep its orientation with respect to the field, the Larmor frequency, $\frac{<\mu>H}{\hbar}$, has to be larger than the angular frequency of the rotating magnetic field. When this adiabatic condition is violated, it would spin-flip to a high-field-seeking state (This process is called Majorana spin-flip) and be rejected from the trap. In the region of near zero magnetic field, this is the dominant 1-body loss mechanism.

For our trap geometry, the size of this region can be roughly characterized by r^*,

$$r^* = \sqrt{\frac{\pi v \hbar}{<\mu> \frac{dH}{dr}}} \tag{6.20}$$

where v is the velocity of the atom and $< \mu >$ is the magnetic moment. (Here the angular frequency of the rotating field was assumed $\frac{\pi v}{r^*}$.) The averaged value of r^* over the velocity distribution is $r^*_{avg} = \sqrt{\pi v_{mean} \hbar < \mu > \frac{dH}{dr}}$ (this is accurate up to an order of unity constant factor). r^*_{avg} is 1.1 μm for 250 mK and 15 A ($\frac{dH}{dr}$ =0.3 Tesla cm^{-1}). For the rest of the discussion, r^*_{avg} will be denoted by simply r^* The loss rate due to Majorana spin flips can be estimated by considering this region ($r \leq r^*$) as a hole in the trap. The atoms that enter it are ejected from the trap. The rate at which atoms enters this region is given by $\frac{n(r^*)vA}{4}$ (similar to eqn. 6.18). $n(r^*) = n_0 e^{-\frac{<\mu>H(r^*)}{kT}}$ is

$\approx n_0$ for our experimental conditions. A is $\sim 2.6\pi r^{*2}$ accounting for the fact $\frac{dH}{dr}$ is twice as steep along the axial direction of the trap as the radial direction. The lifetime due to Majorana loss is then given by

$$\begin{aligned} \tau_M &= \frac{N}{\dot{N}} \\ &\approx \frac{1.54 V_0 \eta^{-3}}{\pi v r^{*2}} \\ &\propto \frac{T^2}{H_{max}^2} \\ &\propto \eta^{-2} \end{aligned} \tag{6.21}$$

Using typical trapping parameters (250 mK, 15 A), we estimate that Majorana flops limit the trap lifetime to 5 hrs.Including an extra factor of 10 to accommodate for the order-of-magnitude-estimate nature of this calculation, we can set a lower bound for $\tau_{Majorana}$ at $\sim 0.5\ hr$. This is much greater than the lifetime of the trapped ensemble and therefore Majorana losses should not be a dominant loss mechanism.

Dipolar Relaxation and Nuclear Spin Exchange

Dipolar relaxation occurs when a collision induces the spin magnetic moments of two atoms to interact and one of the atoms makes a transition to an anti-trapped high-field seeking state or a marginally trapped ($M_J < 7/2$) state. An alternate view is that an atom in presence of a second atom which is moving toward it with a non-zero spin sees a changing magnetic field created by the magnetic moment of the second atom. This coupling of spin to orbital angular momentum causes the spin to flip to an untrapped state.

Spin exchange is another mechanism by which atoms collide inelastically leaving one of the atoms in untrapped state. Spin exchange is caused by the exchange potential component of the interatomic potential and involves an exchange of angular momentum between the electron spin and the nuclear spin. Spin exchange is forbidden for a doubly spin polarized atoms due to angular momentum conservation.

In evaporative cooling experiments with alkali atoms, dipolar relaxation is the main binary loss mechanism. This is because the spin exchange, with a rate which is generally much higher than the dipolar relaxation rate (1000 times greater in hydrogen[2]), removes from the trap all hyperfine states except for the "pure" ones that are not affected by spin exchange. For atomic hydrogen, only d-state atoms remain in the trap after approximately 1 s. [37] The remaining atoms then leave the trap through dipolar relaxation.

Both dipolar relaxation and spin exchange involve binary collisions, hence the loss rate is proportional to n^2. The rate coefficient G_{dip} for hydrogen atoms was measured to be 1×10^{-15} cm^3s^{-1} (averaged over low field-seekers at low field and low temperature). The measured value agreed rather well with the calculated value[94]. For other alkalis, the measured values of G_{dip} range from 1×10^{-15} cm^3s^{-1} to 3×10^{-14} cm^3s^{-1}[2]. If we assume our measured two-body decay rate of trapped Eu atoms are purely due to dipolar relaxation and fitted data to the appropriate 2-body decay function, $G_{dip} = 3.7 \pm 1.8 \times 10^{-13} cm^3s^{-1}$. *Ab. initio* calculations of dipolar relaxation rate for Eu have not been carried out. (The rate calculation may depends critically on the low energy interatomic potential of Eu molecule.) Hydrogen and alkali atoms that have one electron in the outer shell. Eu, however has a half-filled f-shell. Thus, calculation of these rates (for both dipolar, spin-exchange and elastic collisions) would be quite different. Perhaps this work may motivate a serious attempt at making such calculations. Since the dipolar relaxation rate is due to the μ^2/r^3 term in the interaction Hamiltonian, a simple scaling law would indicate the dipolar relaxation rate of $M_J = 7/2$ of Eu atoms would be $(7^2)^2 = 2401$ times greater than that of hydrogen atoms. (The interaction energy scales as $< \mu >^2$ and the transition rate scales as the square of interaction Hamiltonian matrix element.) This matches quite well with our measured value. However, because the rate may be sensitive to the exact shape of the intermolecular potential at low collision velocities, it is difficult to draw accurate analogies with other systems, such as atomic

hydrogen.

For alkali atoms, spin exchange rate coefficient is generally much greater. For sodium (Na), $G_{ex} = 10^{-11}$ cm^{3}s^{-1}[95]. It is uncertain whether this also holds for Eu atoms. If the spin exchange rate of the trapped $M_J = 7/2$ states of Eu atoms is much greater than the dipolar relaxation rate, we would expect all of the hyperfine states except for $M_J = 7/2, M_I = 5/2$ (which is doubly spin polarized) to depopulate faster leaving only $M_J = 7/2, M_I = 5/2$ states. We see, however, all the hyperfine states are present after 60 sec (Figure 6.2). This implies that the spin exchange rate is comparable or lower than the dipolar rate. At closer inspection, we observed that the relative population of different hyperfine states do change with respect to time; $M_J = 7/2, M_I = 5/2$ states decay at a slower rate than other hyperfine states. However, this could be due to the difference in dipolar relaxation rate among different hyperfine states and therefore it does not provide a solid evidence for spin exchange.

We have not attempted calculation of the spin exchange rate for $M_J = 7/2$ states of Eu atoms nor found the calculation in the literature. The absence of detailed experimental measurements makes it difficult to draw any further conclusion regarding the effects of spin exchange.

3-body Decay Term

It is possible that the decay of the trapped sample includes n^3 term as well as aforementioned n and n^2 terms (i.e. $\dot{n} \propto -Ln^3$ where n is the density of the sample). This can be caused by three-body recombination process involving three Eu atoms.

The three-body recombination rate coefficient, L is not known for Eu atoms. For alkali atoms, L is on the order of 10^{-28} cm^{6}s^{-1} ($L = 2\times10^{-28}$, 2.6×10^{-28}, and 4×10^{-30} for Na, Li, and Rb respectively[93].) If we assume L for Eu to be 100 times bigger than that for sodium atoms, the 2-body decay term would dominate for $n < 10^{13}$ cm^{-3}. Thus we expect the 3-body decay term to be negligible for our trapped sample.

Other Losses

^{3}He has a nuclear magnetic moment which is $\sim$ 1000 times smaller than the magnetic moment for Eu. Hence dipolar relaxation due to Eu-^{3}He collisions should be negligible compared to Eu-Eu collisions (by a factor of 1000^2 if Eu and ^{3}He have the same density). This process becomes significant only when $n_{^3He} > 10^6 n_{Eu}$. Other loss mechanisms include Eu-Eu and Eu-^{3}He dimerizations. In order to form a dimer, a three-body collision is necessary. This requires Eu-^{3}He-^{3}He or Eu-Eu-^{3}He collisions for Eu-^{3}He dimer formation and Eu-Eu-Eu or Eu-Eu-^{3}He collisions for Eu-Eu dimer formation.

Using a simple hard sphere model, τ_1^{-1}, the rate at which type 1 atoms impinges on a composite particle (2+3) (i.e. density of which is the probability per unit volume that particle 2 and 3 are within a spherical volume extended by $r_2 + r_3$) is given by,

$$\tau_1^{-1} = k_1 n_2 n_3 \tag{6.22}$$

where n_2 and $n_3$are density of particle 1 and particle 2 and

$$k_1 = \frac{4\pi}{3}(r_2 + r_3)^3 \pi (r_1 + r_2 + r_3)^2 v_1 \tag{6.23}$$

where r_1, r_2 and r_3 are radius of particle 1, 2 and 3 respectively and v_1 is the velocity of particle 1.

From this formula, it follows

$$\tau_{Eu+Eu+He}^{-1} = k_{Eu+He} n_{Eu} n_{He} \tag{6.24}$$

$$k_{Eu+He} = \frac{4\pi}{3}(r_{Eu} + r_{He})^3 \pi (2r_{Eu} + r_{He})^2 v_{Eu} \tag{6.25}$$

$$\tau_{Eu+Eu+Eu}^{-1} = k_{Eu+Eu} n_{Eu}^2 \tag{6.26}$$

$$k_{Eu+Eu} = \frac{4\pi}{3}(2r_{Eu})^3 \pi (3r_{Eu})^2 v_{Eu} \tag{6.27}$$

$$\tau_{Eu+He+He}^{-1} = k_{He+He} n_{He} n_{He} \tag{6.28}$$

$$k_{He+He} = \frac{4\pi}{3}(2r_{He})^3 \pi (2 * r_H + r_{Eu})^2 v_{Eu} \tag{6.29}$$

The contribution to $\dot{n}_{Eu}$ due to Eu + He and Eu+Eu dimer formations is

$$\dot{n}_{Eu}(\text{dimerformation}) = c_1(k_{Eu+Eu})n_{Eu}^3 + c_2(k_{Eu+He})n_{Eu}^2 n_{He} + c_3(k_{He+He})n_{Eu}n_{He}n_{He} \quad (6.30)$$

where c_1, c_2 and c_3 are dimensionless constants (< 1), which depend on factors such as the interatomic potentials of Eu+Eu and Eu+He, the velocity of v_{Eu} and v_{He}, *etc.*

At T = 250 mK, k's are on the order of $10^{-35} - 10^{-33}$ cm^{6}s-1 (using hard sphere radii of 0.05 nm for He and 0.2 nm for Eu). If we assume the ratio of inelastic scattering to elastic scattering to be 1:10[96], c_1, c_2 and c_3 are ~ 0.1. Since $n_{^3He}(250\ mK) \approx 10^{16}$ cm^{-3} and $n_{Eu_{max}} = 5 \times 10^{12}$ cm^{-3}, the upper limit of $\dot{n}_{Eu}/n_{Eu}$ from three-body processes is $\sim .01$ s^{-1} mainly from inelastic scattering of Eu+He+He. Other three-body rates are smaller since $n_{Eu} < n_{He}$. $\dot{n}_{Eu}/n_{Eu}$ from 2-body decay rate due to Eu-Eu inelastic scattering is $10^{-13}n_{Eu}$ in cgs unit. Therefore, the 2-body decay term dominates for $n_{Eu} > 10^{11}$ cm^{-3}.

At T = 170 mK, $n_{^3He}(170\ mK) \approx 4 \times 10^{14}$ cm^{-3}. Hence, the three-body loss rate according to the above model would be $\sim$ 1000 times smaller. At this temperature, we expect the loss rate due to these three-body inelastic collisions to be negligible.

Chapter 7

Conclusion and Future Research

7.1 Summary

Loading of paramagnetic neutral atoms into a magnetic trap using a cryogenic buffer gas has been described and demonstrated. 10^{12} Eu atoms were loaded into a static anti-Helmholtz trap at 250 mK. A trap lifetime greater 100 s was observed.

In order to further cool the atoms, evaporative cooling is necessary. Unfortunately, our cell and detection method were not designed to accomplish this. Nevertheless, the new precooling and trap loading mechanism described here should greatly expand the number of atoms and molecules that can be trapped.

7.2 Future Improvements

Several improvements can be made to the experiment to better our understanding of the trapped atoms. First we need to image the atom cloud either with a CCD camera or an intensified CCD camera. This will tell the shape and size of the atom cloud as well as the location of the beam with respect to the trapped atoms. This information has to be deduced from the data in our current set-up. Imaging the cloud will provide us the temperature and the momentum distribution of the cloud. For many of the molecules

we are considering for trapping, it is more difficult to find a transition in the visible with high enough oscillator strength for doing absorption spectroscopy. A laser induced fluorescence spectroscopy set up may be necessary for observing the molecules.

In the current set-up, we cannot evaporatively cool atoms due to the eddy current heating in the cell when the magnet is quickly ramped down. Either an rf-knife technique[97] should be employed (this may be technically difficult because we need to sweep ~10 GHz) or the cell should be made out of a composite nonconducting material such as G10[98].

A different trap geometry, for example an Ioffe trap, offers more flexibility in controlling the trap parameters and a bigger trap volume. The trap volume issue may be important if the number of trapped atoms is density limited as in the case of a large dipole-dipole relaxation cross section.

A number of interesting experiments can be carried out with the existing or modified experimental setup. As mentioned above, evaporative cooling can be performed on non-alkali atoms with only minor modifications. This would make it possible to attain BEC in other than alkali species. Molecules have never been trapped. Trapping of molecules is a natural and important extension of this work. There are many paramagnetic molecules with large enough magnetic moments that can be trapped using the current setup. (For example, VO, GdO, EuO and O_2.) Trapping any one of them would likely provide important information on molecular collisions and cluster formation at low temperatures. High resolution spectroscopy of paramagnetic atoms that are suitable for testing fundamental theories could also be easily implemented. The magnetic broadening can be reduced by cooling the atoms further, thereby decreasing the requisite field strength; also, in the case of a very cold ensemble, the trapping field can be switched off altogether. The measurement can be effected while the slow atom cloud is expanding.

Bibliography

[1] A. L. Migdall *et al.*, Phys. Rev. Lett. **54**, 2596 (1985).

[2] W. Ketterle and N. J. Van Druten, Advances in Atomic, Molecular, and Optical Physics. **37**, 181-236 (1996).

[3] M. R. Andrews *et al.*, Science **275** , 5300 (1997).

[4] J. Weiner, J. Opt. Soc. Am. B **6**, 2270 (1989).

[5] D. W. Noid, S. K. Gray, and S. A. Rice, J. Chem. Phys. **84**, 2649 (1986).

[6] S. K. Gray and S. A. Rice, J. Chem. Phys. **83**, 2818 (1985).

[7] D. A. Bell *et al.*, Phys. Rev. B. **34**, 7670 (1986).

[8] C. J. Myatt *et al.*, Phys. Rev. Lett. **78**, 586 (1997).

[9] D. Cho *et al.*, Phys. Rev. Lett. **63**, 2559 (1989).

[10] E. A. Hinds and K. Sangster, AIP Conference Proceedings, Time Reversal, 1991 **270**, 77 (1993).

[11] N. F. Ramsey, in *Molecular Beams* (Oxford University Press, London, 1963).

[12] M. G. Kozlov and V. F. Ezhov, Phys. Rev. A **49**, 4502 (1994).

[13] K. B. Davis *et al.*, Phys. Rev. Lett. **74**, 5202 (1995a).

[14] M. H. Anderson *et al.*, Science **269**, 198 (1995).

[15] H. Hess, Physical Review B **34**, 3476 (1986).

[16] M. -O. Mewes *et al.*, Phys. Rev. Lett. **77**, 416 & 988 (1996).

[17] J. J. Adams *et al.*, Phys. Rev. A. **51**, R22 (1995).

[18] S. Chu *et al.*, Phys. Rev. Lett. **57**, 314 (1986).

[19] J. Miller *et al.*, Phys. Rev. A. **47**, R4567 (1994).

[20] C. S. Adams *et al.*, Phys. Rev. Lett. **74**, 3577 (1995).

[21] W. D. Philips, Proc. Int. Sch. Phys. "Enrico Fermi" **118**, 289 (1992).

[22] J. D. Miller, *et al.*, Phys. Rev. A **47**, R4567 (1993).

[23] F. Shimizu, *et al.*, Jpn. J. Appl. Phys. **31**, L1721 (1992).

[24] C. C. Agosta *et al.*, Phys. Rev. Lett. **62**, 2361 (1989).

[25] R. V. E. Lovelace *et al.*, Nature (London) **318** , 30 (1985).

[26] E. A. Cornell *et al.*, Phys. Rev. Lett. **67**, 2439 (1991).

[27] S. Chu *et al.*, Phys. Rev. Lett. **55**, 48 (1985).

[28] E. L. Raab *et al.*, Phys. Rev. Lett. **59**, 2631 (1987).

[29] C. C. Bradley *et al.*, Phys. Rev. Lett. **75**, 1687 (1995).

[30] P. D. Lett *et al.*, J. Opt. Soc. Am. B **6**, 2084 (1989).

[31] M. A. Kasevich, Bull. Am. Phys. Soc. [2] **40**, 1270 (1995).

[32] J. Lawall *et al.*, Phys. Rev. Lett. **73**, 1915 (1994).

[33] N. R. Newbury *et al.*, Phys. Rev. Lett. **74**, 2196 (1994).

[34] J. M. Doyle, Ph.D. thesis, Massachusetts Institute of Technology, 1991, unpublished.

[35] I. D. Setija *et al.*, Phys. Rev. Lett. **70**, 2257 (1993).

[36] 5H. F. Hess, Bull. Am. Phys. Soc. **30**, 854 (1985).

[37] H. F. Hess *et al.*, Phys. Rev. Lett. **59**, 672 (1987).

[38] N. Masuhara *et al.*, Phys. Rev. Lett. **61**, 935 (1988).

[39] K. B. Davis *et al.*, Int. Conf. At. Phys. 14th, Boulder, CO, 1994, Book Abst., 1-M3 (1994).

[40] W. Ketterle *et al.*, Invited oral presentation at the Annual Meeting of the Optical Society of America, Toronto, Canada, October 3-8.

[41] J. M. Doyle *et al.*, Phys. Rev. Lett. **67**, 603 (1991).

[42] W. Petrich *etal.*, Phys. Rev. Lett. **74**, 3352 (1995).

[43] C. Salomon *et al.*, AIP Conference Proceedings, Atomic Physics, 1990 **233**, 73 (1991).

[44] K. B. Davis *et al.*, Phys. Rev. Lett. **75** , 3969 (1995).

[45] C. C. Bradley *et al.*, Phys. Rev. Lett. **78**, 985 (1997).

[46] J. Kim *et al.*, Phys. Rev. Lett. January, in press. (1997).

[47] J. D. Weinstein *et al.*, Phys. Rev. A., to be submitted. (1997).

[48] S. Lazare *et al.*, Chemtronics **4**, 157 (1989).

[49] R. Srinivasan *et al.*, Appl. Phys. Lett. **41**, 576 (1982).

[50] R. F. Haglund *et al.*, Nucl. Instrum. Methods Phys. Res. B **65**, 206 (1992).

[51] C. Puliafito, ed., Proc. Opthalmic Techol. SPIE (1991) 1423.

[52] M. Karas, *et al.*, Mass Spec. Rev. **10** , 335 (1991).

[53] M. D. Rosen *et al.*, Phys. Rev. Lett. **54**, 106 (1985).

[54] E. T. Arakawa *et al.*, *Lecture Notes in Physics : Laser Ablation* (Sprigner-Verlag, Berlin 1991) Proceedings, Oak Ridge, TN, USA 1991, **389** 82.

[55] H. Wang *et al.*, Appl. Phys. Lett. **59**, 935 (1991).

[56] I. Borthwick *et al.*, *AIP Conference Proceedings : Laser Ablation: Mechanisms and Applications-II* (AIP, New York 1994) Second International Conference, Knoxville, TN, 1993, **288** 414.

[57] C. E. Moore, *Atomic Energy Levels* (U.S. Department of Commerce, National Bureau of Standards, Washington, D. C., 1971), Vol. 1 and 3.

[58] C. E. Moore, *Atomic Energy Levels-The Rare Earth Elements* (U.S. Department of Commerce, National Bureau of Standards, Washington, D. C., 1978).

[59] J. N. Louris *et al.*, Int. J. Mass Spectrom. Ion Processes **88**, 97 (1989), and references contained within.

[60] R. H. Sherman *et al.*, J. Res. Nat. Bureau of Stds. - A. Phys. and Chem. **68A**, 579 (1964).

[61] J. Wilks, in *The Properties of Liquid and Solid Helium* (Clarendon Press, Oxford, 1987). Appendix A.

[62] J. M. Doyle *et al.*, Phys. Rev. A. **52**, R2515 (1995).

[63] G. Z. Zaal *et al.*, Z. Phys **A290**, 339 (1979).

[64] L. D. Landau and E. M. Lifshitz, *Quantum Mechanics* (Pergamon Press, 1977).

[65] A. D. Sappey *et al.*, J. Appl. Phys. **72**, 5095 (1992).

[66] S. Svanberg, in *Atomic and Molecular Spectroscopy, 2nd edition* (Springer-Verlag, Berlin, 1992) p 87.

[67] S. Svanberg, in *Atomic and Molecular Spectroscopy, 2nd edition* (Springer-Verlag, Berlin, 1992) p 162.

[68] Tube Furnace 21100, Thermolyne.

[69] L. S. Nelson and N. A. Kuebler, Spectrochimica Acta. **19** 781 (1963).

[70] Hamamatsu R669, multialkali photomultiplier tube.

[71] T. Kakazawa *et al.*, J. Quant. Spectrosc. Radiat. Transfer **27**, 615 (1982).

[72] Light Metal Platers, Bedford, MA.

[73] HR 760 nm & HT 866 nm, Lightning Optical Corporation.

[74] H. D. Babcock and L. Herzberg, Astrophys. J. **108**, 167 (1948).

[75] By Granville-Philips.

[76] A such device, 1 K cryostat, can be purchased from Infrared Lab.

[77] F. Pobell, *Matter and Methods at Low Temperatures* (Springer-Verlag, Berlin, 1992).

[78] Oxford Instruments.

[79] RV-Elektroniikka Oy Picowatt, VANTAA, Finland.

[80] American Magnetics, Inc. Oak Ridge, TN.

[81] STYCAST 1266 PartA clear epoxy and 1266 PartB

[82] Dupon.

[83] 0.1-0.35 W m^{-1} K^{-1}, from Goodfellow Catalog.

[84] Virgo Optics.

[85] Contiuum model Surelite I-10.

[86] Newport Energy Detector 818J-50B.

[87] Melles Griot, with Coating 275 or Maxbrite Coating.

[88] Jorway model 221

[89] TDS 744A from Tektronics

[90] DS345, Stanford Research Systems.

[91] I. I. Sobel'man, *Excitation of Atoms and Broadening of Spectral Lines* (Springer-Verlag, Berlin, 2nd edition, 1995).

[92] K.B. Blagoev and V.A. Komarovskii, Atomic Data and Nuclear Data Tables **56**, 1-40 (1994).

[93] A. J. Moerdijk *et al.*, Phys. Rev. A. **53**, 916 (1996).

[94] A. Lagendijk, *et al.*, Phys. Rev. B. **33**, 626 (1986).

[95] E. Tiesinga *et al.*, Phys. Rev. A. **43** , 5188 (1991).

[96] D. R. Miller *Atomic and Molecular Beam Methods*, edited by G. Scoles (Oxford University Press, New York, 1988), p. 40.

[97] D. E. Pritchard *et al.*, *Atomic Physics* **11**, 179 (1989).

[98] Goodfellow